Doctoral Thesis in Chemical Engineering

Gas Diffusion Layers for PEM Fuel Cells: Characterization, Modeling and Optimization

MARCUS RINGSTRÖM

KTH ROYAL INSTITUTE OF TECHNOLOGY

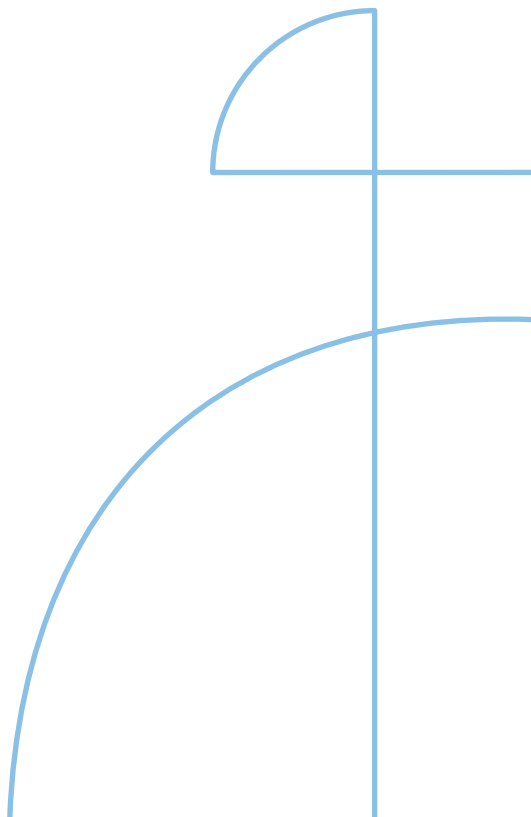

Gas Diffusion Layers for PEM Fuel Cells: Characterization, Modeling and Optimization

MARCUS RINGSTRÖM

Academic Dissertation which, with due permission of the KTH Royal Institute of Technology, is submitted for public defence for the Degree of Doctor of Philosophy on Friday the 13th of November 2026, at 13:30 in F3, Lindstedtvägen 26, Stockholm.

Doctoral Thesis in Chemical Engineering
KTH Royal Institute of Technology
Stockholm, Sweden 2026

AI-Acknowledgment: ChatGPT-5 (OpenAI) was used for minor language editing and to improve the clarity and readability of the thesis. The author has critically reviewed and revised all AI-assisted text and takes full responsibility for the content of the thesis.

© Marcus Ringström
Paper 1: © 2026 The Author(s). CC BY 4.0.
Paper 2: © 2026 The Author(s). CC BY 4.0.
Paper 3: © 2026 The Electrochemical Society.

TRITA-CBH-FOU-2026:52
ISBN: 978-91-8106-763-7

Printed by: Universitetsservice US-AB, Sweden 2026

Abstract

Proton exchange membrane fuel cells (PEMFCs) are electrochemical energy conversion systems that convert the chemical energy of hydrogen directly into electrical energy. Gas diffusion layers (GDLs) facilitate reactant transport, water management, and electrical and thermal conduction. Their effective properties depend on material architecture and compression, while their influence on cell performance depends on flow-field geometry and operating conditions. This thesis investigates these relationships through experimental characterization, X-ray computed tomography, continuum modelling, and surrogate-assisted multi-objective optimization.

The thesis provides new insights into how substrate architecture, mechanical properties, and water invasion influence GDL function. The native fiber-binder architecture affected the distribution of subsequently applied polytetrafluoroethylene (PTFE), demonstrating that nominal loading alone is insufficient to describe its distribution within the material. GDL material recovered after approximately 20,000 h of stack operation exhibited differences in pore structure, external wettability, and capillary water invasion relative to the pristine material. Water saturation was higher in the aged material at low capillary pressures, whereas the opposite occurred at higher pressures. Nevertheless, the relative diffusivity–saturation relationships remained broadly similar. These findings distinguish differences in water uptake at a given capillary pressure from differences in the fractional reduction in gas diffusivity at a given saturation.

Material characterization revealed a strong dependence on compression. The measurements informed constitutive relations used in a physics-based continuum model to describe local compression-dependent properties. Through-plane elastic stiffness had the largest mechanical influence on predicted performance within the investigated parameter range, while shear stiffness became more influential with increasing channel width. The effect of stiffness on current uniformity depended on flow-field geometry, supporting the selection of mechanical properties according to rib–channel dimensions. Mean current density was primarily associated with through-plane oxygen transport, whereas current non-uniformity was more strongly associated with lateral transport beneath the ribs.

Joint optimization of GDL properties and flow-field geometry quantified the trade-offs between mean current density, current uniformity, and electrical contact resistance. The analysis showed how under-rib oxygen transport and electrical contact resistance jointly influence the current distribution and constrain design selection. Across changes in operating conditions, design rankings remained comparatively stable despite reduced accuracy in absolute performance predictions. For most investigated conditions, limited additional simulations supported continued use of previously identified designs, reducing the need to repeat the complete optimization.

Together, these findings provide a physical basis for screening candidate GDLs and prioritizing material properties according to assembly compression, flow-field geometry, and performance requirements within the investigated conditions.

Keywords: Proton exchange membrane fuel cells, gas diffusion layers, material characterization, compression, wettability, ageing, multiphysics modelling, multi-objective optimization.

Sammanfattning

Protonutbytesmembranbränsleceller (PEMFC) är elektrokemiska energiomvandlare som omvandlar kemisk energi till elektrisk energi. Gasdiffusionsskiktet (GDL) bidrar till reaktanttransport, vattenhantering samt elektrisk och termisk ledning. Materialegenskaperna beror på struktur och kompression, medan deras inverkan på cellprestandan påverkas av flödesfältets geometri och driftförhållandena. Syftet med avhandlingen är att undersöka dessa samband genom experimentell materialkaraktärisering, röntgentomografi, fysikbaserad kontinuummodellering och surrogatbaserad flerobjektivsoptimering.

Avhandlingen bidrar till nykunskap om hur materialets struktur påverkar fördelningen av impregnerad polytetrafluoreten (PTFE). I substratet utan bindemedel återfanns PTFE främst vid fiberkontakter och längs angränsande fiberytor, medan PTFE i substratet med bindemedel huvudsakligen var lokaliserat till det kolbaserade bindemedlet. Den nominella PTFE-halten är därför inte tillräcklig för att beskriva fördelningen i materialet.

Material som undersökts efter cirka 20 000 timmars stackdrift uppvisade skillnader i porstruktur och yttre vätbarhet jämfört med referensmaterialet. Vattenmättnaden var högre i det åldrade materialet vid låga kapillärtryck, medan referensmaterialet uppvisade högre vattenmättnad vid högre tryck. Trots skillnaderna i vattenupptagning observerades inga systematiska skillnader i sambandet mellan relativ gasdiffusivitet och vattenmättnad. Vid samma vattenmättnad var den relativa minskningen av gasdiffusiviteten jämförbar i det åldrade materialet och referensmaterialet. Resultaten visar att gastransporten efter långvarig drift behöver analyseras med hänsyn till både materialets transportegenskaper och sambandet mellan kapillärtryck och vattenmättnad.

Materialkaraktäriseringen visade hur kompressionen påverkade mekaniska egenskaper, elektrisk och termisk ledning samt gastransport. Mätningarna låg till grund för konstitutiva materialsamband som användes i en fysikbaserad kontinuummodell. Kompressionsstyvheten hade störst inverkan på cellprestanda inom det undersökta parameterområdet, medan skjuvstyvhetens betydelse ökade med kanalbredden. De mekaniska egenskapernas inverkan på strömtäthetsfördelningen berodde på flödesfältets geometri. Medelströmtätheten var främst kopplad till syretransporten genom materialets tjocklek, medan transporten under ribborna hade större betydelse för strömtäthetsfördelningens homogenitet.

Optimering av GDL-egenskaper och flödesfältsgeometri kvantifierade avvägningarna mellan hög medelströmtäthet, uniform strömtäthetsfördelning och elektrisk kontaktresistans. Vid ändrade driftförhållanden var den inbördes rangordningen mellan olika kombinationer av materialegenskaper och geometri mer tillförlitlig än prediktionerna av absolut prestanda. För sex av sju undersökta förändringar i driftförhållanden kunde tidigare optimeringsresultat användas efter ett begränsat antal kompletterande simuleringar. Detta bidrog till att minska det totala antalet simuleringar jämfört med fullständiga simuleringskampanjer vid nya driftförhållanden.

Avhandlingen ger en fysikalisk grund för urval av GDL-material och identifierar vilka materialegenskaper som bör prioriteras för en given flödesfältsgeometri. Resultaten tydliggör vilka avvägningar mellan cellprestanda, strömtäthetsfördelning och elektrisk kontaktresistans som behöver beaktas vid val av GDL-material och flödesfältsgeometri.

Nyckelord: Protonutbytesmembranbränsleceller, gasdiffusionsskikt,materialkaraktärisering, kompression; transportegenskaper, vätbarhet, åldring; multifysikmodellering, flerobjektivsoptimering

Acknowledgement

This thesis would not have been possible without the support, knowledge, and encouragement of the people who have accompanied me throughout this journey.

I would like to express my sincere gratitude to my main supervisor, Rakel Wreland Lindström, and my co-supervisors, Göran Lindbergh, Henrik Ekström, and Lisa Kylhammar, for their guidance and support throughout my doctoral studies. Their expertise and perspectives have been invaluable to this work and to my development as a researcher.

I gratefully acknowledge PowerCell Sweden AB, StandUp for Energy, and the Swedish Electromobility Centre for their financial support, which made this research possible.

My sincere thanks go to Gabor Toth for generously sharing his deep knowledge of fuel cells. I am also grateful to Jens Eller for the research collaboration at the Paul Scherrer Institute (PSI) and for sharing his expertise in X-ray imaging of water distribution in gas diffusion layers.

I would like to thank my colleagues at PowerCell and the Div. Applied Electrochemistry for their curiosity, knowledge, and stimulating discussions. Special thanks go to Björn Eriksson, whose expertise and engagement I have greatly appreciated, and to Raimund von der Emden for the many interesting conversations about life and everything beyond research.

Finally, I dedicate this thesis to my partner, Mikaela. Thank you for your love, patience, and unwavering support throughout this journey. You have stood by me through its challenges and shared in its joys. Without you, this thesis would not have been possible.

List of Publications

Paper I. Ringström, M., Ekström, H., Kylhammar, L., Lindbergh, G., and Wreland Lindström, R. (2026). *Comprehensive ex-situ characterization of the compression-dependent properties of gas diffusion layers in PEM fuel cells.* Energy Conversion and Management, 356, 121319. https://doi.org/10.1016/j.enconman.2026.121319

Paper II. Schulz, D., Ringström, M[1]., Sankar, S. R., and Martinelli, A. (2026). *The role of native binder in controlling the polytetrafluoroethylene distribution in gas diffusion layers for proton exchange membrane fuel cells.* Fuel Cells, 26(4), e70139. https://doi.org/10.1002/fuce.70139

[1]I and Schulz contributed equally to this work and agreed to share first authorship. This designation is not indicated in the published article.

Paper III. Ringström, M., Ekström, H., Lindbergh, G., and Wreland Lindström, R. (2026). *Interplay between the GDL mechanical properties and the flow field structure in PEMFCs.* Journal of The Electrochemical Society. https://doi.org/10.1149/1945-7111/aeb076

Paper IV. Ringström, M., Ekström, H., Kylhammar, L., Lindbergh, G., and Wreland Lindström, R. *Certified transfer of multi-objective Bayesian optimization across PEM fuel cell operating conditions.* Manuscript to be submitted to Energy and AI.

Paper V. Thiele, B = Ringström, M., Galante, B., Garcia Padilla, A., Herranz, J., Schmidt, T. J., Eller, J., Ekström, H., Boden, A., Lindbergh, G., and Wreland Lindström, R. *Image-based characterization of aged gas diffusion layers for PEM fuel cells.* Manuscript in preparation.

Publication Not Included in This Thesis

Butori, M., Petrovick, J., Eriksson, B., Liljenberg, M., Ringström, M., Jannasch, P., Svens, P., Lagergren, C., Lindbergh, G., and Wreland Lindström, R. (2026). *Intermediate temperature proton exchange membrane fuel cells: A systematic review of recently electrochemically evaluated materials.* Applied Energy, 410, 127499. https://doi.org/10.1016/j.apenergy.2026.127499

Author Contributions

Paper I. I developed the methodology, performed the experiments and data analysis, and wrote the manuscript.

Paper II. I contributed to the conceptualization of the study, analyzed the limiting-current density data, and contributed to writing and revising the manuscript.

Paper III. I conceptualized the study, implemented the numerical model, performed the data analysis, and wrote the manuscript.

Paper IV. I conceptualized the study, implemented the numerical model and computational framework, developed the code, performed the data analysis, and wrote the manuscript.

Paper V. Barbara Thiele performed the dry and wet image preprocessing and segmentation and the external contact-angle measurements. I performed the quantitative XCT post-processing, including the formal analysis and computed the transport properties. Barbara Thiele and I jointly wrote the manuscript.

Declaration of generative AI use

Generative AI (ChatGPT-5, OpenAI) was used to assist with language editing. The author critically reviewed and revised all AI-assisted content and takes full responsibility for the thesis.

Nomenclature

Symbol	Unit	Definition
A		Fitting constants, pre-factor
B		Model constant
a	–	Anode
a	–	Log-response transfer offset and slope
b	–	Log-response transfer offset and slope
b	Pa	Klinkenberg slip coefficient
c	–	Cathode
c	$\mathrm{mol\ m^{-3}}$	Concentration
CL	–	Catalyst layer
CV	–	Coefficient of variation
D	$\mathrm{m^2 s^{-1}}$	Diffusivity
DNS	–	Direct numerical simulation
det	–	Determinant
E	Pa	Young's modulus
E	V	cell potential
EDX	–	energy-dispersive X-ray spectroscopy
F	Pa	Applied force
$\mathbf{F}$	–	Deformation gradient
FFP	–	Flow-field plate
g	mm	Shear span
GDL	–	Gas diffusion layer
I	A	Current
ICR	$\mathrm{m\Omega cm^2}$	Interfacial contact resistance
j	$\mathrm{A\ cm^{-2}}$	Current density
$\mathbf{J}$	$\mathrm{mol\ cm^{-2} s^{-1}}$	Diffusive flux vector
k	–	Relative permeability
$\boldsymbol{K}$	$\mathrm{m^2}$	Intrinsic permeability tensor
L	m	Path length
MD	–	Machine direction
MIP	–	Mercury intrusion porosimetry
MPL	–	Microporous layer
N	–	Number
$\mathbf{N}$	$\mathrm{mol\ cm^{-2} s^{-1}}$	Molar flux vector
p	Pa	Pressure
P	$\mathrm{W\ cm^{-2}}$	Power density
PEM	–	Proton exchange membrane
PEMFC	–	Proton exchange membrane fuel cell
PTFE	–	Polytetrafluorethylene
ref	–	Reference

r	–	Throat
$\mathbf{r}$	m	Distance vector
R	$\mathrm{m\Omega cm^2}, \mathrm{s\ m^{-1}}$	Resistance
R^2		Coefficient of determination
REV	–	Representative elementary volume
RH	–	Relative humidity
S	–	Liquid water saturation
SEM	–	Scanning electron microscopy
t	m	Thickness
T	K	Temperature
TP	–	Through-plane
$\boldsymbol{u}$	$\mathrm{m\ s^{-1}}$	Superficial fluid velocity vector
U	V	Voltage
UI	–	Uniformity index
V	$\mathrm{m^3}$	Volume
W	mm	Width
x	–	Molar fraction
x	–	In-plane coordinate
XCT	–	X-ray computer tomography
y	–	Through-plane coordinate
$\mathbf{x}, \mathbf{z}, \mathbf{y}$	–	Design, surrogate-input and response vectors
Y	–	Mass fraction

Greek

α	–	Phase
γ	–	Shear angle
ρ	$\mathrm{kg\ m^3}$	Mass density
ϕ	–	Porosity/volume fraction
Δ	–	Difference
∂	–	Partial derivative
∇	–	Nabla operator $\left(\frac{\partial}{\partial x}, \frac{\partial}{\partial y}, \frac{\partial}{\partial z}\right)$
η	V	Overpotential
ε	–	Strain
κ	$\mathrm{W\ m^{-1}\ K^{-1}}$	Thermal conductivtiy
σ	$\mathrm{S\ m^{-1}}, \mathrm{N\ m^{-2}}$	Electrical conductivity, mechanical stress
ξ	$\mathrm{N\ m^{-1}}$	Surface tension
θ	°, –	Contact angle, hyperparameter
τ	–	Tortuosity
δ	–	Log-response transfer discrepancy
μ	Pa s, –	Dynamic viscosity, covariance function

φ	V	Potential
Latin		
$\mathcal{J}$	$-$	Local volume ratio
$\mathcal{R}$	$\mathrm{J\,mol^{-1}K^{-1}}$	Gas constant
$\mathcal{F}$	$\mathrm{As\,mol^{-1}}$	Faraday's constant
$\mathcal{E}$	$-$	Agglomerate volume fraction
Subscript		
0		Initial value
lim		Limiting
ch, rib		Channel, rib
act, Ω, conc		Activation, ohmic, concentration
abs, cont		Absolute, contact
Bulk, rel		Bulk, relative
g, l, s		Gas, liquid, water, solid
i, q, α		Species; spatial direction; phase
ip, tp		In-plane; through-plane
crit, tot, sub		Critical threshold, total, substrate
ref,tar		Reference, target
m		Response
M, K, B		Molecular, Knudsen, Bosanquet
$e^-, \mathrm{H^+}$		Electronic, protonic
$\mathrm{O_2}$		Oxygen
$\mathrm{H_2O}$		water
rev		Reversible
tot		total
agg		Agglomerate
w		wetting
nw		Non-wetting
Superscript		**Definition**
eff		Effective property
dry		Dry state
$\mathrm{O_2}$		Oxygen transport
0		Standard electrode potential

ABSTRACT 1

SAMMANFATTNING 2

1. INTRODUCTION 11

1.1 MOTIVATION 11
1.2 RESEARCH QUESTIONS 13

1.3 PEMFC FUNDAMENTALS 14

1.3.1 Operation principles 14
1.3.2 Cell Performance and Voltage Losses 15
1.3.3 Flow-Field Plate and Rib-Channel Geometry 16
1.3.4 Gas Diffusion Layer 17
1.3.5 GDL Manufacturing and Directionality 18
1.3.6 GDL compression 19
1.4 GDL STRUCTURE 20
1.4.1 Porosity and Pore-Size Distribution 21
1.4.2 Tortuosity, Connectivity, and Percolation 21
1.4.4 Wettability and Capillary Pressure 23
1.5 AGEING OF GAS DIFFUSION LAYERS 24
1.6 IMAGING OF WATER IN PEMFCS 24
1.7 MODELLING STRATEGIES 25
1.7.1 Continuum models 25
1.7.2 Pore-scale modeling and upscaling 25
1.8 SURROGATE MODELING AND MULTI-OBJECTIVE OPTIMIZATION 26
1.9 KNOWLEDGE GAPS AND THESIS SCOPE 27

2.1 MATERIALS AND EXPERIMENTAL METHODS 29

2.2 INVESTIGATED GDL MATERIALS 29
2.3.1 Mechanical properties 30
2.3.2 Electrical and thermal properties 30
2.2.3 In-plane gas permeability 31
2.2.4 Characterization of the GDL pore structure 32
2.3 PTFE DISTRIBUTION AND OXYGEN TRANSPORT RESISTANCE 32
2.3.1 PTFE treatment and microstructural characterization 32
2.3.3 Wettability and oxygen transport resistance 33
2.4 IMAGE-BASED CHARACTERIZATION 34
2.4.1 Materials and sample selection 34
2.4.2 Water injection measurements 34
2.4.3 Image reconstruction and phase segmentation 35
2.5 Image-based quantification of pore structure and gas transport 36
2.5.1 Representative Elementary Volume (REV) 37

3 EXPERIMENTAL RESULTS 38

3.1 GDL PORE STRUCTURE 38
3.2 MECHANICAL PROPERTIES 39
3.3 THERMAL AND ELECTRICAL PROPERTIES 40
3.4 IN-PLANE GAS PERMEABILITY 42
3.5 GDL MICROSTRUCTURE, PTFE DISTRIBUTION, AND OXYGEN TRANSPORT 43
3.6 AGEING-INDUCED CHANGES IN GDL STRUCTURE AND WATER TRANSPORT 44
3.6.1 Wettability and Pore Structure 44
3.6.2 Capillary pressure and water distribution 46

3.6.3 Diffusivity ... *48*

4. MODEL DEVELOPMENT ... **50**

4.1 CONTINUUM PEMFC MODEL ... 50

4.1.1 Model assumptions ... *51*

4.2 Constitutive models ... *53*

4.2.1 Mechanical Constitutive Law ... *53*

4.2.2 Compression-dependent transport properties ... *53*

4.2.3 Electrical contact resistance ... *54*

4.2.4 MIP-informed constitutive models ... *55*

4.3 GDL Flow-field Interaction ... *57*

4.3.1 Flow-field configurations and parametric study ... *57*

4.4 SURROGATE-ASSISTED OPTIMIZATION FRAMEWORK ... 59

4.4.1 Design space, objectives, and simulation database ... *59*

4.4.3 Transfer between operating conditions ... *60*

5. MODEL RESULTS ... **62**

5.1 Coupled influence of GDL mechanics and flow-field geometry on cell performance ... *62*

5.2 Current-density uniformity and co-design ... *63*

5.3 SURROGATE-ASSISTED GDL DESIGN AND OPERATING-CONDITION TRANSFER ... 65

5.3.1 Design sensitivity and Transport descriptors ... *65*

5.3.2 Stability of design relationships across operating conditions ... *66*

5.3.3 Reuse of optimization results across operating conditions ... *67*

6. CONCLUSIONS AND FUTURE WORK ... **69**

6.1 CONCLUSIONS ... 69

6.2 FUTURE WORK ... 70

REFERENCES ... **71**

1. Introduction

1.1 Motivation

Reducing dependence on fossil fuels requires energy-conversion technologies capable of meeting the demands of transport and other energy-intensive sectors while limiting greenhouse-gas emissions [1,2]. Hydrogen fuelled proton exchange membrane fuel cells (PEMFCs) are of particular interest for applications where requirements on range, refuelling time, system mass, and power density can make direct battery electrification challenging. PEMFCs operate at relatively low temperatures and convert hydrogen electrochemically without direct carbon dioxide emissions at the point of use, although their overall climate impact depends on how the hydrogen is produced and supplied.

Further development of PEMFCs requires improvements in efficiency, power density, durability, and cost. These requirements depend partly on the coupled transport processes within the membrane-electrode assembly (MEA), where reactant gases must reach the catalyst layers, product water must be removed while adequate membrane hydration is maintained, and heat and electrical current must be conducted efficiently [3] At high current densities, limitations in oxygen transport and liquid-water accumulation can increase mass-transport losses, promote non-uniform current distributions, and reduce cell efficiency [4].

The gas diffusion layer (GDL), positioned between the catalyst layer and the flow-field plate, contributes to each of these processes. It provides pathways for gases, liquid water, electrons, and heat while mechanically supporting the MEA. The effective behaviour of the GDL is determined by the fiber architecture, binder and hydrophobic treatment, the presence of a microporous layer (MPL), and the local states of compression and water saturation [5–9]. Understanding GDL behaviour therefore requires quantitative relationships between material composition, structure, deformation and transport.

A central challenge is the influence of assembly compression. Compression changes the GDL thickness, pore structure, fiber contacts, and interfacial contact conditions. Mechanical compression can therefore improve electrical and thermal conduction while simultaneously impede gas and liquid-water transport. Because the rib-channel geometry produces spatially non-uniform compression, the resulting material properties also depend on the local compression state of the GDL and the interaction with the flow-field geometry. Material characterization must therefore be coupled with constitutive modelling to determine how the transport and mechanical properties translate into cell-scale behaviour.

Material composition and wettability introduce further complexity. Hydrophobic treatment is commonly described through PTFE loading, yet the resulting material behaviour also depends on how PTFE is distributed within the porous structure and how that distribution is influenced by the carbonaceous binder. Nominal PTFE content alone may therefore be insufficient to describe the resulting wettability and transport characteristics [10–12] . Prolonged operation may additionally modify both pore structure and surface properties, with consequences for capillary water transport and gas diffusion. Characterization of GDLs recovered after extended stack operation is therefore needed to determine how these changes alter the wettability under service conditions.

This thesis addresses these coupled effects through experimental characterization, pore-scale imaging, continuum modelling, and surrogate-assisted optimization. Mechanical and compression-dependent transport properties are quantified and incorporated into constitutive descriptions for PEMFC modelling, enabling the interaction between GDL mechanics and flow-field geometry to be examined at the rib-channel scale. Complementary studies investigate how native binder affects PTFE

distribution and how prolonged stack operation modifies pore structure, wettability, local water distribution, and effective diffusivity. The resulting modelling framework is subsequently combined with surrogate modelling and multi-objective optimization to investigate trade-offs between GDL properties, flow-field geometry, and operating conditions.

The overall objective is to establish quantitative links between GDL composition, structure, mechanical behaviour, and transport, and to use these relationships to strengthen the physical basis for PEMFC modelling and GDL–flow-field design.

The research also relates to the United Nations Sustainable Development Goals, particularly Goal 7, Affordable and Clean Energy; Goal 9, Industry, Innovation and Infrastructure; and Goal 12, Responsible Consumption and Production. Its relevance to Goal 7 lies in addressing transport and electrical losses that limit fuel-cell performance. A better understanding of these losses can support the development of more efficient energy-conversion technologies, although the benefits at system level depend on operating strategy and auxiliary energy requirements. In relation to Goal 9, the thesis provides experimental data and modelling methods that support the development of fuel-cell components.

The ability to compare GDL materials in conjunction with flow-field geometry provides a basis for material selection and targeted experimental evaluation. Furthermore, using existing optimization results to inform design selection at changed operating conditions can reduce the number of additional simulations required during component development. The connection to Goal 12 concerns material use and durability. Understanding how prolonged operation affects water uptake and gas transport can inform future efforts to improve component lifetime, while the investigation of PTFE distribution supports a more detailed assessment of hydrophobic treatment. These contributions do not, however, establish longer service life or lower material consumption. The broader environmental benefits also depend on hydrogen production and supply, component manufacturing, and end-of-life treatment. Consequently, the thesis contributes knowledge relevant to sustainable fuel-cell development, while quantification of the resulting environmental benefits requires further experimental validation and life-cycle assessment.

1.2 Research questions

The thesis is guided by the following research questions:

RQ1. How do GDL structure and compression influence mechanical behaviour, gas permeability, thermal conductivity and electrical conductivity, and how can these relationships be represented by constitutive models?

RQ2. How do native binder and hydrophobic treatment influence PTFE distribution, wettability and oxygen transport in GDLs?

RQ3. How do the orthotropic mechanical properties of the GDL interact with assembly compression and flow-field geometry to determine local transport, current distribution and cell performance?

RQ4. What differences in pore structure and wettability are observed between pristine and aged GDLs, and how are these differences associated with water invasion, liquid-water distribution and structural changes?

RQ5. What trade-offs between mean current density, current density uniformity and interfacial contact resistance arise when GDL properties and rib geometry are varied, and how accurately can surrogate models predict these responses and adapt to other operating conditions using limited additional simulations?

1.3 PEMFC fundamentals

1.3.1 Operation principles

A proton exchange membrane fuel cell (PEMFC) consists of a membrane electrode assembly (MEA) positioned between two flow-field plates that contain the reactant channels, as illustrated in Fig. 1.1. The MEA comprises a proton-conducting membrane (PEM), catalyst layers (CLs), and gas diffusion layers (GDLs), commonly incorporating microporous layers (MPLs) between the fibrous substrates and catalyst layers. The membrane separates the anode and cathode gas compartments while conducting protons, restricting reactant crossover, and providing electronic insulation. The catalyst layers contain the active sites for the electrochemical reactions [13] .

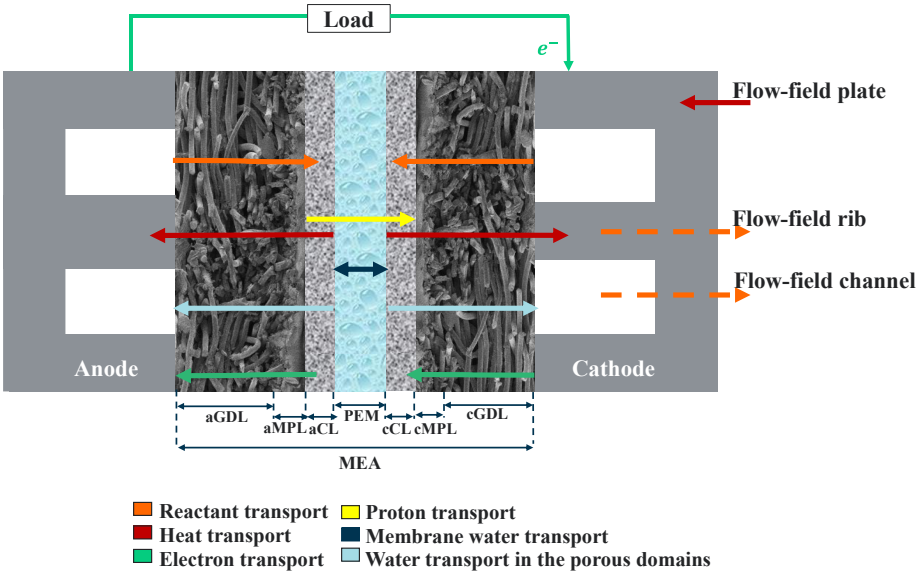

Figure 1.1. Schematic representation of a polymer exchange membrane fuel cell (PEMFC) and the associated transport processes. (a) Fuel cell unit illustrating electron, reactant, product water, proton, and thermal transport across the membrane electrode assembly and gas diffusion layers. (b) Cross-sectional image showing the layered architecture of the cell, including the flow-field plates (FFPs), gas diffusion layers (GDLs), and membrane electrode assembly (PEM+CLs).

Hydrogen supplied through the anode flow-field channels is transported through the porous GDL and MPL to the anode catalyst layer. At the catalyst layer, hydrogen is oxidized [14] :

$$H_2 \rightarrow 2H^+ + 2e^- \tag{1.1}$$

The corresponding standard equilibrium potential is $E_a^0 = 0$ V versus the standard hydrogen electrode (SHE). The generated protons and electrons are subsequently transported through separate pathways. Protons are conducted through the PEM from the anode to the cathode, whereas electrons are transported through the electronically conducting porous electrode and flow-field plate into the external circuit and subsequently to the cathode through the corresponding conducting components.

At the cathode, oxygen supplied through the flow-field channels passes through the GDL and MPL to the CL, where it reacts with protons and electrons to form water:

$$\frac{1}{2}O_2 + 2H^+ + 2e^- \rightarrow H_2O \tag{1.2}$$

For liquid water at 25℃, the standard cathode equilibrium potential is $E_c^0 = 1.229$ V vs SHE. Combining Eqs.(1.1) and (1.2) gives the overall cell reaction:

$$H_2 + \frac{1}{2}O_2 \rightarrow H_2O \tag{1.3}$$

The corresponding standard reversible cell voltage is:

$$E_{\text{cell}}^0 = E_c^0 - E_a^0 = 1.229\ \text{V} \tag{1.4}$$

The electrochemical reactions are coupled to water and heat transport throughout the cell. Water transport governs membrane hydration and liquid-water accumulation in the porous layers, thereby affecting proton conduction and reactant access to the catalyst layers. Heat generated during operation is conducted through the cell components towards the flow-field plates. The interaction between these processes determines the local temperature, water distribution, and reactant concentrations, which in turn influence the reaction rates and spatial distribution of current density.

1.3.2 Cell performance and voltage losses

PEMFC performance is commonly represented by the polarization curve, which relates the cell voltage, V_{cell}, to the cell current density, j_{cell}. The corresponding power density is given by:

$$P = V_{\text{cell}} \times j_{\text{cell}} \tag{1.5}$$

For an ideal thermodynamics cell, the operating voltage would equal the reversible thermodynamic voltage, E_{rev} under standard conditions. In practice, the measured open-circuit voltage (OCV) is lower than E_{rev} due to processes such as reactant crossover, internal currents, and parasitic reactions. Under load, additional irreversible losses further reduce the cell voltage, which is usually expressed as:

$$V_{\text{cell}} = E_{\text{rev}} - \eta^{\text{act}} - \eta^{\Omega} - \eta^{\text{conc}} \tag{1.6}$$

Where η^{act}, η^{Ω}, and η^{conc} denote the activation, ohmic, and concentration overpotentials, respectively. Their relative contributions vary with j_{cell} producing to the characteristic shape of the polarization curve shown in Fig. 1.6.

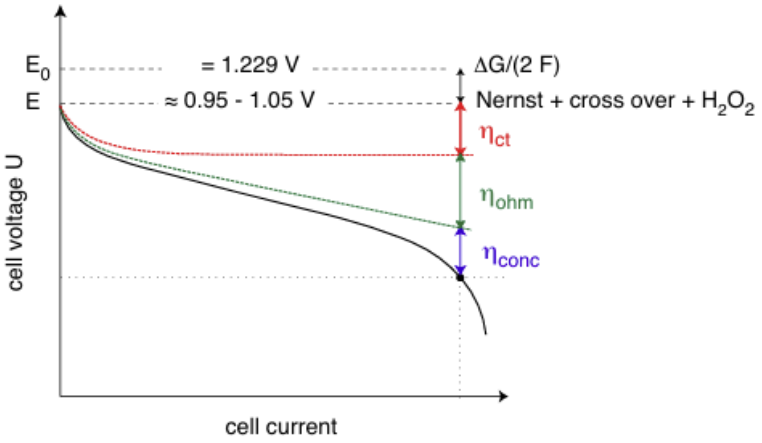

Figure 1.2. Schematic polarization curve of a PEM fuel cell illustrating the reduction in cell voltage from the thermodynamic reversible potential, E^0, to the operating voltage. The principal contributions to the voltage loss are the activation overpotential, η^{act}, ohmic overpotential, η^{Ω}, and concentration overpotential, η^{conc}. The difference between the reversible potential and the practical open-circuit voltage additionally reflects effects such as reactant crossover and parasitic reactions. Adapted from [15].

Activation losses arise from the finite kinetics of the electrode reactions and are the dominant loss mechanism in conventional PEMFCs by the comparatively slow oxygen reduction reaction (ORR) at the cathode. Ohmic losses originate from protonic and electronic resistance within the ionomer and porous domains, and their interfaces, and increase approximately proportionally with current density. Concentration losses result from reactant depletion at the electrochemically active sites and become more pronounced at high current densities, as increased reactant consumption leads to larger concentration gradients.

1.3.3 Flow-field plate and rib-channel geometry

Flow-field plates provide electrical and thermal conduction, mechanical support, and distribution of the reactant gases across the active area of the cell. Flow channels formed in the plates distribute hydrogen and oxygen over the respective electrodes and facilitate removal of product water, while the ribs provide mechanical, electrical, and thermal contact with the GDL [16,17]. Common flow-field configurations include serpentine, parallel, and interdigitated designs, which provide different compromises between reactant distribution, pressure drop, and water removal [18].

In addition to the overall flow-field topology, the local rib-channel geometry influences transport and mechanical conditions within the porous electrode. The rib and channel widths determine both the distance over which reactants must be transported laterally beneath the ribs and the fraction of the GDL that is directly supported by the flow-field plate. Geometrical parameters such as the channel-to-rib ratio therefore affect reactant transport, local contact conditions, and cell performance [19–21].

The choice of flow-field plate material is governed by competing requirements related to electrical and thermal conductivity, corrosion resistance, mechanical strength, manufacturability, and cost [22–27]. Metallic plates offer advantages in compactness and mechanical strength but generally require protective coatings to maintain corrosion resistance and sufficiently low interfacial contact resistance under PEMFC operating conditions. Since current is transferred between the flow-field plate and GDL only through the contacting rib regions, the electrical resistance of the GDL-FFP interface contributes

directly to the cell ohmic losses. The magnitude of the resistance depends on the local contact pressure, real contact area, surface condition, and electrical properties of the contacting materials. Variations in rib geometry and manufacturing tolerances can therefore influence both reactant distribution and local electrical contact conditions [28,29].

1.3.4 Gas diffusion layer

The gas diffusion layer forms the porous interface between the flow-field plate and catalyst layer. Commercial GDLs generally consist of a carbon-fiber substrate, with a microporous layer (MPL) commonly applied on the catalyst-facing side. The fibrous substrate provides mechanical support while enabling transport of reactant gases, liquid water, electrons, and heat. The substrate is commonly treated with a hydrophobic agent, typically polytetrafluoroethylene (PTFE), The substrate is commonly treated with a hydrophobic agent, typically polytetrafluoroethylene (PTFE), to limit flooding and maintain gas-filled pathways for reactant transport.

A thin sublayer, known as the microporous layer (MPL), is commonly coated onto the GDL substrate. It consists of fine carbon particles and a hydrophobic binder, forming a finer pore structure that modifies transport and interfacial conditions between the substrate and catalyst layer [30]. The MPL is introduced to improve contact with the catalyst layer, facilitate water management, and provide a more gradual transition in pore structure between the substrate and catalyst layer.

GDL substrates can be broadly classified according to their corresponding fiber architecture. carbon papers (, SGL) consist of short carbon fibers oriented predominantly within the material plane and bonded by a carbonaceous binder. The planar fiber network produce pronounced anisotropy between the in-plane and through-plane directions. Carbon felts and hydroentangled nonwoven materials instead exhibit a more three-dimensional fiber architecture. Freudenberg GDLs belong to this category and are manufactured by hydroentanglement, which promotes mechanical interlocking between the fibers and reduces the reliance on a carbonaceous binder. Woven carbon cloths represent another class of GDLs and consist of continuous carbon-fiber bundles arranged in an interlaced structure, although this material type was not investigated in the present work.

Representative surface and cross-sectional images of the architectures investigated in this thesis are shown in Fig. 1.3. Differences in fiber orientation, fiber bonding, binder morphology, MPL structure, and hydrophobic treatment are reflected in the mechanical and transport properties discussed in detail in Paper I.

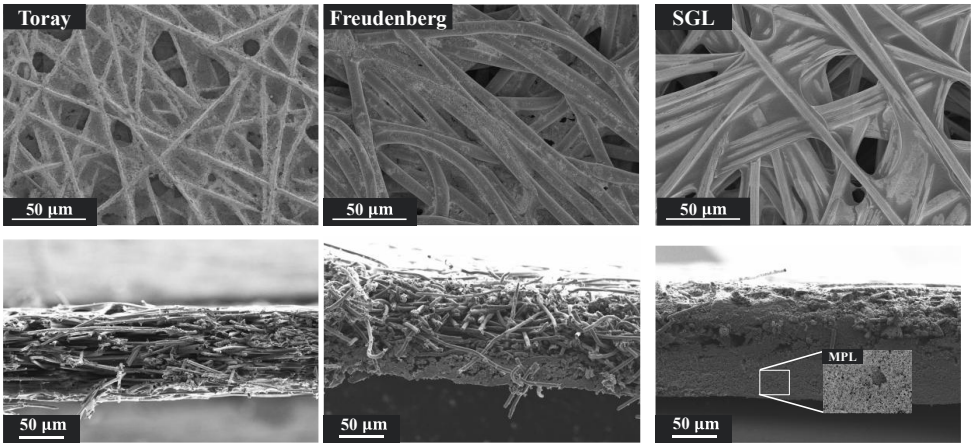

Figure 1.3. SEM images of the three commercial GDLs. Top row: top-view images of three commercially available GDLs.Top row: Field-of-view of Toray TGP-H-060 carbon paper, Freudenberg, and SGL. Bottom row: corresponding cross-sectional images showing the fibrous substrate and MPL.

1.3.5 GDL manufacturing and directionality

The manufacturing route influences GDL properties through the fiber arrangement, inter-fiber bonding, and carbon structure. SGL carbon papers are produced by wet-laid papermaking, in which chopped carbon fibers are dispersed in a liquid suspension and deposited to form a web. Following initial bonding, the paper is impregnated with carbonizable resins and cured. Subsequent carbonization converts the resin into a carbonaceous binder, while further high-temperature treatment promotes structural ordering of the carbon, improving both electrical and thermal conductivity [31] .

The Toray TGP-H series follows a similar route, involving wet-laid sheet formation, resin impregnation, compression, curing, and subsequent carbonization and graphitization. The resulting substrate consists of a predominantly planar fiber network connected by carbonaceous binder. Freudenberg substrates, by comparison, are formed from a dry-laid fiber web that is consolidated by hydroentanglement before carbonization. High-pressure water jets mechanically interlock the fibers, producing a three-dimensional network with pronounced fiber curvature [33,34]. These substrates derive their cohesion primarily from mechanical entanglement rather than a resin-derived binder network. The terms wet-laid and dry-laid describe how the fiber web is formed, whereas hydroentanglement describes how the fibers are subsequently interlocked to provide the web mechanical integrity [32,33].

These manufacturing differences affect mechanical stiffness as well as electrical and thermal conduction. Fiber orientation and inter-fiber bonding govern load transfer and deformation, while conduction depends on both the intrinsic properties of the carbon and the resistance at fiber contacts. Although graphitization generally improves electrical and thermal conductivity, heat and charge transport respond differently to structural disorder and inter-fiber contacts. A material can therefore exhibit relatively high effective electrical conductivity alongside low effective thermal conductivity. Neither property alone provides a direct measure of the degree of graphitization.

Manufacturing also influences directionality. In continuous production, such as the reel-to-reel processing used for SGL GDLs, the direction of web travel defines the machine direction (MD), while the perpendicular in-plane direction is termed the cross-machine direction (CMD). Preferential fiber

alignment during web formation can produce differences between MD and CMD properties. The predominantly planar architecture of carbon papers introduces a further distinction between the in-plane (IP) and through-plane (TP) directions [34] .

The corresponding directions are illustrated in Fig. 1.4. Together, fiber orientation, inter-fiber bonding, and pore connectivity results in direction-dependent mechanical stiffness, diffusivity, permeability, and electrical and thermal conductivity [35].

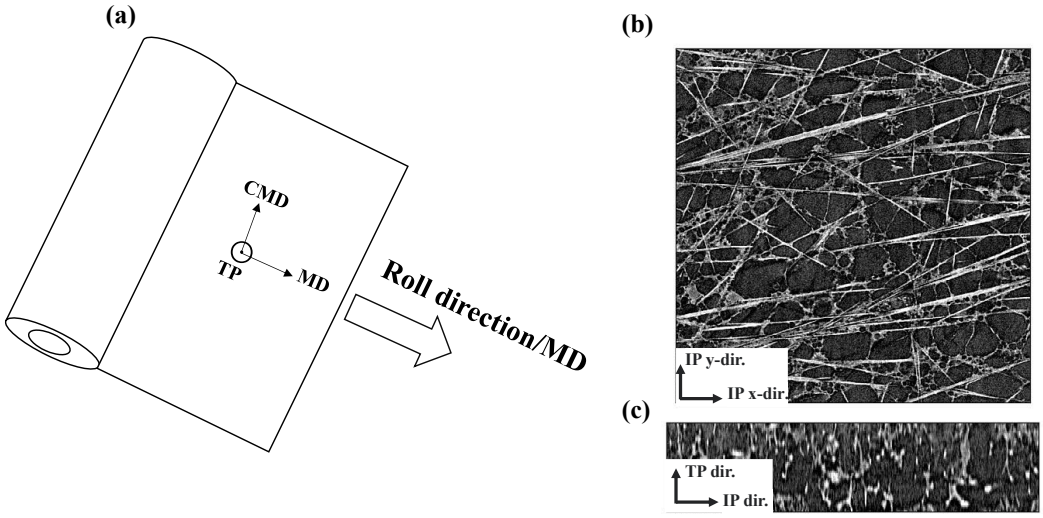

Figure 1.4. Directional terminology for carbon-paper GDLs. (a) Schematic showing the machine direction (MD), cross-machine direction (CMD), and through-plane direction (TP) relative to the material production direction. (b) XCT reconstruction of AvCarb MB30 carbon paper illustrating the predominantly in-plane orientation of the fibrous network

The structural characteristics governing these effective properties, including porosity, pore-size distribution, tortuosity, connectivity, and wettability, are discussed in Section 1.4.

1.3.6 GDL compression

Assembly compression arises from the stack clamping force, which is transmitted from the end plates through the flow-field plates to the membrane-electrode assembly (MEA). Adequate clamping is necessary to maintain structural integrity, provide gas-tight sealing, and limit electrical and thermal contact resistances between adjacent components. Owing to its comparatively low through-plane compressive stiffness, the porous GDL is deformed during stack assembly. The largest compressive strains develop beneath the ribs, where the GDL is loaded directly by the flow-field plate, whereas the channel regions experience less deformation as compressive stresses are redistributed from the neighbouring rib-supported areas. The resulting deformation field is thus governed by the applied clamping pressure, the rib–channel geometry, and the mechanical response of the GDL [36–47]. The characteristic deformation pattern beneath the ribs and channels is illustrated in Fig. 1.5.

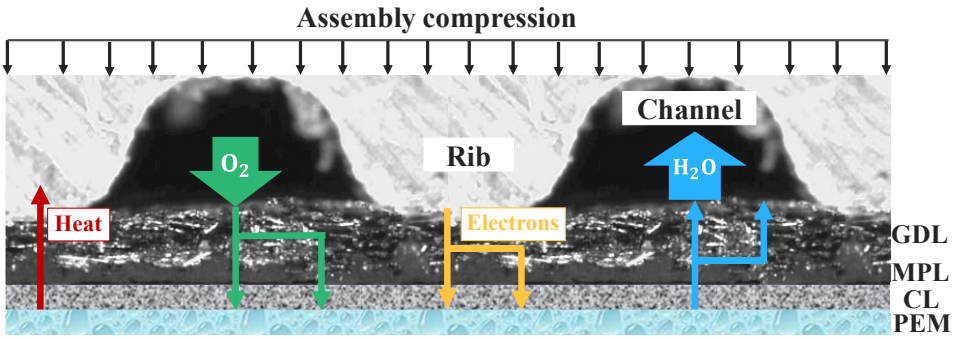

Figure 1.5. Cross-sectional illustration of the cathode GDL beneath the flow-field ribs and channels under assembly compression. Arrows indicate oxygen transport towards the catalyst layer, electron conduction from the ribs towards the catalyst layer, and water and heat removal. GDL: gas diffusion layer; MPL: microporous layer; CL: catalyst layer; PEM: polymer electrolyte membrane.

The resulting non-uniform deformation modifies both the pore network and the solid backbone of the GDL, with direct consequences for mass, charge, and heat transfer. Increasing compressive strain decreases the available pore volume and changes the pore-size distribution, tortuosity, and constriction of gas-transport pathways, thereby increasing resistance to reactant transport [36–42,48–51]. Changes in pore and throat dimensions also affect the capillary response of the porous medium and hence the distribution and displacement of liquid water [39]. Within the solid phase, the increased fiber–fiber contact density under compression enhances both electrical and thermal conduction [45,46,68]. Beneath the ribs, the local contact pressure and true contact area at the GDL–flow-field interface further determines the corresponding electrical and thermal contact resistances [52,53].

These effects establish distinct transport environments beneath the ribs and channels. The compressed rib regions generally provide improved solid-phase conduction and interfacial contact, but at the expense of reduced pore space for gas and liquid transport. By contrast, the less compressed channel regions keep a more open pore structure, while the lower fiber–fiber contact density results in lower effective electrical and thermal conductivities. Consequently, charge and heat generated beneath the channels must partly be conducted laterally towards the adjacent ribs. The compression state of the GDL, together with the flow-field geometry, therefore, controls the spatial distribution of mass-transport and conductive resistances within the porous layer. Stack compression consequently represents a compromise between minimizing electrical and thermal losses and maintaining a pore structure that supports reactant and liquid-water transport.

1.4 GDL structure

The effective properties of a GDL are governed by the architecture and connectivity of its fibrous substrate and microporous layer (MPL). The substrate comprises an interconnected carbon-fiber network characterized by relatively large pores and pronounced structural anisotropy, whereas the MPL consists predominantly of carbon-black agglomerates combined with a hydrophobic binder and exhibits a substantially finer pore structure. The contrast in characteristic length scales results in distinct transport regimes and capillary transport within the two layers. Consequently, the macroscopic behaviour of the GDL reflects not only the properties of the substrate and MPL individually, but also their combined contribution to gas and liquid-water transport, electron conduction, and heat transfer between the flow field and catalyst layer.

At the pore scale, effective transport is determined by the geometry and continuity of the pathways available within each phase. Porosity and pore-size distribution characterize the volume and dimensions of the void space, whereas tortuosity and connectivity describe the extent to which the pore space provides continuous pathways through the material. Moreover, the arrangement, orientation, and interconnection of the carbonaceous solid network determine the mechanical response and its ability to conduct electrons and heat. These morphological characteristics therefore provide the structural basis for the effective-property relationships employed throughout this thesis.

1.4.1 Porosity and pore-size distribution

Porosity is a fundamental property of porous materials and is defined as the fraction of the bulk volume occupied by pore space [54]:

$$\phi = \frac{V_{\mathrm{pore}}}{V_{\mathrm{tot}}} \tag{1.6}$$

where V_{pore} and V_{tot} denote the pore volume and total bulk volume, respectively. Although porosity quantifies the overall void fraction, it provides no information on the spatial distribution or characteristic dimensions of the pore space. Materials with comparable porosities may therefore exhibit different transport behaviour depending on their pore-size distribution, pore-throat dimensions, and network morphology.

The combination of substrate and MPL gives the GDL a hierarchical pore architecture spanning multiple characteristic length scales. The size and connectivity of pores and pore throats influence both gas-phase transport and liquid-water invasion. Larger pores generally provide less restrictive pathways for gas transport, whereas the constrictions between neighbouring pores strongly influence the capillary pressure required for liquid-water invasion. Mechanical compression and prolonged operation can modify the pore geometry and thereby change the effective transport properties of the GDL. In this thesis, the pore architecture is characterized using complementary intrusion based and X-ray imaging techniques.

1.4.2 Tortuosity, connectivity, and percolation

Porosity specifies the volume available for transport but does not capture the geometry or continuity of the underlying pathways. Within a porous medium, transport pathways are typically longer and more convoluted than the corresponding macroscopic distance. The geometric tortuosity in direction q may be expressed as [55] :

$$\tau_{g,q} = \frac{L_{\mathrm{eff,q}}}{L_q}, q \in \{\mathrm{ip}, \mathrm{tp}\} \tag{1.7}$$

Where $L_{\mathrm{eff,q}}$ is the effective path length through the porous structure and L_q is the corresponding straight-line distance. Connectivity, by contrast, describes the extent to which the pore space forms continuous pathways through the material. Tortuosity and connectivity thus represent complementary aspects of pore architecture that influence effective transport.

Percolation refers to the establishment of a continuous network when the volume fraction of a given phase exceeds a critical threshold [56]. In commercial GDLs, the carbonaceous solid phase generally forms an interconnected conducting network well above the critical threshold. Differences in electrical and thermal conductivity are therefore governed primarily by fiber orientation, the density and quality of fiber–fiber contacts, and the associated contact resistances rather than by the onset of

solid-phase percolation [57–59]. Gas transport depends on the connectivity of the pore space, while the spatial distribution of water determines whether continuous liquid pathways develop during two-phase operation. Tortuosity, pore constrictions, and connectivity influence both permeability and effective diffusivity, while liquid water occupying critical pore throats can further reduce gas transport. The corresponding effective transport properties are introduced in Section 1.4.3.

1.4.3 Gas transport

Gas transport through the GDL occurs through both pressure-driven flow and molecular diffusion. These processes are characterized by different effective properties. Intrinsic permeability, $\boldsymbol{K}$, characterizes the resistance of the pore structure to pressure-driven flow and is independent of the fluid properties within the Darcy regime [60,61] :

$$u_{\alpha,q} = -\frac{K_q k_{r,\alpha}(S)}{\mu_\alpha}\frac{\partial p_\alpha}{\partial q}, \alpha \in \{g, l\} \tag{1.8}$$

Where $u_{\alpha,q}$, μ_α, and $\nabla p_{\alpha,q}$ denote the superficial velocity, viscosity, and pressure of phase α, respectively, and $k_{r,\alpha}(S)$ the relative permeability. Under single-phase conditions, $k_{r,\alpha}(S) = 1$, whereas under two-phase conditions $k_{r,\alpha}(S) \leq 1$ accounts for the reduction in phase mobility caused by occupation of the pore space displaced by the other fluid phase. The intrinsic permeability is generally anisotropic in fibrous GDLs because of the preferential in-plane fiber orientation (see Fig.1.4).

In the finer pores of the MPL, gas slip at the pore walls can increase the apparent permeability above the intrinsic permeability of the porous structure. The pressure dependence on gas permeability is commonly described by the Klinkenberg relation [62]:

$$K_{\text{app}} = K_\infty \left(1 + \frac{b}{\bar{p}}\right) \tag{1.9}$$

Where K_∞ is the intrinsic permeability approached when gas-slip effects become negligible, b is the Klinkenberg slip coefficient, and $\bar{p}$ is the mean gas pressure.

Effective diffusivity, $\boldsymbol{D}^{\text{eff}}$, describes diffusive transport through the connected pore space relative to the corresponding bulk-gas diffusivity. In the dry state it may be expressed as:

$$D^{\text{eff}}_{\text{dry},q} = \frac{\phi}{\tau_{D,q}} D_{\text{bulk}} \tag{1.10}$$

Where ϕ is the porosity of the porous domain and D_{bulk} is the bulk diffusivity. In contrast to the geometric tortuosity in Eq.1.7, τ_D is an effective transport parameter that accounts for pore constrictions and connectivity on diffusive transport. During two-phase operation, partial saturation within the pore space reduces gas saturation accordingly:

$$D^{\text{eff}}_q(S) = D^{\text{eff}}_{\text{dry},q} D_{\text{rel},q}(S) \tag{1.11}$$

where $D_{\text{rel},q}(S) = 1$ denotes the dry state. As liquid-water saturation increases, the available gas-filled pore volume decreases, thereby reducing the effective gas diffusivity.

The small characteristic pore diameters of the MPL increase the relative importance of gas–wall collisions compared with intermolecular collisions. Under these conditions, molecular and Knudsen diffusion can be combined using the Bosanquet relation:

$$D_B = \left(\frac{1}{D_M} + \frac{1}{D_K}\right)^{-1} \tag{1.12}$$

where D_M and D_K denote the molecular and Knudsen diffusivities, respectively. The specific compression- and saturation-dependent permeability and diffusivity relations used in this thesis are introduced in Chapter 4.

1.4.4 Wettability and capillary pressure

Wettability describes the interaction between a liquid and a solid surface and is commonly characterized by the contact angle, θ. Surfaces with $\theta < 90°$ are generally considered hydrophilic, whereas $\theta > 90°$ indicates a hydrophobic surface. In GDLs, wettability is governed by the surface chemistry and morphology as well as by the spatial distribution of the hydrophobic phase [63].

Within a porous medium, wettability and pore geometry coolectively determine the capillary pressure required for liquid invasion. Capillary pressure is defined as the pressure difference between the non-wetting and wetting phase:

$$p_c = p_{\mathrm{nw}} - p_w = p_l - p_g \tag{1.13}$$

Where P_{nw} and P_w denote the pressures of the non-wetting and wetting phases, respectively. In a hydrophobic GDL, liquid water generally constitutes the non-wetting phase. For an idealized pore throat, the Young–Laplace relation relates the invasion pressure to the interfacial tension, contact angle, and pore-throat size. Consequently, the invasion of smaller pore throats generally requires higher capillary pressures.

As illustrated in Fig. 1.6, increasing capillary pressure allows liquid water to invade a progressively larger fraction of the pore network, resulting in increased saturation. At the continuum scale, this response is described by a capillary pressure–saturation relation, $P_c(S)$. Such relations can be obtained from intrusion measurements or spatially resolved X-ray imaging [64–68] . Bulk measurements provide the overall saturation response, whereas imaging also reveals how the invading liquid is distributed within the material.

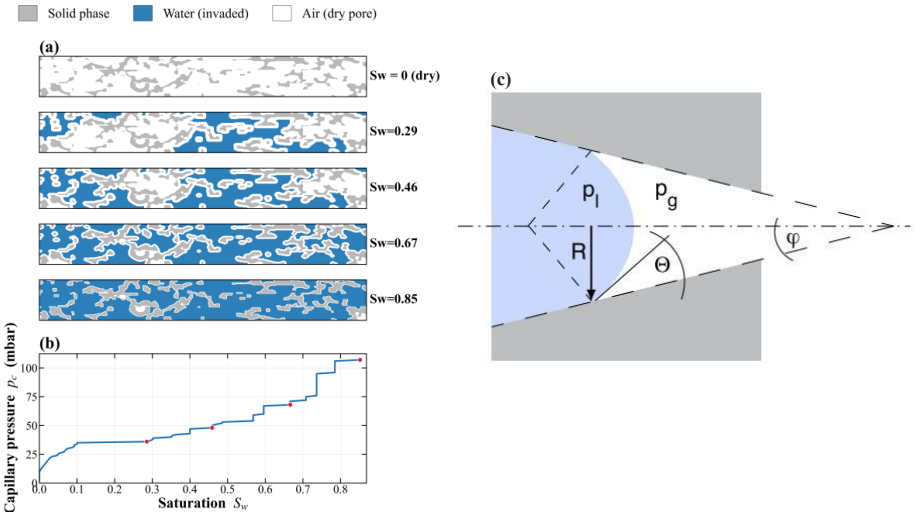

Figure 1.6. Illustration of capillary invasion and pore-throat geometry in a hydrophobic GDL. (a) Pore-morphology-method (PMM) simulations showing progressive water invasion of the pore space with increasing

saturation. (b) Corresponding capillary pressure–saturation relation obtained from the simulated invasion sequence. (c) Schematic representation of a gas–liquid meniscus in a converging pore throat, illustrating the relation between liquid pressure p_l, gas pressure p_g, meniscus radius R, contact angle θ, and throat opening angle φ. (c) adapted from [15].

1.5 Ageing of gas diffusion layers

Gas diffusion layers are exposed to mechanical, thermal, and chemical stresses during fuel cell operation, which can progressively alter the microstructure, wettability, and transport properties. Mechanical degradation may result from sustained compression and load cycling, leading to irreversible deformation, fiber rearrangement, local buckling, or fiber fracture [69]. Chemical ageing can involve carbon-surface oxidation and degradation or redistribution of hydrophobic PTFE treatment, thereby modifying the interaction between the pore structure and liquid water [70].

These processes can change porosity, pore-size distribution, connectivity, and wettability, with corresponding consequences for gas transport, capillary behaviour, and electrical and thermal conduction [70–72]. Since degradation processes originate at the pore scale, image-based characterization techniques have become increasingly important for studying ageing phenomena in GDL materials [73].

Much of the existing understanding of GDL degradation is derived from accelerated stress tests (ASTs) designed to promote specific ageing mechanisms within experimentally practical timescales. Although these protocols provide valuable insight into individual degradation processes, they may not reproduce the combined mechanical, thermal, and chemical exposure encountered during prolonged stack operation. Evidence from GDLs recovered from operated fuel cell stacks remains comparatively limited, particularly regarding how changes in pore structure and wettability jointly affect capillary transport, local saturation distribution and saturation dependent transport properties. This thesis addresses this gap by combining structural characterization, wettability measurements, and capillary pressure-resolved imaging of water distributions in stack aged GDLs and pristine reference material.

1.6 Imaging of water in PEMFCs

Spatially resolved characterization of liquid water is important because bulk saturation alone does not reveal how water is distributed within the porous structure. Several imaging approaches have been applied to PEMFCs, including neutron and X-ray radiography and tomography, optical methods, and magnetic-resonance techniques [74–77]. Neutron imaging provides high sensitivity to water and is particularly suitable for cell- and channel-scale measurements, whereas X-ray methods provide higher spatial resolution and are therefore well suited to resolving water within the GDL and MPL [74,75].

Synchrotron X-ray computed tomography (XCT) enables three-dimensional characterization of both the porous microstructure and liquid-water distribution, allowing local saturation, through-plane water profiles, and cluster morphology to be related directly to the underlying pore structure [76–78]. The principal limitations arise from trade-offs between spatial resolution, field of view, and temporal resolution, together with uncertainties associated with image registration and phase segmentation. Nevertheless, XCT provides a direct means of relating pore structure, wettability, and water distribution and is therefore particularly suitable for the ageing analysis presented in this thesis.

1.7 Modelling strategies

Modelling has become an important tool for understanding the coupled transport and electrochemical processes occurring in a PEMFC. Depending on the quantities of interest, models span several characteristic length scales, ranging from transport within individual pores to complete cells, stacks and fuel-cell systems [79–81]. Accordingly, modelling approaches can broadly be divided into continuum-scale and pore-scale methods. Continuum models represent porous components as homogenized media and are predominantly used to investigate transport and electrochemical processes at the membrane electrode assembly (MEA) and unit cell scales. Pore-scale models instead represent the porous microstructure explicitly and can therefore establish direct relationships between material structure and transport behaviour [81]. More recently, physics-based continuum models have increasingly been complemented by surrogate modelling and numerical optimization, enabling computationally efficient exploration of large parameter and design spaces [82–86].

1.7.1 Continuum models

Continuum models constitute a widely used framework for describing coupled transport and electrochemical processes in PEMFCs [87]. The detailed pore and fiber structures of porous components such as the GDL, microporous layer (MPL), and catalyst layer (CL) are not explicitly resolved. Instead, each domain is represented as a homogenized medium characterized by effective properties including porosity, permeability, diffusivity, and electrical and thermal conductivity [79,88]. The influence of the underlying microstructure therefore enters through constitutive relations and effective material properties rather than through explicit resolution of the pores and solid components that constitute the solid network.

The required spatial dimensionality depends on the phenomena of interest. One-dimensional models primarily resolve transport through the MEA thickness, whereas two-dimensional formulations can additionally capture spatial variations associated with rib–channel geometry. Three-dimensional models further resolve variations along the flow-field channels [81].

Increasing dimensionality does not remove the underlying homogenization of the porous components, and predictive capability therefore remains dependent on appropriate constitutive relations and effective properties. The specific continuum formulation employed in this thesis is presented in Chapter 4.

1.7.2 Pore-scale modeling and upscaling

Pore-scale approaches preserve the spatially resolved microstructure that is lost through continuum homogenization, including the local arrangement of pores, fibers, and binder. Advances in X-ray computed tomography (XCT) have made it possible to reconstruct three-dimensional GDL structures and analyze their morphology and transport characteristics directly. Depending on the quantity of interest, these reconstructions can be examined using pore-network models, pore-morphology methods, lattice-based methods, or direct numerical simulation (DNS) [46,89–93].

Morphology-based methods characterize geometrical accessibility, connectivity, and invasion behaviour without explicitly solving the complete transport equations and have, for example, been applied to predict liquid-water invasion and capillary pressure–saturation behaviour in reconstructed GDL structures [94]. By contrast, direct numerical simulation (DNS) solves the relevant transport equations directly on the voxel-resolved geometry, thereby capturing the effects of pore connectivity, tortuosity, constrictions, and microstructural anisotropy on the local transport fields.

Pore-scale and continuum models consequently provide complementary descriptions of porous-media transport. Transport fields obtained from a resolved microstructure can be upscaled to provide effective properties used for continuum modeling. For diffusion, the volume-averaged pore-scale flux can be related to the macroscopic concentration gradient through the effective diffusivity tensor:

$$\langle \boldsymbol{N} \rangle = -\boldsymbol{D}^{\mathrm{eff}} \nabla \langle c \rangle \tag{1.14}$$

Similar procedures can be applied to determine permeability and effective thermal and electrical conductivities. Such upscaling is inherently associated with loss of information: the explicit pore geometry and local fields are replaced by a smaller number of effective parameters. The validity therefore requires that the pore-scale domain adequately represents the material at the continuum scale. This requirement is commonly expressed through the concept of a representative elementary volume (REV). Importantly, the required REV can depend on the property being evaluated; a volume that is representative with respect to porosity is not necessarily representative with respect to connectivity or transport [95,96].

1.8 Surrogate modeling and multi-objective optimization

Increasing physical resolution is generally accompanied by increased computational cost. Detailed three-dimensional continuum models and pore-scale simulations can therefore become prohibitively expensive when large numbers of parameter combinations must be evaluated. This is particularly restrictive in design optimization, sensitivity analysis and uncertainty quantification, where hundreds or thousands of model evaluations may be required. Surrogate modelling provides a complementary approach in which a computationally inexpensive approximation is constructed from a limited number of evaluations of the underlying continuum model [97–99]:

$$\hat{\mathbf{y}} = \hat{f}(\mathbf{x}) \approx f(\mathbf{x}) \tag{1.15}$$

Where $\mathbf{x}$ contains the model inputs or design variables and $\mathbf{y}$ represents the model outputs. Once trained, the surrogate can be evaluated at lower computational cost than the underlying physics-based model.

Surrogate and machine-learning methods have increasingly been applied to PEMFC flow-field and component design, operating-condition optimization, degradation prediction, stack modelling, and system-level optimization [98,99]. Among available approaches, Gaussian-process ($\mathcal{GP}$) regression is particularly suitable for data-efficient optimization since it provides both a predicted response and an associated estimate of uncertainty [100–102]. This uncertainty can be exploited by Bayesian optimization to balance exploration of under sampled regions against exploitation of regions expected to provide improved performance [103]

Engineering design commonly involves several competing objectives for which no single design simultaneously optimizes all quantities of interest. A solution is termed non-dominated if no objective can be improved without degrading at least one other objective. The collection of non-dominated solutions forms the Pareto front and represents the available trade-offs between the objectives, as illustrated in Fig. 1.7.

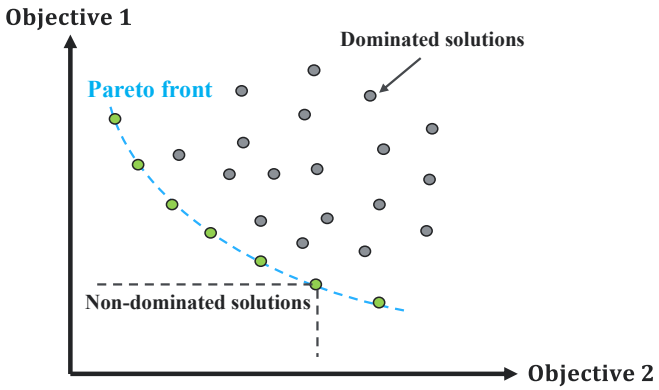

Figure 1.7. Conceptual illustration of a bi-objective minimization problem. Green markers indicate non-dominated solutions forming the Pareto front, while grey markers represent dominated solutions.

Bayesian optimization combines a probabilistic surrogate with an acquisition function that determines which candidate designs should subsequently be evaluated using the physics-based continuum model. The surrogate is updated as new high-fidelity observations become available, allowing the design space to be explored sequentially while limiting the number of expensive model evaluations [104]. For multi-objective design problems, acquisition functions can preferentially select candidates expected to improve the current Pareto front.

A further challenge arises when the same design problem is considered under different operating conditions. Constructing an independent surrogate and optimization campaign for every condition can require many additional high-fidelity simulations. Information obtained at one operating condition may therefore be transferred to another, if changes in the underlying response are appropriately represented. The specific $\mathcal{GP}$ formulations, multi-objective Bayesian optimization strategy, and transfer approach employed in this thesis are described in Chapter 4.

1.9 Knowledge gaps and thesis scope

Despite extensive research on gas diffusion layers, translating experimentally determined material properties into criteria for GDL selection remains challenging. Assembly compression simultaneously influences mechanical behaviour, electrical and thermal conduction, and gas transport, while fuel cell performance depends on flow-field geometry and operating conditions. A central question is how directional mechanical and transport properties should be considered jointly when cell performance, current density uniformity, and electrical contact resistance impose competing requirements. Further uncertainties concern the influence of native binder on PTFE distribution and oxygen transport, and how changes in pore structure and wettability following prolonged operation affect capillary water invasion and gas diffusivity.

This thesis addresses these questions through complementary experimental characterization, pore-scale analysis, and continuum modelling. Experimental characterization establishes the nonlinear compressive response and directional elastic stiffness of the investigated GDLs, together with the compression dependence of their electrical conductivity, thermal conductivity, and gas transport. Complementary investigations examine how substrate architecture influences PTFE distribution and oxygen-transport resistance, and how prolonged stack operation affects pore structure, wettability, water invasion, and effective diffusivity. A Multiphysics PEMFC model is used to investigate the combined influence of GDL mechanical properties and flow-field geometry on cell performance,

while surrogate-assisted multi-objective optimization examines competing design requirements and the transferability of favourable designs across operating conditions.

The investigations are subject to several experimental and modelling limitations. Compression-dependent in-plane and through-plane effective gas diffusivities were not measured directly in the material-characterization campaign, either under dry or partially saturated conditions, and were instead represented using empirical relations. The ageing analysis was primarily limited by the small thickness of the fibrous GDL substrate available for pore-scale characterization due to substantial intrusion of the microporous layer (MPL). The ageing analysis was primarily limited by the limited thickness of the fibrous GDL substrate available for pore-scale characterization due to significant intrusion of the microporous layer (MPL). Consequently, the analysed substrate volume was insufficient to establish a representative elementary volume in the through-plane direction.

Furthermore, the 2 μm voxel resolution was insufficient for reliable quantification of internal contact-angle distributions, restricting wettability characterization to measurements of apparent external contact angles and leaving local wettability variations within the pore structure unresolved. Furthermore, the optimization independently varied material-property multipliers within prescribed design and operating domains, without establishing whether all resulting property combinations are physically realizable. The proposed design relationships therefore provide guidance for material screening and GDL–flow-field optimization, while their quantitative applicability beyond the investigated conditions requires further experimental validation.

2. Materials and experimental methods

This chapter describes the materials and experimental methods used in the studies comprising this thesis. The investigated GDLs are first introduced, followed by the methods used to characterize their mechanical, thermal, electrical, gas-transport, and structural properties. The experimental procedures used to investigate the influence of native carbonaceous binder on PTFE distribution and wettability are then summarized. Finally, the methods used for X-ray computed tomography (XCT) characterization of pristine and aged GDLs, including pressure-controlled water invasion and image-based structural analysis, are presented.

2.1 Investigated GDL materials

Several commercial GDL materials were investigated across the studies comprising this thesis. The materials were selected to represent differences in substrate architecture, hydrophobic treatment, native binder content, and the presence or absence of a microporous layer (MPL). Different subsets were employed depending on the objectives of each study, as summarized in Table 2.1.

Table 2.1. Overview of the GDL materials employed in the studies comprising this thesis

Study	Material designation	Principal characteristics	Role
Paper I	Toray TGP-H-60	Batch-produced carbon paper, no MPL; two PTFE loadings	Mechanical and compression-dependent transport properties
	SGL 29BA	PTFE-treated roll-good carbon paper, no MPL	
	SGL 28BC	PTFE-treated roll-good carbon paper with MPL	
	Freudenberg H23C7	PTFE-treated roll-good carbon felt with MPL	
Paper II	Freudenberg H23	Carbon felt substrate, no PTFE, MPL loading	PTFE treatment and microstructural characterization
	SGL 39AA	Carbon paper substrate, no PTFE, MPL loading	PTFE treatment and microstructural characterization
Paper III	GDL-X	PTFE-treated roll-good carbon paper with MPL	Physics-based continuum modeling
Paper IV	GDL-X	PTFE-treated roll-good carbon paper with MPL	Physics-based continuum modeling and surrogate-assisted optimization
Paper V	AvCarb MB30	PTFE treated roll-good carbon paper with MPL	Image-based characterization

The materials include both predominantly planar carbon-paper structures (SGL, Toray,AvCarb) and interconnected nonwoven materials (Freudenberg), with and without MPLs and hydrophobic treatment. These differences provide a basis for comparing the influence of GDL structure and composition on mechanical and transport behaviour. For commercially sensitive material GDL-X, the manufacturer-specific grade designation is not disclosed; the material is therefore referred to by the

anonymized designation used throughout this thesis. Toray TGP-H-060 carbon paper is used as a reference material.

2.2 Ex-situ material characterization

The ex-situ characterization was designed to establish an internally consistent set of mechanical, transport, and structural properties for the investigated GDLs to quantify the compression dependence of those properties that change during assembly compression. The measurements served two purposes: to identify how differences in GDL architecture govern the mechanical and transport response, and to provide experimentally based material parameters and constitutive relations for the continuum model. Characterization comprised through-plane compression moduli, in-plane bending moduli, through-plane shear moduli, direction-dependent electrical conductivity, through-plane thermal conductivity, in-plane gas permeability, and mercury intrusion porosimetry. Where applicable, the properties were determined as functions of local compression. Detailed experimental procedures are provided in Paper I.

2.2.1 Mechanical properties

The mechanical properties of the GDLs were characterized using designated through-plane compression, three-point bending, and through-plane shear measurements. Through-plane compression provided the stress–strain response and compressed thickness (Fig. 2.1a), while direction-dependent in-plane bending moduli were obtained from three-point bending tests (Fig. 2.1c). The short-beam method was adapted to thin, highly compressible GDLs using a micrometer-controlled adjustable gap, allowing the deformation mode to be shifted towards through-plane shear and reducing uncertainty associated with the effective shear span and sample thickness, as shown in Fig. 2.1b, d.

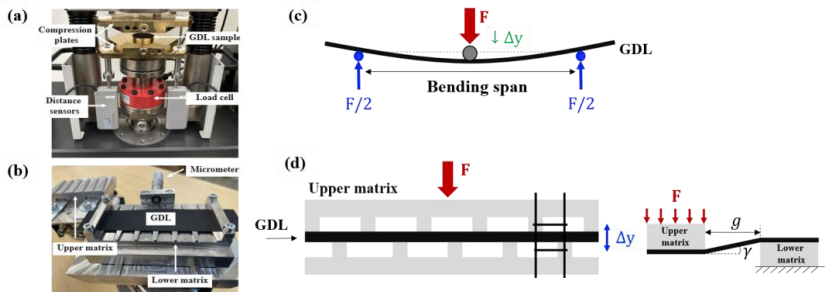

Figure 2.1. Experimental configurations used for mechanical characterization of the GDLs: (a) uniaxial compression setup with load-cell and displacement measurements, (b) through-plane shear test fixture, (c) schematic of the three-point bending configuration with applied force F and bending span, and (d): schematic representation of the shear deformation between the upper and lower matrices, defining the shear gap, g, and shear angle, γ.

2.2.2 Electrical and thermal properties

Electrical transport was characterized in both the through-plane and in-plane directions. The through-plane effective electrical conductivity, $\sigma_{\mathrm{tp}}^{\mathrm{eff}}$ was measured under compressive stresses up to 3 MPa using GDL specimens positioned between gold-coated electrodes. The applied compressive stress and compressed thickness were measured simultaneously, and a stacking procedure was used to separate the bulk GDL resistance from the external electrode contact resistance. For MPL-coated materials, the

substrate, MPL, and internal substrate-MPL interface could not be separated experimentally; the reported conductivity therefore represents the effective response of the complete GDL–MPL assembly.

The in-plane electrical conductivity was measured using a four-point configuration to minimize the contribution of electrode contact resistance. Measurements were performed separately in the machine direction (MD) and cross-machine direction (CMD), thereby quantifying differences in electronic transport within the material plane. The through-plane and in-plane electrical configurations are illustrated in Fig. 2.2a and b.

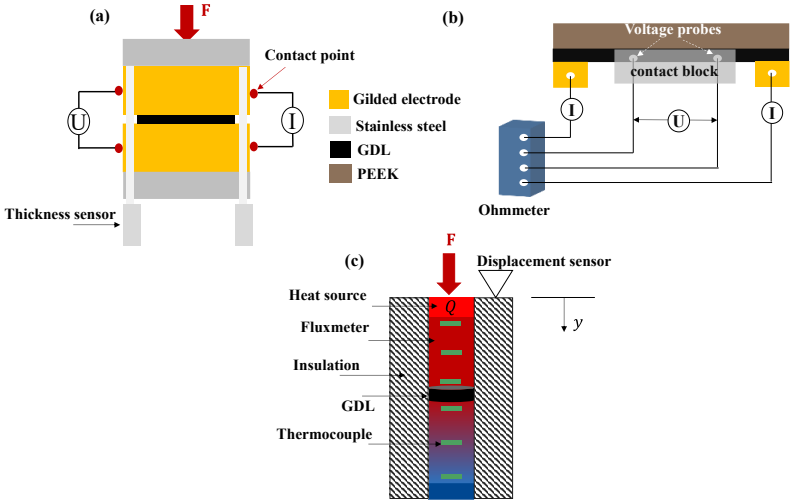

Figure 2.2. Schematic configurations used for electrical characterization of the GDLs: (a): through-plane electrical resistance measurement under controlled compression between gold-coated stainless-steel electrodes, with simultaneous monitoring of specimen thickness (b): four-point probe configuration for measurement of in-plane sheet resistance, where current I is applied through the outer electrodes and the voltage drop U is measured between the inner probes.

Through-plane thermal conductivity was measured under compression using a steady-state guarded heat-flux method (Fig.2.2d) at 80 ℃ and compressive stresses up to 3 MPa. The heat flux was determined from the temperature gradients measured across calibrated flux meters positioned on either side of the specimen. For MPL-coated materials, the reported κ_{tp}^{eff} therefore represents the effective conductivity of the complete GDL substrate-MPL assembly.

2.2.3 In-plane gas permeability

In-plane gas permeability was measured under compression using a radial-flow method [105,106], whereby an annular GDL specimen was compressed between two parallel plates, while air was introduced through the inner radius and transported radially through the material. The permeability was determined from the measured pressure drop and gas flow rate using Darcy's law, with the compressed GDL thickness measured simultaneously. Measurements were performed at compressive stresses up to 3 MPa to determine the compression dependence of the in-plane permeability. Only the in-plane permeability was measured experimentally in the present work.

2.2.4 Characterization of the GDL pore structure

The pore structure of the investigated GDLs was characterized using mercury intrusion porosimetry (MIP), providing the cumulative pore volume, pore-size distribution, and total porosity. Because mercury is non-wetting within the GDL pore structure, increasing pressure progressively accesses smaller pore throats, with the corresponding characteristic pore dimensions determined using the Washburn equation [107]. The resulting values should be interpreted as effective pore dimensions because the conversion assumes an idealized pore geometry rather than the irregular geometry of the actual fibrous and MPL pore networks.

The measured pore-size distributions were subsequently used to formulate capillary and saturation-dependent transport relations employed in the two-phase continuum model, including the capillary pressure-saturation, relative permeability, and relative gas diffusivity relations described in Chapter 4.

2.3 PTFE distribution and oxygen transport resistance

The role of the native substrate structure in controlling PTFE deposition was investigated using two GDL substrates with contrasting binder morphologies: binder-free Freudenberg H23 (F-H23) and binder-containing SGL 39AA (39AA). The experimental approach combined controlled PTFE treatment with spatially resolved Raman spectroscopy and SEM/EDX analysis to relate the deposited PTFE to the underlying microstructure. Contact-angle and limiting-current density measurements were subsequently used to examine how these microstructural differences affected external wettability and dry oxygen transport resistance. The contribution of this study lies in linking the native substrate architecture to the spatial distribution of subsequently applied PTFE and to the resulting transport behaviour, rather than treating nominal PTFE loading as the sole descriptor of hydrophobic treatment. Detailed experimental procedures are provided in Paper II [108].

2.3.1 PTFE treatment and microstructural characterization

The substrates were hydrophobically treated by dip coating in aqueous PTFE dispersions to obtain nominal PTFE loadings of 5, 20, and 50 wt.%, followed by drying and thermal treatment. The actual PTFE uptake was determined gravimetrically from the change in specimen mass. The resulting mean loadings were approximately 7.3, 20.7, and 48.5 wt.% for F-H23 and 5.0, 19.5, and 56.5 wt.% for SGL 39AA, respectively.

The spatial distribution of PTFE was characterized primarily using confocal Raman spectroscopy. Carbon and PTFE were distinguished from their characteristic Raman responses, enabling spatial maps of the two phases to be generated at the GDL surface and across sectioned specimens. The measurement principle and representative spectral discrimination are illustrated in Fig. 2.3.

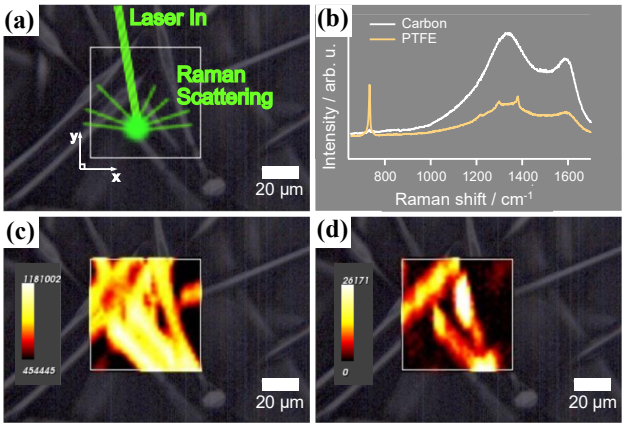

Figure 2.3. Raman spectroscopic mapping used to distinguish carbon and PTFE within the GDL substrate: (a) schematic of the laser excitation and Raman-scattering measurement area, (b) representative Raman spectra of carbon and PTFE showing the spectral features used for phase discrimination, (c) spatial map of the carbon signal, and (d) corresponding spatial map of the PTFE signal. The maps illustrate the local distribution of the carbonaceous phase and PTFE within the investigated region.

SEM was used to characterize the fiber and native-binder morphology, while EDX mapping provided complementary information on the fluorine distribution as an indicator of PTFE. Raman and SEM/EDX measurements were performed at corresponding locations, allowing the spatial distribution of PTFE to be related directly to the underlying substrate structure. Further experimental details are provided in Paper II [108].

2.3.2 Wettability and oxygen transport resistance

The effect of PTFE treatment on the external wettability of the GDL substrates was evaluated using sessile-drop contact-angle measurements with deionized water. Measurements were performed at several locations on each specimen, and the reported values represent the mean contact angle after the droplets had reached an approximately stationary shape. The measurements were used to assess differences in surface wettability associated with PTFE loading and substrate structure.

Dry oxygen transport resistance (DOTR) was determined from limiting-current measurements using the approach originally introduced by Baker et.al [109]. The cell was operated at low oxygen concentrations, and the voltage was progressively reduced until oxygen transport to the cathode catalyst layer became rate limiting. Under these conditions, the limiting current density provides a measure of the total resistance to oxygen transport through the cell.

Measurements were performed in a single-cell configuration using the two GDL materials at selected PTFE loadings. High reactant flow rates were used to approach differential operating conditions and thereby limit changes in gas composition and thereby minimize changes in gas composition and relative humidity (RH) gradients between inlet and outlet. The detailed operating conditions and cell configuration are provided in Paper II.

Measurements were performed for both GDL substrates at selected PTFE loadings. For each oxygen concentration, the cell voltage was reduced until a limiting-current plateau was obtained. The corresponding limiting current density was used to calculate the total dry oxygen transport resistance according to:

$$R_{\mathrm{tot}}^{\mathrm{O_2,dry}} = \frac{4\mathcal{F}x_{\mathrm{O_2}}^{\mathrm{dry}}}{j_{\mathrm{lim}}} \frac{p_{\mathrm{abs}} - p_{H_2O}}{\mathcal{R}T} \tag{2.1}$$

where p_{abs} is the absolute cell pressure, $p_{\mathrm{H_2O}}$ is the water-vapour partial pressure, $\mathcal{R}$ is the universal gas constant, T is the cell temperature, and j_{lim} is the limiting current density. The water-vapour pressure was determined from the inlet relative humidity. Measurements were performed for the two lower PTFE loadings; the highest-loading samples were excluded since stable cell conditioning could not be achieved.

2.4 Image-based characterization

The image-based study examined how long-term fuel-cell operation alters GDL pore structure, wettability, liquid-water invasion, and gas-phase transport. A pristine GDL was compared with material recovered from a PEM fuel-cell stack after approximately 20,000 h of operation. External wettability measurements and pressure-controlled water-injection X-ray Computed Tomography (XCT) were combined with pore-scale transport calculations to relate ageing-induced changes in structure and wetting to the three-dimensional water distribution at various capillary pressures and to the corresponding gas-phase transport. Full experimental details are provided in Paper V.

2.4.1 Materials and sample selection

An AvCarb MB30 GDL consisting of a PTFE-treated carbon-fiber substrate with an MPL was investigated in pristine and aged states. The aged material was recovered from a PEM fuel-cell stack after approximately 20,000 h of stack operation. Samples from different locations of the most degraded cell were initially screened with respect to external wettability, after which one aged location was selected together with pristine material for pore-scale analysis.

External wettability was characterized using sessile-drop and Wilhelmy measurements, providing static as well as advancing and receding contact angles on the substrate and MPL surfaces. These measurements were primarily used to identify an aged region exhibiting a pronounced change in wetting behaviour for subsequent water-invasion experiments.

Table 2.1. Mean GDL substrate thickness and relative thickness change measured under the applied compression during XCT acquisition for pristine and aged materials sampled from different locations in the MEA.

Sample	Mean Thickness (µm)	Relative thickness change (%)	Thickness XCT (µm)	Compression (%)
Pristine	193.2	–	151.7 ± 4.4	21.5
Anode inlet	172	-11	140.3 ± 4	18.4
Anode outlet	174.9	-9.5	138.6 ± 4	20.8
Cathode inlet	176.4	-8.7	142.2 ± 1.9	19.4
Cathode outlet	178.9	-7.4	146.1 ± 2.5	18.3

2.4.2 Water injection measurements

For the tomographic water-injection experiments, three circular GDL samples were stacked in a PEEK sample holder following the general configurations reported by Lamibrac et al. and Chen et al.

[65,110]. Hydrophilic membranes were used to distribute water between the samples, while a hydrophobic membrane at the outlet facilitated air removal and retained liquid water within the assembly. The experimental configuration is shown in Fig. 2.4.

Prior to water injection, a dry XCT scan of the GDL assembly was acquired as a reference. Deionized water was then introduced from the bottom of the sample holder, and the pressure was increased stepwise from 15 to 1000 mbar to characterize the capillary-pressure–saturation response. At each pressure level, the system was allowed to equilibrate for 10 min before image acquisition, with the imposed pressure maintained throughout the scan. The monotonic water-invasion sequence from the initially dry state followed primary drainage. XCT images were acquired at a voxel size of approximately 2 µm.

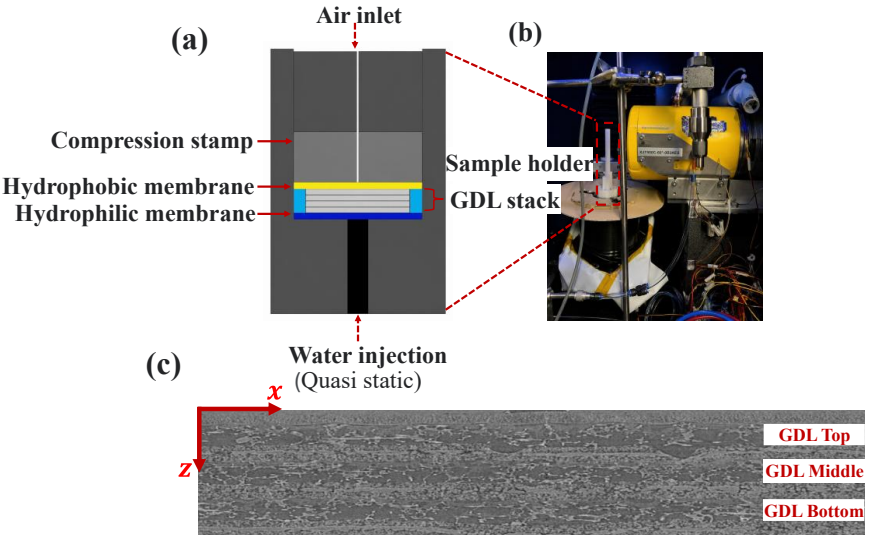

Figure 2.4. Experimental configuration for quasi-static water injection and cross-section grey-scale image of the GDL stack. (a) Schematic of the sample holder showing the GDL stack, compression stamp, hydrophobic and hydrophilic membranes, air inlet, and water-injection direction. (b) Photograph of the experimental setup and sample holder mounted for XTM measurements. (c) Representative reconstructed gray-scale cross-section of the GDL stack, showing the coordinate system and through-plane (z) and in-plane (x,y) directions.

2.4.3 Image reconstruction and phase segmentation

The reconstructed XCT volumes were separated into individual GDL domains and processed in dry and wet states. The dry volumes were filtered and segmented into pore and solid phases and served as reference images for identifying liquid water.

For the partially saturated analysis, each wet volume was rigidly registered to its corresponding dry reference. Since liquid water and the carbon based GDL structure exhibited similar X-ray attenuation, the water phase could not be reliably segmented directly from the wet images. Liquid water was therefore identified from the difference between the registered wet and dry volumes, followed by filtering and segmentation. The resulting water phase was constrained to the corresponding dry pore space for the principal pristine and aged samples. The overall processing workflow is illustrated in Fig. 2.5.

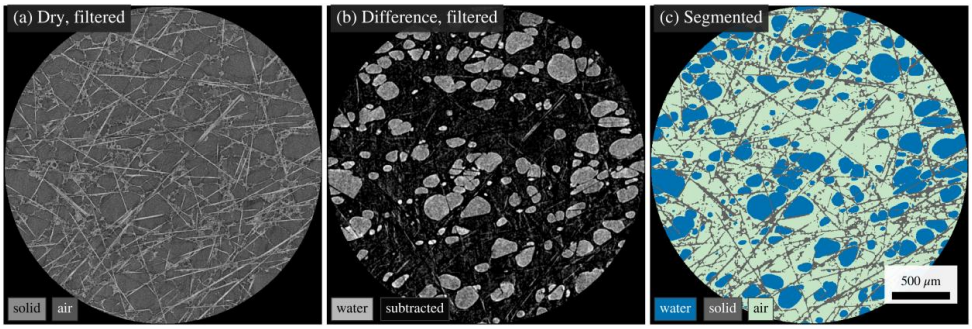

Figure 2.5. Schematic overview of the X-ray XCT image-processing workflow, comprising (a) dry-state GDL segmentation and wet-to-dry registration, (b) difference-image generation, and (c) liquid-water segmentation and connected-component filtering.

2.5 Image-based quantification of pore structure and gas transport

The segmented XCT volumes were used to quantify the pore structure, local water distribution, capillary pressure-saturation curves and saturation dependent diffusivity of the pristine and aged GDL substrates. Three regions corresponding to the upper, middle, and lower samples were analyzed for each material. Porosity was determined from the fraction of pore voxels, while pore-throat-size distributions were obtained from the segmented pore space using a distance-transform and watershed-based analysis. Liquid-water saturation was calculated as:

$$S = N_w / N_p \tag{2.2}$$

Where N_w and N_p are the numbers of water and pore voxels, respectively. Spatial saturation distributions and connected water clusters were additionally evaluated to characterize how water occupied the pore network. Dry and partially saturated effective gas diffusivities were calculated directly from the segmented voxel domains. In the dry state, the connected pore space formed the gas-transport domain, whereas water-filled voxels were excluded under partially saturated conditions. Only gas-phase pathways spanning the investigated transport direction were included. Steady-state diffusion was described by:

$$\nabla \cdot (D_M \nabla c) = 0 \tag{2.3}$$

where D_M is the molecular diffusivity and c is the concentration. For each investigated direction q, a concentration difference was imposed between the two opposing domain faces normal to the transport direction, while the remaining boundaries were treated as a Neumann boundary condition (no-flux). The solid phase and water-filled voxels were treated as impermeable to gas transport. After convergence of the concentration field, the effective diffusivity was obtained from the resulting area-averaged diffusive flux according to:

$$D_q^{\text{eff}} = \frac{\bar{J}_q L_q}{\Delta c} \tag{2.4}$$

where $\bar{J}_q$ is the mean diffusive flux through the domain, L_q is the domain length in direction q, and Δc is the imposed concentration difference. Effective diffusivities were evaluated independently in the two in-plane directions and the through-plane direction. The additional transport loss caused by liquid-water occupation of the pore space was expressed using the relative diffusivity:

$$D_{\mathrm{rel},q} = D_q^{\mathrm{eff}}(S)/D_{\mathrm{eff},q}^{\mathrm{dry}} \tag{2.5}$$

Values below unity therefore represent the reduction in gas-phase transport caused by liquid-water.

2.5.1 Representative Elementary Volume (REV)

The dependence of porosity and tortuosity on domain size was examined to assess whether the analysed volumes were representative of the GDL substrates (Fig. 2.6). The in-plane properties approached convergence as the in-plane dimensions increased. Through-plane tortuosity, however, continued to increase as the analysed thickness increased from 10 to 50 µm, with no clear indication of convergence. The corresponding through-plane effective diffusivities therefore remain dependent on the sampled volume, limiting their interpretation as bulk material properties.

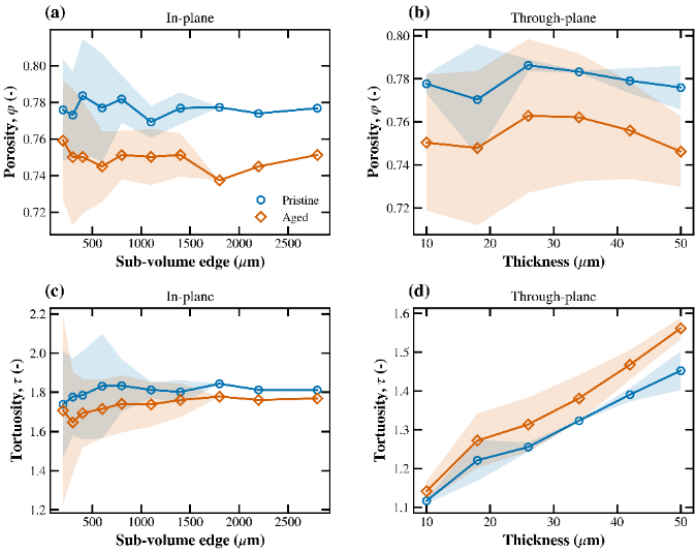

Figure 2.6. Sensitivity of pore-space properties to the size of the analyzed volume for pristine and aged GDL substrates. (a) In-plane porosity as a function of sub-volume edge length, (b) through-plane porosity as a function of analyzed thickness, (c) in-plane tortuosity as a function of subvolume edge length, and (d) through-plane tortuosity as a function of thickness. Shaded regions indicate the variability between sub-volumes.

3. Experimental results

This chapter summarizes the experimental results used to determine how GDL material structure, composition, compression, and ageing influence the properties relevant to PEMFC operation. Emphasis is put on the common trends and material-specific differences that are subsequently used as input to the continuum models, rather than on the complete experimental datasets presented in the appended papers.

3.1 GDL pore structure

As shown in Fig. 3.1, the investigated GDLs exhibited distinct pore-entry-size distributions and accessible pore volumes. GDL-X had the highest cumulative intrusion volume per unit mass, with a pronounced contribution from the macropore range associated with the fibrous substrate. Freudenberg showed a lower intrusion volume and a macropore distribution shifted towards smaller pore sizes, whereas SGL contained an additional population at intermediate pore-entry sizes. Based on the SEM observations, this feature may be associated with porous binder-rich regions and with the heterogeneous structure formed where the MPL penetrates the fibrous substrate, as illustrated in Fig. 1.3. This interpretation remains tentative since MIP provides no spatial information and cannot uniquely assign the measured pore populations to specific structural regions.

These structural differences are relevant to both gas and liquid-water transport because pore dimensions, constrictions, and network connectivity affect gas-phase transport and capillary invasion. The measured pore-entry-size distributions are therefore used later in the thesis to derive material-specific two-phase constitutive relations, including capillary pressure–saturation behaviour and MPL relative permeability. They also provide input for calculating the dry and saturation-dependent effective diffusivity of the MPL, accounting for both molecular and Knudsen contributions to diffusion.

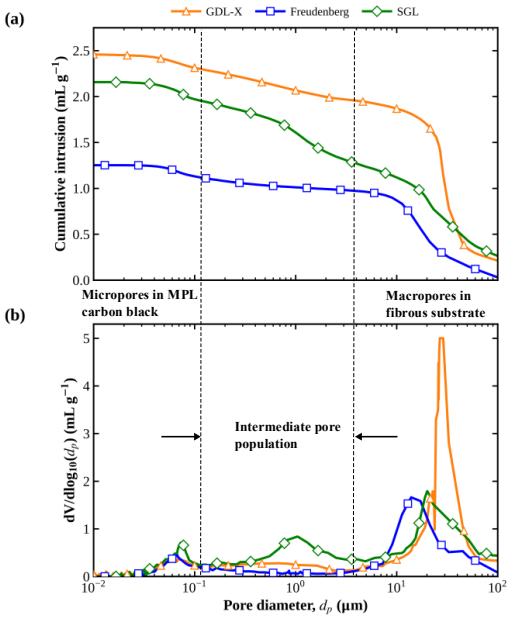

Figure 3.1. (a) Cumulative mercury intrusion volume and (b) differential pore-volume distribution as a function of equivalent pore-entry diameter for GDL-X, Freudenberg, and SGL GDLs. The distributions indicate fine-pore, intermediate, and macropore populations associated predominantly with the MPL, mixed binder/MPL–substrate structures, and fibrous substrate, respectively. The indicated regions represent approximate pore-size regimes and should not be interpreted as uniquely identified physical layer boundaries.

3.2 Mechanical properties

The mechanical properties of the investigated GDLs are summarized in Fig. 3.2. All materials exhibited nonlinear through-plane compression, with increasing resistance to deformation as fiber rearrangement became progressively restricted. At a given stress, GDL-X showed the largest compressive strain, whereas Freudenberg showed the smallest. The comparatively high compression resistance of Freudenberg can be attributed to its three-dimensional hydroentangled nonwoven fiber network, in which fiber entanglements limit through-plane deformation and structural rearrangement. In SGL, compression occurs mainly through bending and rearrangement of the quasi-planar fiber network, while MPL intrusion reduces the space available for fiber motion and influences the progression towards densification. TGP-H-60 showed a similar bending-dominated deformation mechanism, with PTFE at fiber junctions further restricting fiber movement.

The bending and shear measurements produced a different material ranking because these loading modes engage the fiber network in different ways. TGP-H-60 had the highest bending stiffness, consistent with its highly graphitized structure and preferential in-plane fiber orientation. Freudenberg, despite its high resistance to through-plane compression, had a considerably lower bending modulus. Its three-dimensional fiber architecture provides fewer continuous in-plane load-bearing paths, while the lower graphitization temperature used during fiber manufacture may also contribute to the lower fiber stiffness. In contrast to the carbon-paper GDLs, Freudenberg had a higher bending modulus in the CMD than in the MD, reflecting differences in the in-plane fiber-orientation distribution of the nonwoven network. Its three-dimensional architecture also resulted in a weaker directional dependence on shear.

These mechanical characteristics determine how the GDL deforms under the non-uniform mechanical compression imposed by the flow-field structure. The through-plane stress–strain relation governs the local compression and remaining thickness beneath the ribs, whereas bending and shear stiffness influence deformation across the rib–channel transition. Furthermore, deformation of the fiber network affects electrical and thermal transport by changing the number and area of contacts between neighbouring fibers. The mechanical properties therefore provide the basis for interpreting the compression-dependent conductive properties discussed in Section 3.3.

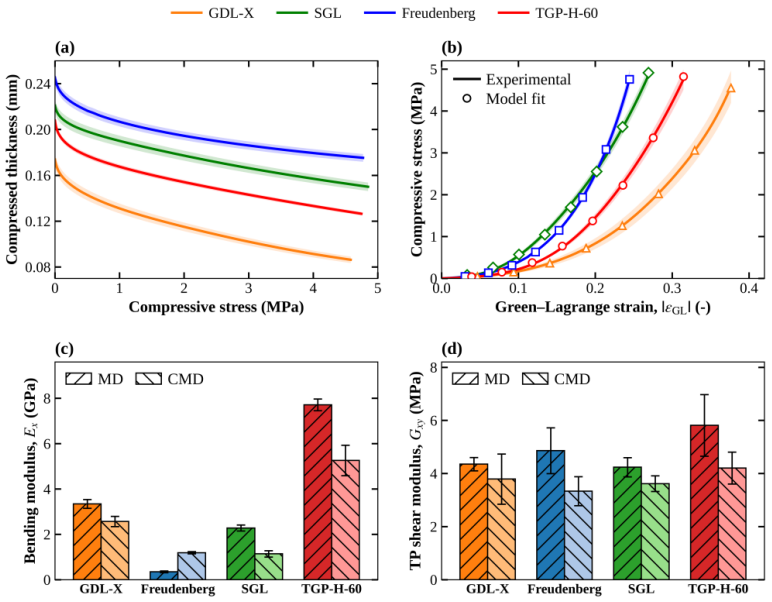

Figure 3.2. Through-plane compression response of the investigated GDLs. (a) Predicted compressed thickness as a function of applied compressive stress. (b) Experimental mean compressive stress–strain response together with the fitted nonlinear constitutive model for each GDL.

3.3 Thermal and electrical properties

The through-plane thermal and electrical conductivities increased with compressive stress for all investigated GDLs (Fig. 3.3). Expressing the conductivities as functions of solid volume fraction reduced some of the separation associated with compression, but distinct material trends remained. Solid fraction alone is therefore insufficient to describe conduction; fiber architecture and the intrinsic properties of the carbon structure also contribute.

TGP-H-60 carbon paper had the highest through-plane thermal conductivity, consistent with its highly graphitized carbon-fiber structure. Freudenberg combined comparatively low thermal conductivity with high electrical conductivity, indicating that thermal and electrical transport are governed by different aspects of the material structure. Its thermal conductivity is consistent with the lower graphitization temperature used during fiber manufacture, whereas the high electrical conductivity points to favourable connectivity within the three-dimensional fiber network. In addition, the carbon powder applied during post-treatment to enhance electrical conduction may provide further conductive pathways within the substrate.

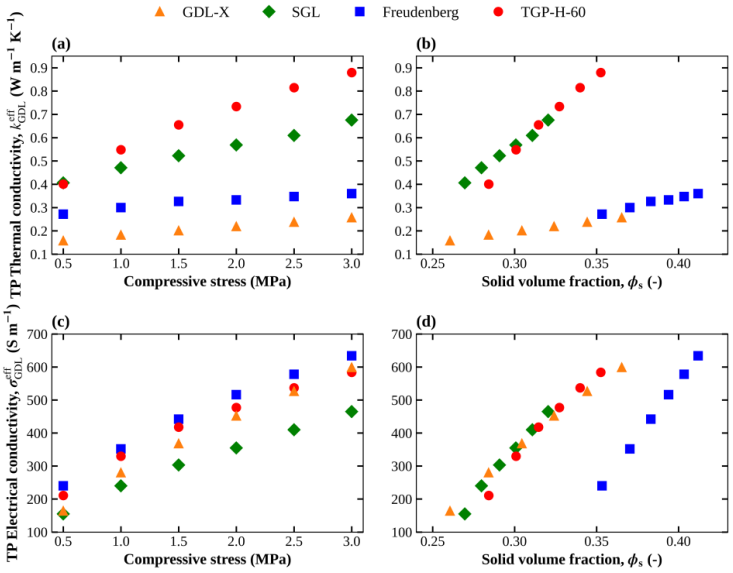

Figure 3.3. Through-plane transport properties of the investigated GDLs as a function of compression and solid volume fraction. (a) Effective thermal conductivity, κ_{tp}^{eff} versus compressive stress; (b) effective thermal conductivity versus solid volume fraction, ϕ_s. (c) effective electrical conductivity, σ_{tp}^{eff} versus compressive stress; and (d) effective electrical conductivity versus solid volume fraction. Symbols denote the different GDL materials as indicated in the legend

The in-plane electrical conductivity was higher in the MD compared to CMD for all materials (Fig. 3.4). TGP-H-60 had the highest values and most pronounced anisotropy, consistent with the preferential in-plane fiber orientation. The analytical model developed in Paper I showed that the voltage drop associated with lateral current conduction beneath the channels increases with channel width and current density, emphasizing the importance of in-plane electrical conductivity for wider channel spans.

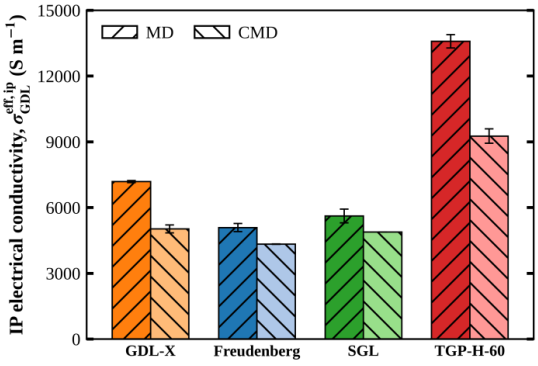

Figure 3.4. In-plane electrical conductivity of the investigated GDLs measured in the machine direction (MD) and cross-machine direction (CMD). The conductivity was consistently higher in the MD than in the CMD, with the strongest directional dependence observed for TGP-H-60. Error bars indicate the experimental variability.

From a performance perspective, high electrical conductivity reduces ohmic losses and facilitates current collection, whereas through-plane thermal conductivity determines heat transport from the MEA towards the flow-field plate. Higher thermal conductivity promotes heat removal and limits temperature gradients, while increased thermal resistance can increase the local MEA temperature and thereby affect evaporation, water distribution, and reactant transport [52]. Furthermore, the compression dependence of the bulk conductive properties links solid-phase transport directly to the mechanical state of the GDL. Compression modifies the inter-fiber contact network while simultaneously reducing pore volume, such that conductive and pore-transport properties must be considered together under the compression conditions present in the assembled fuel cell.

3.4 In-plane gas permeability

Compression caused a pronounced nonlinear decrease in the in-plane gas permeability of all investigated GDLs (Fig. 3.5). TGP-H-60 maintained the highest permeability throughout the investigated pressure range, whereas SGL decreased to the lowest levels at moderate and high compression. GDL-X and Freudenberg remained between these two materials across most of the compression range.

The material-specific trends remained distinct when permeability was expressed as a function of compressed porosity, demonstrating that pore volume alone does not determine resistance to pressure-driven flow. Pore dimensions, constrictions, and connectivity are also important factors. The relatively low permeability of SGL may partly be associated with MPL intrusion into the fibrous substrate (see Fig.1.3), which may constrict larger pores and reduce the connectivity of lateral flow pathways. Freudenberg, by contrast, maintained comparatively high permeability despite its lower porosity, indicating that its three-dimensional pore architecture provides effective pathways for lateral flow. The high permeability of TGP-H-60 at comparable porosity further emphasizes the importance of pore architecture rather than pore volume alone.

In an assembled cell, in-plane permeability determines the resistance to pressure-driven lateral gas flow within the compressed GDL. The influence of in-plane permeability on reactant redistribution depends on the pressure gradients imposed by the flow-field geometry. Where these gradients induce significant convective transport, higher permeability can facilitate gas flow towards regions beneath the ribs. When lateral oxygen supply is predominantly diffusion-controlled, however, transport is governed primarily by the effective in-plane diffusivity and local concentration gradients. Under two-phase conditions, gas-phase mobility is additionally influenced by the saturation-dependent relative permeability introduced in Eq. (1.8). The experimentally determined compression dependence was therefore incorporated into the material-specific constitutive relations describing pressure-driven transport.

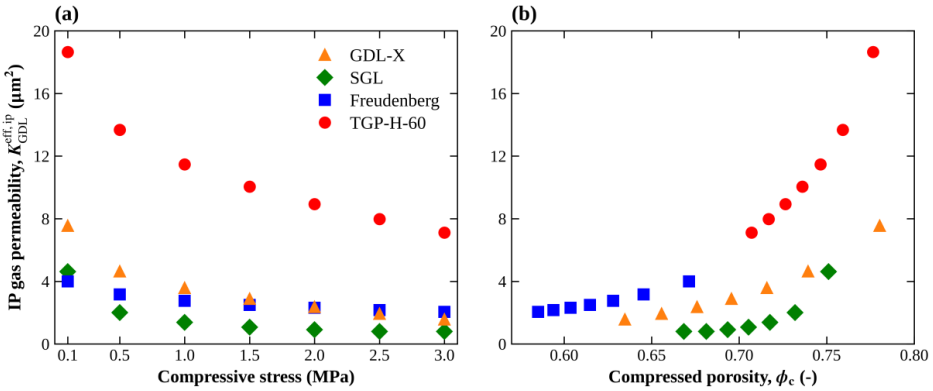

Figure 3.5. In-plane gas permeability, K_{ip}^{eff} as a function of applied compression. (a) IP gas permeability vs compressive stress. (b) IP gas permeability vs compressed porosity.

3.5 GDL microstructure, PTFE distribution, and oxygen transport

The spatial distribution of PTFE depended strongly on the native substrate architecture. Identical-location Raman and SEM–EDX measurements showed contrasting distributions in the binder-free F-H23 and binder-containing SGL-39AA substrates (Fig. 3.6). In F-H23, PTFE was concentrated mainly at fiber intersections and along fiber surfaces, whereas in SGL-39AA it was distributed more extensively over the native carbonaceous binder. The correspondence between the Raman C–F signal and the fluorine maps obtained by EDX supports this distinction. Cross-sectional analysis of F-H23 further showed PTFE agglomerates throughout the substrate thickness, without a systematic increase in PTFE concentration near either surface.

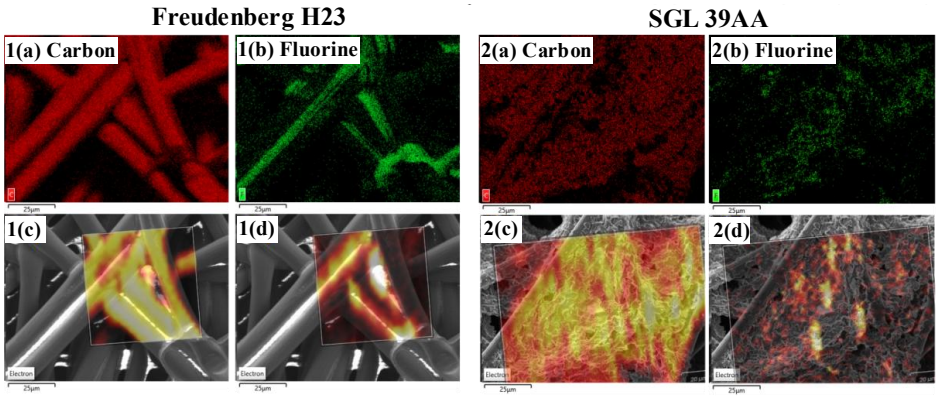

Figure 3.6. Identical-location Raman and SEM–EDX mapping of PTFE-treated F-H23 and SGL-39AA. The measurements show the different spatial distribution of PTFE in the binder-free and binder-containing substrates. Adapted from Paper II.

These observations demonstrate that nominal PTFE loading does not uniquely describe the resulting hydrophobic treatment. The native fiber–binder structure influences where subsequently applied PTFE is deposited and, consequently, how the internal surfaces of the GDL are modified.

The oxygen-transport measurements showed a stronger dependence on substrate type than on PTFE loading (Fig. 3.7). The pressure-dependent oxygen-transport resistance, R_p, was consistently lower for SGL-39AA than for F-H23, whereas increasing the PTFE content from 5 to 20 wt% produced only a modest change within either material. In SGL-39AA, deposition of PTFE on the pre-existing binder may limit the extent to which additional PTFE partially obstruct gas-accessible pathways.

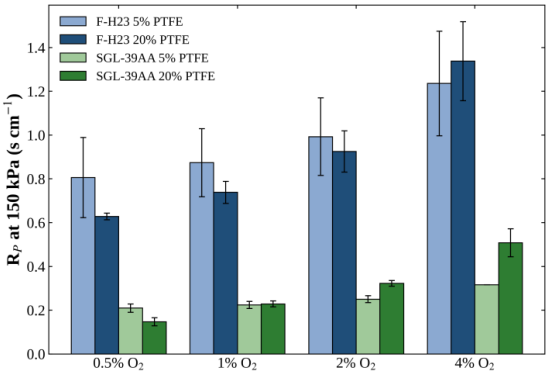

Figure 3.7. Pressure-dependent oxygen transport resistance (DOTR) evaluated at 150 kPa absolute pressure for the four GDL/PTFE combinations, at four O_2 mole fractions (0.5, 1, 2, 4%). DOTR was extracted from a linear regression of R_{tot} vs. absolute pressure using limiting-current sweeps at 1.5, 2, and 3 bar absolute (75 °C, 60% RH, zero-gradient cell, no MPL, constant CCM). Error bars represent ±1 standard error of the regression slope.

Themicroscopy provides a structural explanation for this relatively weak dependence on PTFE loading. In SGL-39AA, much of the PTFE was deposited on the pre-existing binder phase and therefore did not necessarily create an equivalent additional obstruction of the gas-accessible pore network. In F-H23, PTFE was strongly concentrated around fiber intersections, but increased loading nevertheless produced no significant increase in dry oxygen-transport resistance. The difference in R_p between the two substrates cannot be attributed to the binder alone, since the materials also differ in porosity, thickness, and fiber morphology.

Collectively, the results show that PTFE content and PTFE distribution represent distinct material characteristics. Over the range investigated here, the native substrate architecture had a larger influence on oxygen-transport resistance than increasing the nominal PTFE loading from 5 to 20 wt%. Hydrophobic treatment should therefore be considered in relation to the structure into which the PTFE is introduced rather than by nominal loading alone.

3.6 Ageing-induced changes in GDL structure and water transport

The comparison between pristine GDL material and material recovered after 20 khrs stack operation revealed differences in pore structure, wettability, and water retention. These measurements were combined with image-based diffusion calculations to distinguish changes in water saturation at a given capillary pressure from changes in gas transport at a given saturation.

3.6.1 Wettability and Pore Structure

The contrasting evolution of the advancing and receding angles in Fig.3.8 indicates that ageing primarily modifies the receding response. At the anode outlet, the receding angle decreases by approximately 29°, compared with only 4° for the advancing angle, resulting in an increase in contact-

angle hysteresis from 34° for the pristine material to 59° for the aged material. Moreover, the standard deviation of the receding-angle measurements increases from 5.5° to 13.0°. The larger change and increased spatial variability in the receding contact angle could stem from a non-uniform modification of the surface wetting behaviour during ageing. In particular, the reduction in the receding contact angle indicates an increased tendency for liquid water to remain on the surface during receding.

Hereafter, the MEA4 anode outlet material is designated as aged, while the corresponding reference material is designated as pristine.

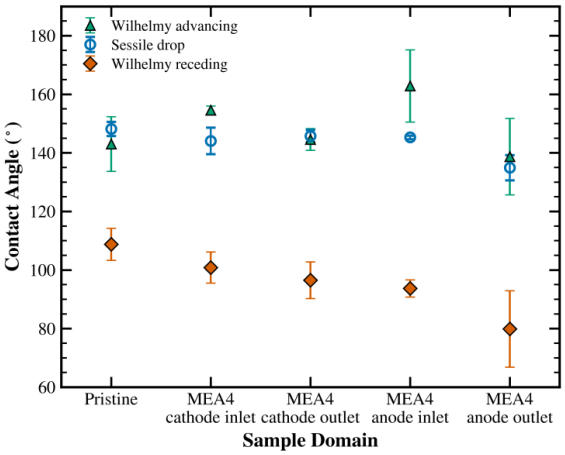

Figure 3.8. External contact angles of the pristine GDL and aged GDL samples recovered from the anode-inlet, anode outlet, cathode inlet, and cathode outlet positions of MEA4. Sessile-drop, advancing, and receding contact angles are shown for each sampling location.

The aged substrate exhibited lower porosity and fewer large pore throats compared to the pristine reference material (Fig. 3.9). These differences should be interpreted in relation to the compression during imaging as shown in Table. 2.2. The aged samples were thinner, and the manually adjusted mounting force introduced uncertainty in the applied compression. The measured pore structures may therefore reflect both irreversible settling during fuel cell stack operation and differences in compression during assembly. Since water invasion was subsequently measured in the same compressed samples, the structural measurements remain directly relevant to the observed capillary pressures.

The structural and wettability measurements imply competing effects on water invasion. If wettability were unchanged, the reduced number of large pore throats would shift invasion towards higher capillary pressures, since $p_{\mathrm{entry}} \propto 1/r_t$. Conversely, a shift towards more wettable conditions would lower the capillary barrier to water invasion and facilitate water retention. The measured capillary pressure–saturation relation therefore reflects the combined influence of the structural and wetting changes.

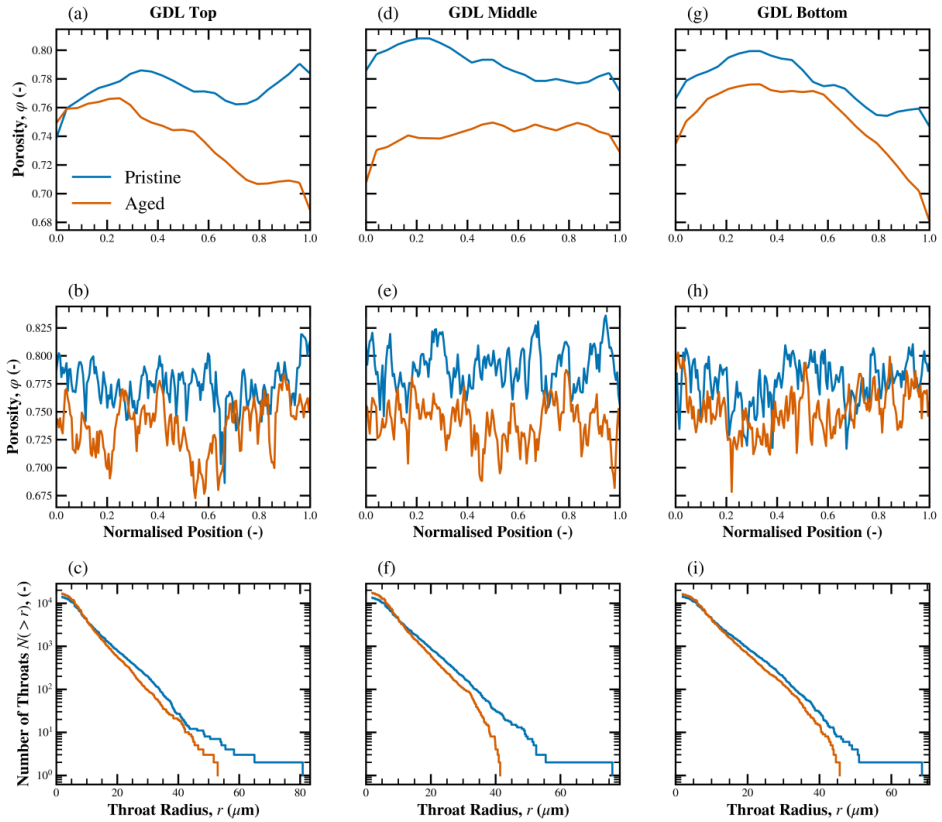

Figure 3.9. Structural characteristics of the pristine and aged substrates calculated on $2.8 \times 2.8 \times 0.05\ mm^3$ dry substrate volume. Through-plane porosity profiles for the top, middle, and bottom GDL samples are shown in (a), (d), and (g), respectively; corresponding in-plane porosity profiles are shown in (b), (e), and (h); and cumulative throat-sizes are shown in (c), (f), and (i).

3.6.2 Capillary pressure and water distribution

At 15 mbar, the aged material reached an average saturation of 0.147, compared with 0.071 for the pristine material. This difference diminished with increasing capillary pressure, and the saturation curves crossed at approximately 20 mbar (Fig. 3.10). Above the crossover pressure, the saturation was higher in the pristine material. Prolonged operation was therefore associated with increased water uptake at low capillary pressure, followed by a reversal at higher pressures.

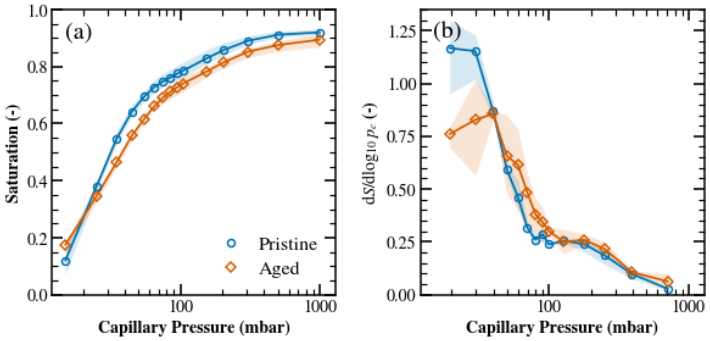

Figure 3.10. (a) Mean liquid-water saturation as a function of capillary pressure for the pristine (blue) and aged (orange) GDL substrates, evaluated within segmented subvolumes measuring 2.8 × 2.8 × 0.05 mm³. (b) Derivative of mean saturation with respect to the base-10 logarithm of capillary pressure. Shaded bands indicate $\pm$ 1 std across the three specimens at the bottom, middle and top of each GDL stack ($n = 3$).

The higher saturation of the aged material at low capillary pressures cannot be explained by the reduction in large pore throats alone. A contribution from altered wettability is consistent with the external contact angle measurements, although these do not directly characterize wetting within the pore network. The segmented images further revealed more small water-filled clusters in the aged material and water near the MPL interface where the pristine substrate remained nearly dry (Fig. 3.11). These observations indicate differences in water invasion and distribution without isolating the respective contributions of wettability and pore structure. Liquid films below the imaging resolution may connect apparently separate clusters, so these should not necessarily be regarded as hydraulically disconnected.

At increased capillary pressures, higher saturation was observed for the pristine material across the analyzed substrate thickness. The crossover therefore indicates that the relative influence of pore structure and wettability changes as water invasion progresses. The measurements establish the combined effect but do not allow their individual contributions to be quantified.

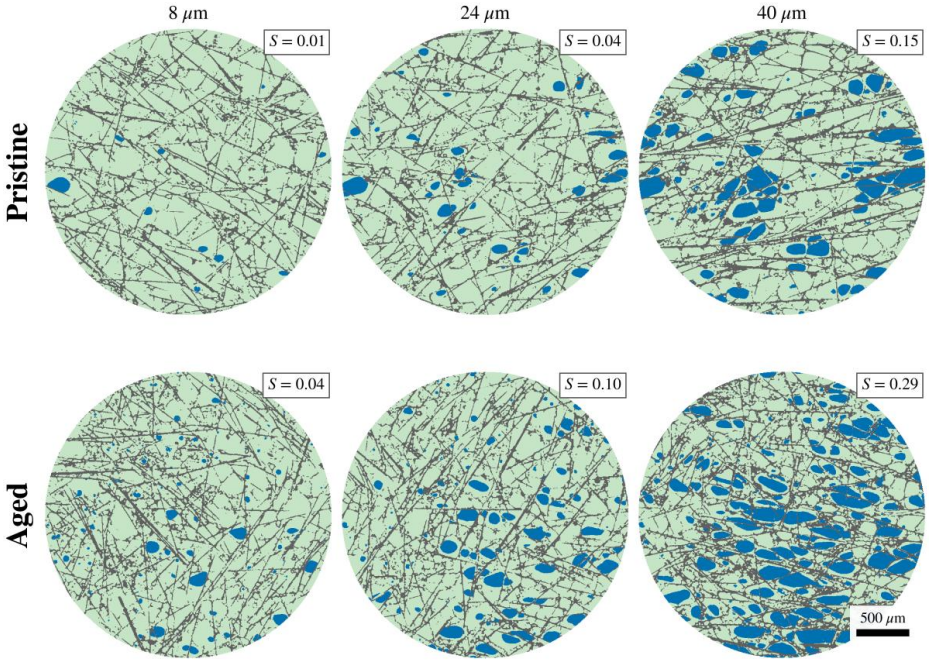

Figure 3.11. Spatial variations in average saturation for the pristine material (upper row) and aged material (bottom row) using $2.8 \times 2.8 \times 0.05\ mm^3$ segmented subvolume for three thicknesses from MPL towards the injection side at 15 mbar injection pressure.

3.6.3 Diffusivity

Dry state in-plane diffusivities were similar for the pristine and aged substrates, whereas the through-plane values showed larger differences. However, the representative volume analysis did not establish convergence in the through-plane direction across the substrate thickness. The apparent differences may therefore arise from local structural heterogeneity and the limited sampling volume and cannot be assigned conclusively to ageing.

To isolate the effect of liquid water, the diffusivity of each partially saturated structure was normalized by its corresponding dry value. Relative diffusivity decreased with increasing saturation as liquid water restricted the gas-filled pathways. At a given saturation, the pristine and aged materials showed similar relative diffusivities, with no systematic separation across the investigated directions (Fig. 3.12). The results therefore provide no clear evidence that ageing changed the relationship between saturation and gas-phase diffusivity.

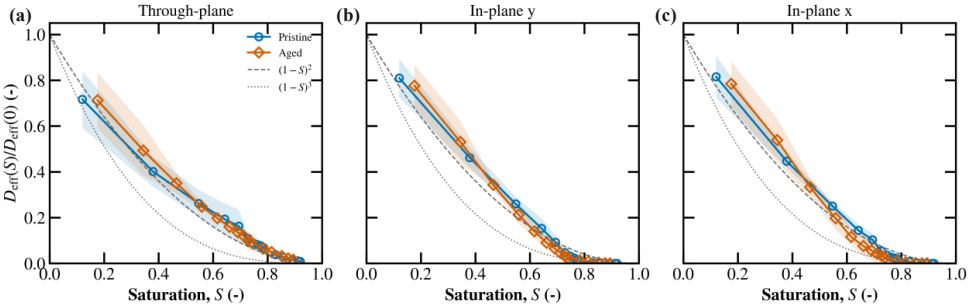

Figure 3.12. Relative effective gas diffusivity of the pristine and aged GDL substrates as a function of water saturation in the (a) through-plane and (b,c) two orthogonal in-plane directions. Values are normalized by the corresponding dry effective diffusivity. Shaded bands indicate $\pm$ 1 std across the three specimens at the bottom, middle and top of each GDL stack ($n = 3$). Reference relations are included for comparison.

The principal observed difference concerned the capillary response. Although the relative diffusivity–saturation relationships were broadly similar, the higher water saturation in the aged material at low capillary pressures resulted in larger fractional reduction in gas diffusivity. Dry transport properties alone therefore do not fully describe the effects of fuel cell stack operation. Their interpretation must also account for the capillary-pressure–saturation relationship, which determines the extent of water invasion and the associated restriction of gas-filled transport pathways under the investigated conditions.

4. Model development

The computational work comprises two related approaches based on a continuum PEMFC model. Paper III investigates the interaction between GDL mechanics, material properties, flow-field geometry, and cell performance using a single-phase formulation and a discrete set of flow-field geometries. Paper IV extends the model to two-phase transport and a parametrically defined geometry within a surrogate-assisted optimization framework for exploration of a larger design space and multiple operating conditions. The two-phase formulation additionally incorporates capillary and saturation-dependent transport relations informed by the pore-structure characterization.

This chapter first presents the common continuum formulation and constitutive relations, followed by the study-specific model implementations and the surrogate-assisted optimization framework.

4.1 Continuum PEMFC model

The model was formulated on a two-dimensional cross-section of a repeating rib–channel unit, as illustrated in Fig. 4.1. The in-plane direction resolves the rib–channel structure, while the through-plane direction extends across the membrane-electrode assembly. Variations along the channel direction are therefore not resolved explicitly.

The domain comprises the GDL, MPL, CL, and PEM. Mechanical compression is applied at the flow-field ribs, producing spatially varying deformation and contact pressure over the ribs and channel. The fields are coupled to the transport model through compression-dependent material constitutive relations and GDL–flow-field-plate electrical contact resistance.

The same domain architecture is used in Papers III and IV. Paper III considers a discrete set of rib–channel geometries, whereas Paper IV parameterizes the geometry in Fig.4.1 and selected GDL properties for design exploration within the optimization framework.

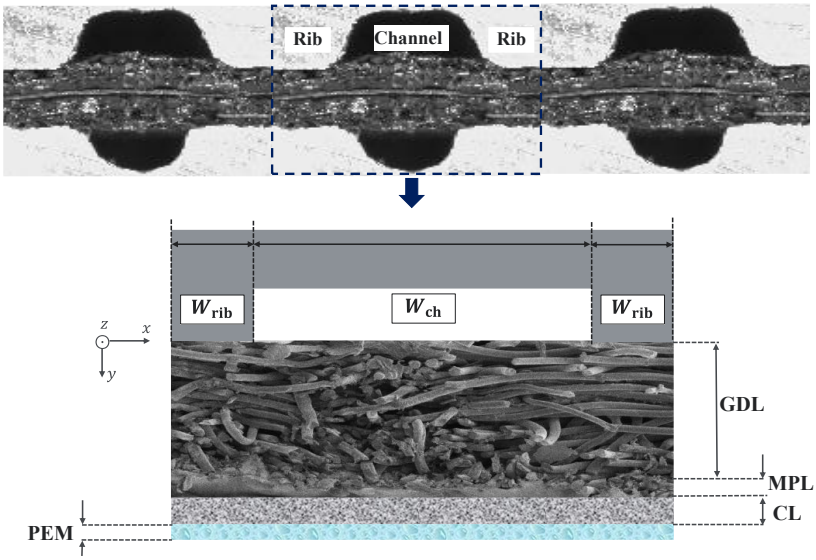

Figure 4.1. Physical rib–channel structure and corresponding two-dimensional computational domain. The dashed region indicates the repeating unit. The cathode half-cell is shown schematically, comprising the GDL, MPL, catalyst layer, and half of the polymer electrolyte membrane. W_{rib} and W_{ch} denote the rib and channel widths, respectively.

4.1.1 Model assumptions

The continuum model retains the principal transport, electrochemical, thermal, and mechanical processes while adopting the following assumptions:

1. The cell is represented by a two-dimensional, steady-state, non-isothermal formulation in the through-plane and rib–channel directions; variations and reactant depletion along the channel direction are not resolved.
2. The domains are treated as homogeneous effective continua, with electrochemical reactions represented by volumetric source terms within the catalyst layers.
3. The GDL is represented as an orthotropic material under finite-deformation plane-strain conditions, with deformation resolved in the through-plane and rib–channel directions and zero strain assumed in the out-of-plane channel direction. The solid-phase volume is assumed to remain constant during compression, such that changes in GDL volume are attributed to changes in pore volume.
4. Hydrogen crossover through the membrane and the associated parasitic currents are neglected.
5. Paper III employs a single-phase formulation, whereas Paper IV includes gas–liquid two-phase transport. In the latter, liquid water is treated as the non-wetting phase in the hydrophobic GDL and MPL. The MIP-derived capillary-pressure–saturation relations represent the primary drainage curve in the hydrophobic regime; the negative-capillary-pressure region associated with hydrophilic pores is not included. Hysteresis is neglected.

4.1.2 Governing equations

The continuum formulation couples mechanical equilibrium with conservation of mass, species, electronic and protonic charge, dissolved water, and energy. Paper III employs a single-phase description of gas transport, charge transport, dissolved-water transport, and heat transfer, whereas Paper IV extends the formulation to include liquid-water transport in the porous GDL, MPL, and catalyst layers. The governing equations are summarized in Table 4.1.

Table 4.1. Governing equations used to solve the respective field variables

Physical process	Governing equation	Application
Mechanical equilibrium	$\nabla \cdot \boldsymbol{\sigma} = \mathbf{0}$	Stress and deformation of the GDL
Mass conservation	$\nabla \cdot (\rho_\alpha \mathbf{u}_\alpha) = S_{\mathrm{m},\alpha}$, $\mathbf{u}_\alpha = -\dfrac{\mathbf{K}\boldsymbol{k}_{r\alpha}\nabla p_\alpha}{\mu_\alpha}, \alpha \in \{\mathrm{g},\mathrm{l}\}$	Phase flow in the porous domains
Species conservation	$\nabla \cdot \left(\rho_\mathrm{g} Y_i \mathbf{u}_\mathrm{g} + \mathbf{J}_i\right) = S_i$	Reactant and water vapour transport
Electronic charge conservation	$\nabla \cdot \mathbf{J}_{\mathrm{e}^-} = S_{\mathrm{e}^-}, \mathbf{J}_{\mathrm{e}^-} = -\boldsymbol{\sigma}_\mathrm{s}^\mathrm{eff}\nabla\varphi_{e^-}$	Electronic current in the flow-field plates and conducting porous domains
Ionic charge conservation	$\nabla \cdot \mathbf{J}_{\mathrm{H}^+} = S_{\mathrm{H}^+}, \mathbf{J}_{\mathrm{H}^+} = -\boldsymbol{\sigma}_\mathrm{p}^\mathrm{eff}\nabla\varphi_{\mathrm{H}^+}$	Protonic current in the membrane and CL ionomer
Dissolved water conservation	$\nabla \cdot \mathbf{N}_\lambda = S_\lambda$, $\mathbf{N}_\lambda = -c_\mathrm{f}\boldsymbol{D}_\lambda^\mathrm{eff}\nabla\lambda + \left(\dfrac{n_\mathrm{d}}{\mathcal{F}}\right)\mathbf{J}_{\mathrm{H}^+} - \left(\boldsymbol{D}_{\lambda\mathrm{T}}^\mathrm{eff}/M_w\right)\nabla T$	Water transport within the ionomer
Energy conservation	$\nabla \cdot \mathbf{N}_E = S_\mathrm{T}$, $\mathbf{N}_E = \rho_\mathrm{g}\mathbf{u}_\mathrm{g}\left(h_\mathrm{g} + \dfrac{\left\|\mathbf{u}_\mathrm{g}\right\|^2}{2}\right) - \boldsymbol{\kappa}^\mathrm{eff}\nabla T$	Energy transport throughout the computational domain
Anode reaction kinetics	$j_{v,a} = a_{\mathrm{Pt},a} j_\mathrm{HOR}^\mathrm{THV}$	Hydrogen oxidation in the anode catalyst layer
Cathode kinetics and agglomerate transport	$j_{v,c} = a_{\mathrm{Pt},c}\mathcal{E}_\mathrm{agg} j_\mathrm{ORR}$	Oxygen reduction accounting for agglomerate transport limitations

Hydrogen oxidation in the anode catalyst layer was described using the Tafel–Heyrovsky–Volmer formulation [111] . The cathodic reaction rate was calculated using the agglomerate model of Moore et al.[112], which couples intrinsic reaction kinetics with agglomerate scale transport. The resulting volumetric reaction current densities define the electrochemical source terms in the species and charge conservation equations.

The conservation equations are coupled through source terms representing electrochemical reactions, phase change, and heat generation. Gas flow through the porous domains follows Darcy's law, with

relative permeability accounting for liquid-water saturation in the two-phase formulation. Species transport comprises convection and multicomponent diffusion, with effective diffusivities accounting for pore structure, liquid-water saturation, and, where applicable, Knudsen effects. Electronic and protonic currents are coupled through the catalyst-layer reactions, while dissolved-water transport in the ionomer phase comprises water diffusion, electro-osmotic drag, and thermal-osmotic transport. The energy balance accounts for conduction and convection, together with heat sources associated with electrochemical reactions, ohmic losses, sorption/adsorption, and phase change (condensation/evaporation).

4.2 Constitutive models

The governing equations require constitutive relations linking local material properties to the mechanical and saturation state of the GDL. Compression-dependent properties are evaluated from the local deformation and contact pressure, while the two-phase formulation additionally includes saturation-dependent capillary and transport relations. Compression-induced changes in the substrate capillary-pressure saturation relationship are represented by scaling the van Genuchten parameter α according to the local void ratio. This shifts the capillary-pressure scale without altering the shape of the retention curve, while the remaining van Genuchten parameters and the MPL capillary properties are assumed to remain unchanged.

4.2.1 Mechanical Constitutive Law

The GDL mechanical response was described using an orthotropic finite-deformation formulation under plane-strain conditions. Finite deformation was required because of the large through-plane compression experienced by the GDL, while orthotropy accounts for the distinct mechanical responses in the through-plane and in-plane directions, respectively.

The nonlinear through-plane response was represented using a constitutive relation developed from the experimental stress-strain data presented in Paper I. The independently determined in-plane elastic and through-plane shear moduli were incorporated to define the orthotropic or transversely isotropic mechanical properties. The full strain-energy formulation and parameter identification are provided in Paper I.

The local deformation is described by the deformation gradient, **F**, from which the local volume ratio is obtained as:

$$\mathcal{J} = \det \mathbf{F} \tag{4.1}$$

Here, $\mathcal{J} = 1$ denotes unchanged volume, whereas $\mathcal{J} < 1$ indicates local volume reduction. Assuming conservation of the solid volume, the local porosity is then related to the initial porosity, ϕ_0 :

$$\phi_c = 1 - \frac{(1 - \phi_0)}{\mathcal{J}} \tag{4.2}$$

The resulting porosity field and local contact pressure provide the principal coupling between the mechanical solution and the compression-dependent transport and interfacial properties described below.

4.2.2 Compression-dependent transport properties

The local compressed porosity obtained from the mechanical solution was used to update the GDL transport properties. Thermal and electrical conductivities were represented by percolation-type relations fitted to the experimental data, while dry gas diffusivity and permeability were evaluated

from porosity-dependent correlations. The principal relations and their experimental or empirical basis are summarized in Table 4.2.

Table 4.2. Principal compression dependent GDL properties.

Property	Relation	Basis
Through-plane effective thermal conductivity	$\kappa_{\mathrm{tp}}^{\mathrm{eff}} = A_{\kappa}\left(\phi_s - \phi_{\kappa,\mathrm{crit}}\right)^{b_{\kappa}}$	Percolation-type fit to measured thermal conductivity data [106]
Effective electrical conductivity	$\boldsymbol{\sigma}^{\mathrm{eff}} = A_{\sigma}\left(\phi_s - \phi_{\sigma,\mathrm{crit}}\right)^{b_{\sigma}}$	Percolation-type fit to measured electrical conductivity data [106]
Dry effective gas diffusivity	$\boldsymbol{D}_{\mathrm{dry},q}^{\mathrm{eff}} = \dfrac{\phi_c}{\tau_q(\phi_c)} D_M$	Percolation type empirical correlation for anisotropic tortuosity [113]
In-plane effective permeability	$K_{\mathrm{ip}}^{\mathrm{eff}} = A_K \exp(B_K \phi_c)$	Measured in-plane gas permeability data fitted with an exponential function [106]
Through-plane gas permeability	$K_{\mathrm{tp}}^{\mathrm{eff}} = \dfrac{d_f^2 \phi_c^3}{16 k_{\mathrm{CK}} (1-\phi_c)^2}$	Carman-Kozeny empirical correlation [114]

The fitted parameters and complete transport correlations used in the simulations are provided in Papers I, III, and IV.

The conductivity relations include material-specific prefactors, exponents, and percolation thresholds obtained from the measurements in Paper I . Anisotropic gas diffusivity was not measured directly but was estimated using an empirical correlation developed for random fibrous media [113]. In-plane permeability is based on the experimentally measured compression dependence, whereas through-plane permeability is estimated from [114].

4.2.3 Electrical contact resistance

Electrical current is transferred between the GDL and flow-field plate through discrete fiber–plate contacts beneath the ribs. The real conducting area is considerably smaller than the nominal contact area, resulting in localized current constriction. Increasing contact pressure increases both the number of conducting contacts and their individual contact areas, thereby reducing interfacial electrical resistance.

A mechanistic contact model was developed by combining statistical fiber-contact mechanics with experimentally determined compressed GDL thickness and directional electrical conductivities. The model accounts for changes in the real conducting area and the electrical resistivity of the compressed fiber network. Electrically inactive surface regions associated with PTFE and binder were represented through an effective masking parameter. For implementation in the continuum PEMFC model, the pressure dependence predicted by the mechanistic contact model was approximated by the following constitutive relation:

$$R_c(p_{\mathrm{cont}}) = A_c \left(\frac{p_{\mathrm{cont}}+P_s}{P_{\mathrm{ref}}}\right)^{-m_c} \left(1+\frac{p_{\mathrm{cont}}}{P_{\mathrm{ref}}}\right)^{-q_c} \tag{4.3}$$

where $P_{\mathrm{ref}} = 1$ MPa, while A_c, P_s, m_c, and q_c are fitting parameters. The model predicts a nonlinear decrease in electrical contact resistance with increasing pressure (Fig. 4.2). At low pressures, the formation of additional conducting contacts and increases in their contact areas reduce current constriction, resulting in a steep initial decrease in resistance. As contact pressure increases, additional compression produces progressively smaller reductions in contact resistance, accounting for the

gradual flattening of the curves. Among the investigated materials, SGL is predicted to exhibit the highest contact resistance, although the differences relative to Freudenberg and GDL-X diminish at higher contact pressures.

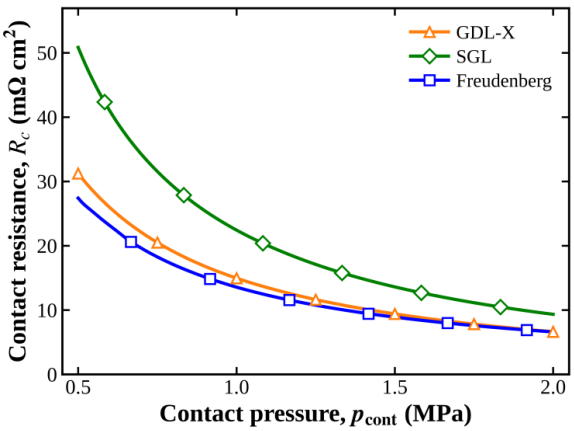

Figure 4.2. Predicted electrical contact resistance as a function of contact pressure.

Since electrical contact with the flow-field plate is restricted to the rib-covered regions, the area-specific contact resistance was normalized to the total geometric cell area using the ratio of flow-field pitch to rib width:

$$\mathrm{ICR} = \bar{R}_c(p_{\mathrm{cont}})\,\frac{W_{\mathrm{rib}}+W_{\mathrm{ch}}}{W_{\mathrm{rib}}} \tag{4.4}$$

Where $\bar{R}_c$ denotes the averaged contact resistance along the rib-covered GDL-FFP interface. In the PEMFC model, the local contact resistance was evaluated from the normal contact pressure obtained from the mechanical solution. The contact pressure was calculated from the average of the Cauchy stress tensors on either side of the GDL–FFP interface, projected onto the interface normal. The resulting spatially varying resistance was incorporated directly into the electrical boundary condition:

$$\varphi_s^{\mathrm{GDL}} - \varphi_s^{\mathrm{FFP}} = j_n R_c(p_{\mathrm{cont}}(\mathbf{x})) \tag{4.5}$$

The resulting interfacial contact resistance was subsequently included as an objective in the surrogate-assisted multi-objective optimization.

4.2.4 MIP-informed constitutive models

Mercury intrusion porosimetry (MIP) was used to derive capillary pressure–saturation relations and saturation-dependent transport properties for the two-phase PEMFC model. The measured pore-entry distributions were separated into populations associated with the fibrous substrate and microporous layer (MPL), providing the basis for the corresponding constitutive relations.

For the SGL material, an intermediate pore population was identified between the larger substrate pores and the finer MPL pores. Cross-sectional SEM observations revealed extensive MPL penetration into the fibrous substrate, suggesting that the intermediate population may partly originate from residual voids and constricted pore entrances within the mixed fiber–MPL region. However, contributions from native binder and other structural features cannot be excluded. Because MIP does not provide spatial information on pore location, the measurements cannot establish whether the MPL itself exhibits a bimodal pore-size distribution. For the constitutive model, the intermediate population

was assigned to the MPL-associated pore space, resulting in an effective bimodal representation. This assignment corresponds to an MPL-associated pore-volume fraction of 0.42, compared with 0.14 if the intermediate population were assigned to the substrate.

The invasion pressures were converted to equivalent water–air capillary pressures by applying the Washburn relation to both fluid systems at the same pore diameter [115]:

$$p_{c,w-a} = p_{c,\mathrm{Hg}} \frac{\xi_w \cos|\theta_w|}{\xi_{\mathrm{Hg}} \cos|\theta_{\mathrm{Hg}}|} \tag{4.6}$$

where ξ denotes surface tension and θ the contact angle, respectively. The conversion changes the pressure scale associated with pore invasion but does not account for water-specific hysteresis, trapping, or disconnected liquid clusters. The broad substrate pore populations were represented using van Genuchten relations [116], whereas Kosugi-type lognormal relations were adopted for the MPL [117]. Where two pore populations were assigned to the same layer, their contributions were combined according to their respective pore-volume fractions. The resulting capillary pressure–saturation relations are shown in Fig. 4.3(a). In the coupled simulations, compression-induced changes in the substrate capillary response were represented by scaling the van Genuchten parameter α according to the local void ratio, $\mathcal{J}$, relative to its uncompressed value. The remaining van Genuchten parameters and the MPL capillary relations were held constant, such that compression altered the capillary-pressure scale without changing the shape of the retention curve.

The MPL gas- and liquid-phase relative permeabilities were derived from the corresponding MIP-informed capillary relations using a Mualem formulation [118] . For bimodal pore distributions, the contributions of the individual populations were combined through pore-volume-weighted integration [119]. For the fibrous substrate, isotropic cubic relations were prescribed for the gas and liquid phases [87] ; $k_{r,g}^{\mathrm{sub}} = (1-S)^3, k_{r,w} = S^3$.The resulting relationships are shown in Fig.4.3(b).

The dry effective diffusivity of the MPL was derived from the MIP-derived pore-size distribution:

$$D_{\mathrm{eff,dry}}^{\mathrm{MPL}} = \phi_{\mathrm{MPL}}^{1.5} \langle D_B \rangle \tag{4.7}$$

Where ϕ_{MPL} denotes the MPL porosity and $\langle D_B \rangle$ is the pore-volume-weighted Bosanquet diffusivity evaluated over the MPL pore population, accounting for both molecular and Knudsen diffusion. For SGL, the intermediate pore population was included in this calculation following its assignment to the MPL-associated pore space.

At finite water saturation, the relative diffusivity was evaluated from the fraction of the pore space remaining gas filled together with the Bosanquet-weighted contribution of the gas-accessible pores:

$$D_{\mathrm{rel}}^{\mathrm{MPL}}(S) = \frac{D_{\mathrm{eff}}^{\mathrm{MPL}}(S)}{D_{\mathrm{eff,dry}}^{\mathrm{MPL}}} \tag{4.8}$$

The saturation dependence therefore reflects both the reduction in gas-filled pore volume and the pore sizes remaining available for gas transport as liquid invasion progresses. For the fibrous substrate, a cubic relation was prescribed.

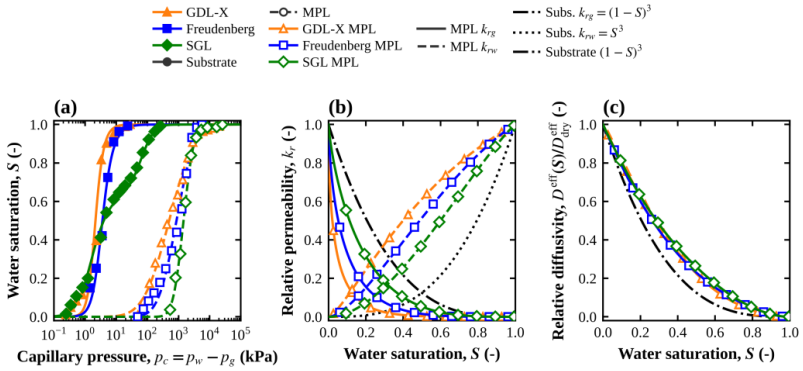

Figure 4.3. MIP-informed two-phase constitutive relations for GDL-X, Freudenberg, and SGL: (a) capillary pressure–saturation, (b) relative permeability, and (c) relative gas diffusivity. Black curves denote the prescribed substrate transport relations.

The derived capillary relations showed reasonable agreement with independent data for comparable GDL materials. Direct water–air measurements report the onset of water invasion at approximately 1 kPa for Toray TGP-H-090 and 2 kPa for SGL 10BA [67] , consistent with the low-kPa pressure range predicted here. Moreover, the van Genuchten exponent obtained for GDL-X ($n = 3.73$) closely agrees with the value ($n = 3.65$) reported for Toray TGP-H-090, while the higher MPL capillary pressures are consistent with its smaller characteristic pore-sizes [120]. These comparisons support the characteristic pressure scale and shape of the MIP-derived relations, although exact agreement is not expected between different GDL grades. MIP further characterizes non-wetting intrusion and therefore cannot distinguish hydrophilic pore regions or the negative water–air capillary pressures associated with pore filling.

4.3 GDL Flow-field Interaction

Paper III used the continuum framework introduced in Section 4.1 to investigate how GDL mechanical properties and compression interact with flow-field geometry. Four discrete cathode rib–channel configurations were considered within the repeating two-dimensional domain.

4.3.1 Flow-field configurations and parametric study

The flow-field configurations were defined by the channel-to-rib width ratio:

$$\lambda = \frac{W_{\mathrm{ch}}}{W_{\mathrm{rib}}} \tag{4.9}$$

where W_{ch} and W_{rib}denote the channel and rib widths, respectively. The total pitch was fixed at 2 mm, such that varying λ redistributed the available width between the channel and rib regions. The investigated configurations are shown in Fig. 4.4.

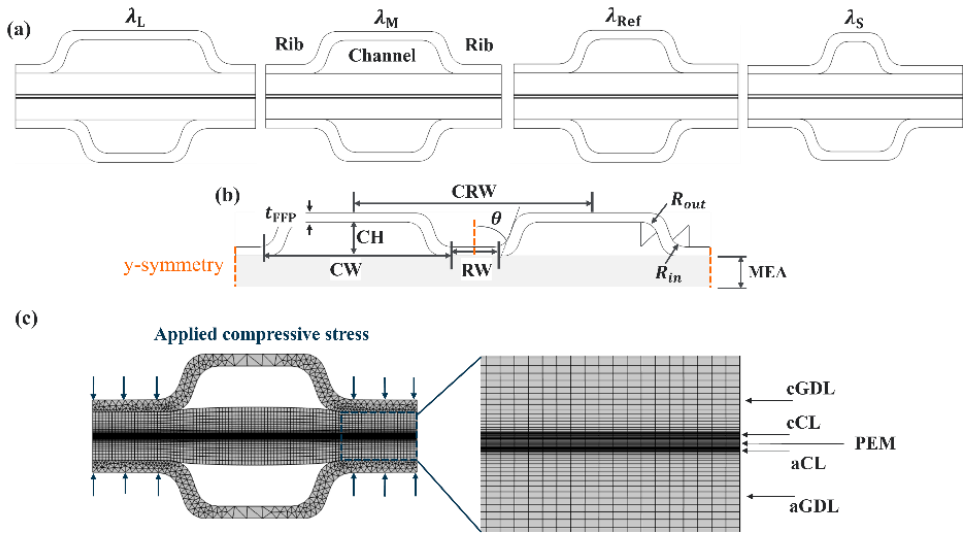

Figure 4.4. Cathode flow-field configurations investigated in Paper III, showing the variation in rib and channel widths and the corresponding channel-to-rib ratio.

In addition to flow-field geometry, the through-plane and in-plane elastic moduli, through-plane shear modulus, and applied compressive stress were varied systematically. The mechanical properties were scaled relative to the experimentally characterized reference GDL, with the subscript 0 denoting the measured baseline value of each property. The investigated parameter ranges are summarized in Table 4.3.

Table 4.3 Flow-field geometries and parameter ranges investigated in Paper III.

Parameter	Symbol	Investigated values / range
Channel-to-rib ratio	λ	0.50, 1.00, 1.50, 2.39
Cell pitch	CRW	2.00 mm
Through-plane elastic modulus	E_y	0.5–2 $E_{y,0}$
In-plane elastic modulus	E_x	0.5–2 $E_{x,0}$
Through-plane shear modulus	G_{xy}	0.5–5 $G_{xy,0}$
Applied compression	F_y	0.5, 1.0, 2.0 MPa

Two complementary parametric studies were performed. Selected parameter combinations were first examined to evaluate local mechanical and electrochemical responses. A Box–Behnken response-surface design was subsequently employed to quantify the main and interaction effects of GDL mechanical properties and compression on cell performance across the investigated flow-field configurations. Further details of the statistical methodology are provided in Paper III.

4.4 Surrogate-assisted optimization framework

A surrogate-assisted framework was developed to investigate trade-offs between mean current density, spatial current-density uniformity, and interfacial contact resistance across the GDL and flow-field design space. Gaussian-process ($\mathcal{GP}$) models were trained using continuum PEMFC simulations and employed as computationally inexpensive approximations of the model responses. Multi-objective Bayesian optimization (MOBO) was subsequently performed using the trained surrogates, with selected non-dominated designs verified through additional continuum simulations.

The framework was also used to investigate whether favourable designs identified at a reference operating condition could be reused under changes in oxygen concentration, temperature, relative humidity, and cell voltage, thereby reducing the computational effort required for subsequent design studies.

4.4.1 Design space, objectives, and simulation database

The design variables comprised cathode GDL thickness, flow-field rib width, and four dimensionless multipliers applied to the baseline through-plane thermal and electrical conductivities and directional gas-phase tortuosities:

$$\mathbf{x} = \left[t_{\mathrm{GDL}}, m_{\kappa}, m_{\sigma}, m_{\tau_{\mathrm{ip}}}, m_{\tau_{\mathrm{tp}}}, W_{\mathrm{rib}}\right]^{\mathrm{T}} \tag{4.10}$$

The multipliers modified the magnitude of the baseline transport relations while preserving their dependence on compression and porosity. The investigated design space covered GDL thicknesses of 0.12–0.30 mm and rib widths of 0.5–1.3 mm. Conductivity multipliers ranged from 0.5 to 3, while tortuosity multipliers ranged from 1 to 3. These independently varied properties represent a virtual material design space and do not necessarily correspond to realizable GDL compositions.

The principal optimization considered three competing objectives: maximizing mean cell current density while minimizing current-density non-uniformity and interfacial contact resistance (ICR). A complementary study varied only GDL thickness and rib width, with the transport-property multipliers fixed at unity, to examine the geometric trade-off between current density and uniformity.

At the reference operating condition, 220 designs were generated using Latin-hypercube sampling. The same designs were evaluated at both oxygen-depletion conditions, while smaller subsets were used for the remaining operating states. In total, the simulation database comprised 899 evaluations across eight operating conditions, as summarized in Table 4.4.

Table 4.4. Operating conditions and number of evaluated designs per condition.

Operating state	x_{O_2}	T / °C	RH / %	V_{cell} / V	Evaluated designs
Reference	0.21	80	80	0.5	220
Mild oxygen depletion	0.14	80	80	0.5	220
Severe oxygen depletion	0.05	80	80	0.5	220
Lower temperature	0.21	70	80	0.5	70
Higher temperature	0.21	90	80	0.5	28

Operating state	x_{O_2}	T / °C	RH / %	V_{cell} / V	Evaluated designs
Lower humidity	0.21	80	60	0.5	70
Combined RH/T shift	0.21	70	100	0.5	40
Lower cell voltage	0.21	80	80	0.2	31

4.4.2 Surrogate-assisted multi-objective optimization

Gaussian-process ($\mathcal{GP}$) surrogate models were trained on the continuum model database to approximate the simulated responses. For each response m:

$$\tilde{y}_m(\mathbf{z}) \sim \mathcal{GP}[\mu_m(\mathbf{z}), k_m(\mathbf{z}, \mathbf{z}'; \boldsymbol{\theta}_m)] \tag{4.11}$$

where $\mathbf{z}$ denotes the normalized surrogate input vector, μ_m and k_m are the mean and covariance functions, and $\boldsymbol{\theta}_m$ contains the hyperparameters governing the characteristic variation and correlation structure of the response.

The surrogate inputs were augmented with physically motivated descriptors combining geometry and effective transport properties:

$$d_{tp} = \frac{t_{GDL}\tau_{tp}}{\bar{\phi}_c x_{O_2}}, \Pi_{rib} = \frac{W_{rib}^2 \tau_{ip}}{\bar{\phi}_c^{rib} t_{GDL}}, \Pi_{geo} = \frac{W_{rib}}{t_{GDL}}\sqrt{\frac{\tau_{ip}}{\tau_{tp}}}, R_{tp} = \frac{t_{GDL}}{\sigma_{tp}^{eff}} \tag{4.12}$$

These quantities represent through-plane oxygen transport, lateral transport beneath the rib, the relative in-plane and through-plane transport scales, and through-plane electrical resistance, respectively. As derived quantities, they provide physically interpretable coordinates without introducing additional design variables.

The $\mathcal{GP}$ surrogates were coupled to multi-objective Bayesian optimization using the qLogNEHVI acquisition function [121] to identify non-dominated designs balancing mean current density, current-density uniformity, and interfacial contact resistance. The previously trained surrogate supplied the predicted objective values, while separate acquisition GP models were updated after each optimization batch. qLogNEHVI selected candidate designs by maximizing the expected improvement in dominated hypervolume, accounting for predictive uncertainty to balance exploration of uncertain regions against exploitation of promising designs. The six-variable and geometry-only studies were initialized with 40 and 24 designs, respectively, followed by batches of four candidates. No additional continuum simulations were performed within the optimization loop; selected non-dominated solutions were subsequently recalculated using the continuum model. Further methodological details are provided in Paper IV.

4.4.3 Transfer between operating conditions

The transfer analysis examined whether design information obtained at the reference operating condition remained applicable following changes in oxygen concentration, temperature, relative humidity, or cell voltage. For each positive, condition dependent response, the relationship between reference and target states was expressed in logarithmic form:

$$\log y_{m,\mathrm{tar}}(\mathbf{x}) = a_m + b_m \log y_{m,\mathrm{ref}}(\mathbf{x}) + \delta_m(\mathbf{x}) \tag{4.13}$$

Where ref and tar denote the reference and target conditions. The coefficients $a_m$and b_m describe the common shift and scaling of the response, while $\delta_m(\mathbf{x})$ represents a design-dependent discrepancy modelled using a $\mathcal{GP}$ conditioned on a limited number of paired reference-target simulations.

Transferability was assessed in terms of absolute prediction accuracy, preservation of design ranking, and multi-objective performance. The latter was quantified through retained hypervolume, comparing the target-condition hypervolume of the reference-condition non-dominated subset with that of the full paired design population. Using a limited number of paired simulations, a model-based lower estimate of retained hypervolume was obtained to assess whether the reference-condition selection could be reused without completing the full target-condition design study. Further details are provided in Paper IV.

5. Model Results

5.1 Coupled influence of GDL mechanics and flow-field geometry on cell performance

Paper III investigated how the orthotropic mechanical properties of the GDL interact with rib–channel geometry and compression to influence PEMFC performance. Among the investigated properties, the through-plane elastic modulus had the largest influence on cell performance and ohmic losses, whereas the shear modulus had a smaller but more geometry-dependent effect. Variations in the in-plane elastic modulus produced only minor changes within the investigated range.

Figure 5.1 shows the polarization behaviour and corresponding ohmic and thermodynamic concentration overpotentials at an applied assembly compression of 1 MPa. Increasing the channel-to-rib ratio reduced concentration losses by improving reactant access, but increased ohmic losses because of the smaller rib area available for current collection. The different geometries therefore shifted the balance between electrical and reactant-transport limitations.

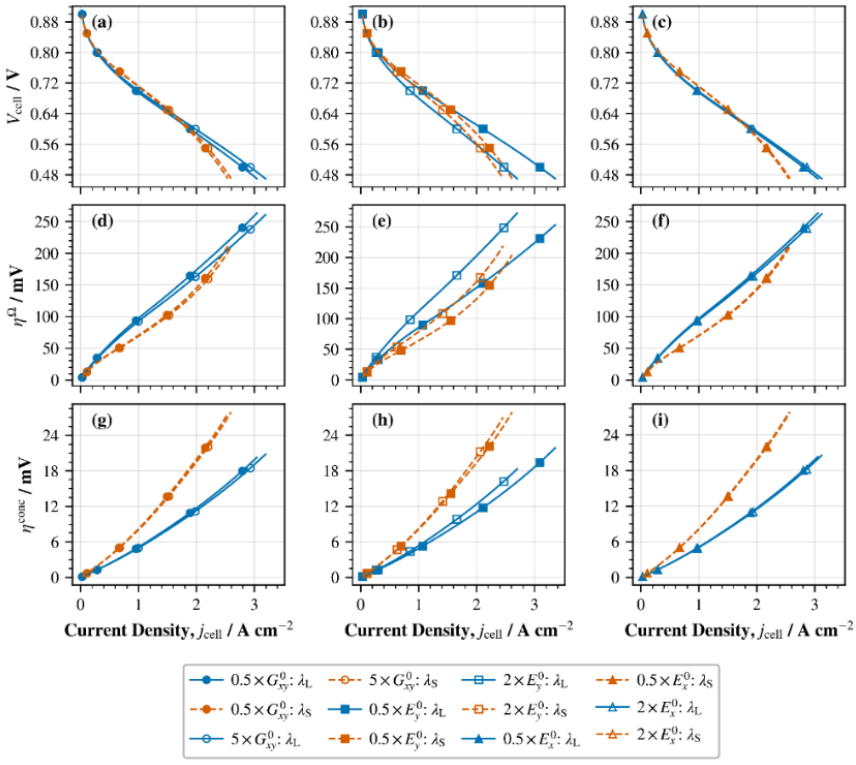

Figure 5.1. Effect of GDL mechanical properties and flow-field geometry on cell performance at an applied compression of 1 MPa. (a–c) Polarization curves, (d–f) ohmic overpotentials, and (g–i) thermodynamic concentration overpotentials for variations in the through-plane shear modulus, through-plane elastic modulus, and in-plane elastic modulus. Adapted from Paper III.

Variations in the GDL mechanical properties affected cell performance primarily through changes in ohmic losses. for the widest-channel geometry, compared with approximately 28 mV for the widest-rib geometry. At 2 A cm^{-2}, varying the through-plane elastic modulus changed the ohmic overpotential by approximately 52 mV. The influence of the shear modulus increased with channel span, producing a change in cell voltage of approximately 17 mV for the widest-channel configuration but only 5–6 mV for the remaining geometries. Corresponding changes due to the in-plane elastic modulus remained below approximately 4 mV.

These trends arise from the different roles of the mechanical properties in establishing the local compression field. The through-plane modulus governs the overall compressive response of the GDL, whereas the shear modulus influences load transfer between the rib-supported and channel-spanning regions. Its effect therefore becomes more pronounced as the unsupported channel width increases. Because the local transport properties and interfacial resistance depend on compression, these mechanical differences propagate directly into the electrochemical response.

Applied compression further modifies this coupling. For the reference flow-field geometry, increasing the compression from 0.5 to 2 MPa reduced the sensitivity to the through-plane elastic modulus: across the investigated modulus range, the variation in ohmic overpotential decreased from approximately 39 to 21 mV. The sensitivity to the shear modulus changed less with applied compression.

Overall, the results show that the influence of GDL mechanical properties on cell performance cannot be considered independently of the flow-field geometry and applied compression.

5.2 Current-density uniformity and co-design

The influence of GDL mechanics and flow-field geometry extends beyond the cell-averaged response and affects the spatial distribution of current generation. This behaviour was quantified using the utilization index (UI), which characterizes the uniformity of the local current density along the GDL–cathode catalyst-layer interface; values approaching unity indicate a more uniform current distribution. Figure 5.2 presents the overall UI together with the corresponding rib and channel contributions for variations in the through-plane shear modulus and through-plane elastic modulus at an applied compression of 1 MPa.

The flow-field geometry has a pronounced influence on current-density uniformity. The intermediate channel-to-rib ratio yields the highest overall utilization, with UI = 0.89, compared with 0.82 for the largest channel-to-rib ratio, 0.80 for the reference geometry, and 0.43 for the smallest ratio. Despite this improvement in uniformity, the mean cell voltage of the intermediate geometry differs from that of the reference geometry by only 1.4 mV. The two measures therefore capture different aspects of cell behaviour: cell voltage reflects the integrated electrochemical response, whereas UI describes how uniformly the electrochemical activity is distributed between the rib and channel regions. A more uniform current distribution does not therefore necessarily imply a higher mean cell performance.

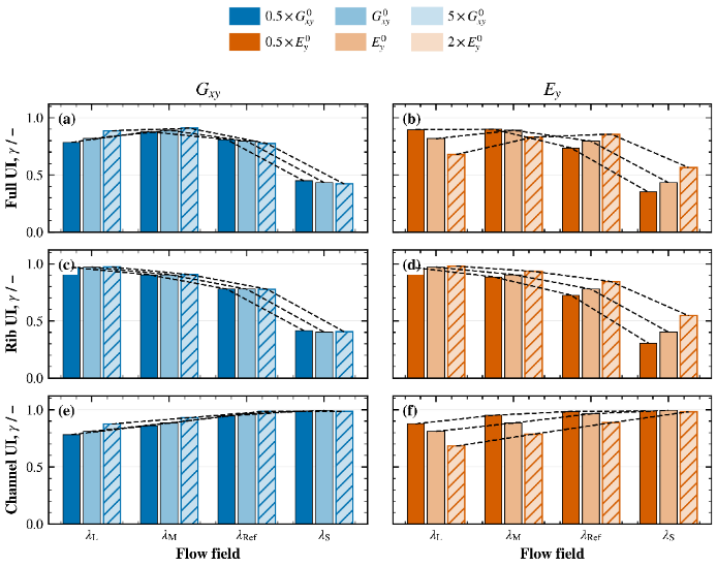

Figure 5.2. Utilization index for variations in the through-plane shear modulus and through-plane elastic modulus across the investigated flow-field geometries at an applied cell compression of 1 MPa. (a,b) Overall utilization index, (c,d) rib contribution, and (e,f) channel contribution. Adapted from Paper III [122] .

The decomposition into rib and channel contributions clarifies the distinct roles of the two through-plane mechanical properties. Increasing the through-plane shear modulus primarily improves utilization beneath the channel, while the rib contribution remains nearly unchanged. This behaviour is consistent with the role of shear stiffness in transferring compressive load from the rib towards the unsupported channel region. The through-plane elastic modulus, by contrast, influences both regions: increasing this modulus generally improves rib utilization while reducing channel utilization. The resulting change in overall UI therefore depends on which region is limiting the current-density uniformity for a given flow-field geometry.

For the smaller channel-to-rib ratios, where the rib region exhibits comparatively low utilization, the improvement in rib utilization dominates and the overall UI increases with increasing through-plane elastic modulus. For the largest channel-to-rib ratio, the channel region instead becomes limiting, and the corresponding reduction in channel utilization leads to a decrease in overall UI. The GDL mechanical properties associated with the highest cell voltage therefore do not necessarily coincide with those that yield the most uniform current distribution.

These results highlight the need to consider GDL mechanical properties and flow-field geometry as a coupled design problem. The through-plane elastic and shear properties influence not only the magnitude of the electrochemical losses, but also their spatial distribution across the rib–channel domain. Cell performance and current-density uniformity should therefore be treated as related, but distinct, design objectives when selecting GDL mechanical characteristics and the corresponding flow-field geometry.

5.3 Surrogate-Assisted GDL Design and Operating-Condition Transfer

The surrogate-assisted analysis was used to examine the coupled influence of GDL properties and flow-field geometry on cell performance and to assess the extent to which design information obtained at one operating condition remains applicable after changes in operating state. The results demonstrate that the absolute cell response is considerably more sensitive to operating conditions than the relative performance of candidate designs. This distinction provides the basis for transferring design information between operating states without requiring complete reconstruction of the target-condition response surface.

5.3.1 Design sensitivity and Transport descriptors

The multi-objective optimization identified a family of non-dominated designs reflecting competing requirements for high mean current density, spatially uniform current generation, and low interfacial contact resistance (Fig. 5.3). Higher $\bar{j}_{\mathrm{cell}}$ was generally associated with increased CV_j, while reductions in ICR through increased rib-supported contact area were accompanied by increased lateral oxygen diffusion length beneath the ribs. The resulting Pareto set therefore represents a balance between through-plane reactant transport, lateral redistribution beneath the ribs, and electronic current collection.

The physics-based transport descriptors provided a complementary interpretation of these trade-offs. Mean cell current density was primarily associated with the through-plane oxygen-transport descriptor d_{tp}, whereas current-density non-uniformity was more strongly associated with the under-rib transport descriptor Π_{rib}. These results indicate that mean performance and spatial current density uniformity are governed by distinct characteristic transport pathways, despite being coupled through the same GDL and flow-field geometry.

The importance of geometry was further demonstrated by the geometry-only optimization. With the transport-property multipliers fixed at their baseline values, the transition from the most uniform solution to the highest current density solution increased $\bar{j}_{\mathrm{cell}}$ by approximately 5%, while CV_j increased by more than a factor of seven. The performance uniformity trade-off can therefore result from GDL thickness and rib width alone and is not contingent on simultaneous variation of the effective transport properties.

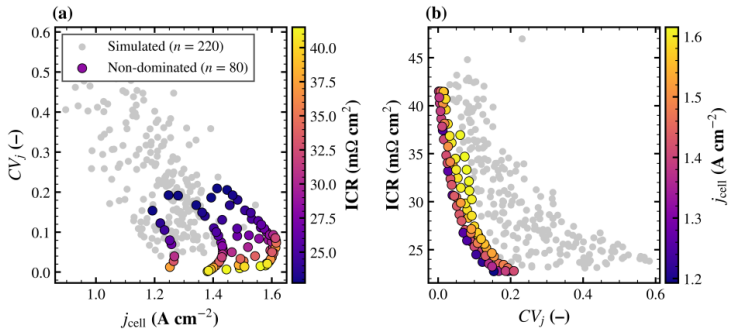

Figure 5.3. Reference-condition Pareto trade-offs for the coupled GDL and flow-field design problem. The non-dominated solutions illustrate the competing requirements for mean cell current density, current-density uniformity, and interfacial contact resistance.

5.3.2 Stability of design relationships across operating conditions

Although the absolute magnitude of the cell response changed with operating condition, the physical relationship between current-density non-uniformity and the under-rib transport descriptor remained comparatively stable. Across the investigated oxygen concentrations, temperatures, relative humidities, and cell voltages, CV_j retained a strong monotonic association with Π_{rib} as indicated by Spearman rank correlations of 0.92-0.96 (Fig. 5.4) and log-log coefficient of determination of 0.81-0.92 (Fig.5.4b). Variations in operating state altered the magnitude and slope of the response but did not fundamentally change the ordering imposed by under-rib transport limitations.

This behaviour indicates that Π_{rib} provides a common physical coordinate for interpreting current-density non-uniformity over the investigated operating domain. Since the descriptor incorporates rib width, GDL thickness, in-plane tortuosity, and averaged compressed porosity, the observed relationship relates spatial current variation with the combined geometric and diffusive resistance governing oxygen supply beneath the ribs.

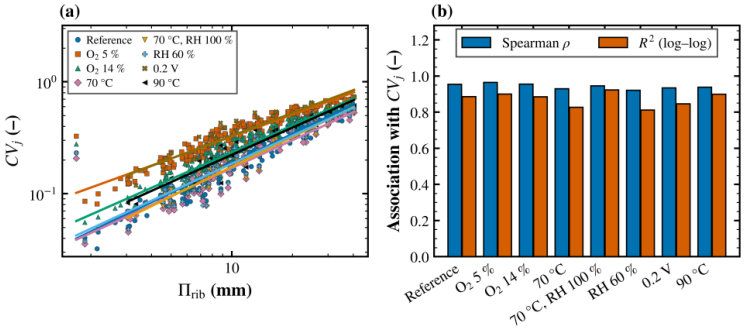

Figure 5.4. (a) Current-density non-uniformity as a function of the under-rib transport descriptor Π_{rib} across the investigated operating conditions. (b) Spearman rank correlation and log–log coefficient of determination between Π_{rib} and CV_j for each condition. The relationship remains strongly monotonic despite condition-dependent changes in response magnitude.

The same distinction was evident when the complete design population was compared between operating states. Direct transfer of reference-condition responses resulted in poor absolute predictions for several of the larger operating shifts, including strongly negative zero-shot R^2 values (Fig. 5.5a). In contrast, the relative ordering of the designs was largely maintained, with Spearman correlations of approximately 0.83-0.99 across all seven shifts (Fig. 5.5b).

The contrast between absolute prediction and rank preservation is central to the transfer analysis. Changes in operating conditions may shift or rescale the response surface without equivalently modifying the relative merit of candidate designs. Consequently, accurate prediction of absolute target-condition responses is not a prerequisite for retaining useful information about favourable regions of the design space.

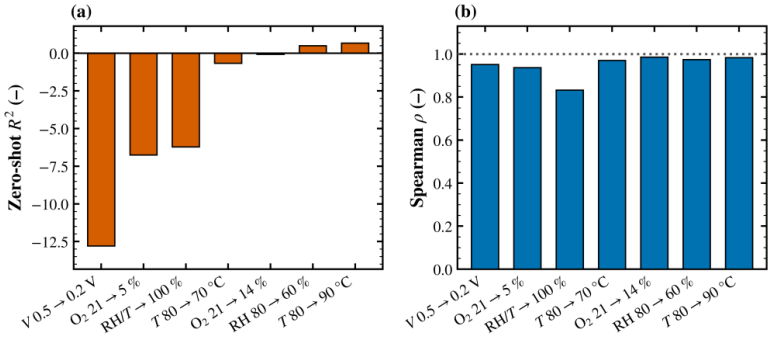

Figure 5.5. Cross-condition comparison of absolute response transfer and design ranking. (a) Zero-shot coefficient of determination, R^2, obtained by transferring the reference-condition response directly to modified operating states. (b) Corresponding Spearman rank correlation, ρ, between reference- and target-condition responses.

5.3.3 Reuse of optimization results across operating conditions

The preservation of design rankings extended to multi-objective performance, with the reference-condition Pareto set recovering 97.1–100% of the target-condition hypervolume across the seven operating-condition shifts (Fig. 5.6). A probabilistic certification procedure was subsequently applied to assess whether these designs could be reused without repeating the full optimization campaigns. Reuse was accepted when a lower quantile of the estimated retained hypervolume exceeded 0.95 in at least 90% of twenty independent anchor selections. Six shifts satisfied this criterion, requiring between five and eight target-condition evaluations each. This corresponded to 39 evaluations compared with 459 for the complete campaigns, a reduction of 91.5%. The 5% oxygen shift could not be certified because the estimated lower bound on retained hypervolume remained below the prescribed threshold of 0.95, despite the high retrospective transfer performance. This outcome does not indicate that reuse was unsuccessful, but rather that the available evidence was insufficient to establish its reliability under the certification criterion. In contrast, the remaining six operating-condition shifts satisfied the criterion, demonstrating the potential for substantial computational savings through the certified reuse of previously optimized designs.

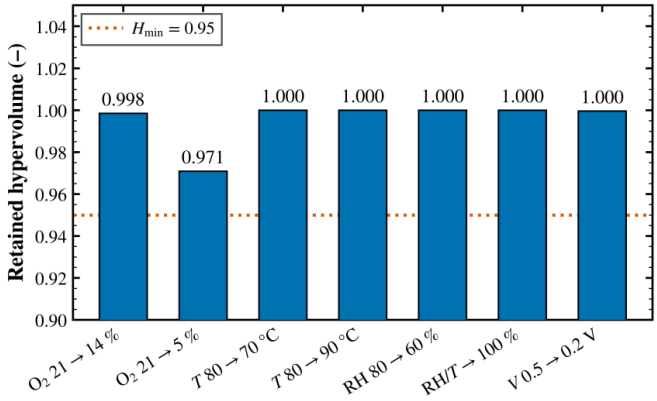

Figure 5.6. Retrospective retained hypervolume of reference-condition non-dominated selections evaluated at the target operating conditions. The retained hypervolume is calculated relative to the corresponding complete paired design population. The dotted line indicates the prescribed reuse threshold of 0.95.

6. Conclusions and future work

6.1 Conclusions

The findings of this thesis establish that GDL selection must account for material architecture, assembly compression, and flow-field geometry. Increasing compression improved electrical and thermal conduction while reducing in-plane gas permeability, with material-specific responses that emphasize the importance of characterization under representative assembly conditions. Increasing PTFE loading from 5 to 20 wt% produced only modest changes in pressure-dependent dry oxygen-transport resistance, whereas differences between substrates were considerably greater. Microscopy revealed that native binder influences PTFE deposition, demonstrating that the transport consequences of hydrophobic treatment depend on the underlying substrate architecture rather than nominal loading alone.

The coupled mechanical–electrochemical analysis identified through-plane elastic stiffness as the dominant mechanical influence on predicted cell performance, while shear stiffness became increasingly important with greater unsupported channel spans. Lower through-plane stiffness generally favoured cell voltage, whereas greater stiffness improved current-density uniformity at smaller channel-to-rib ratios but reduced it at the largest ratio investigated. These findings establish geometry-dependent mechanical requirements, with through-plane stiffness influencing the balance between performance and uniformity and shear stiffness warranting particular attention for wider unsupported channel span.

The transport analysis revealed distinct requirements for mean current density and spatial uniformity. Lower through-plane oxygen-transport resistance favoured higher mean current density, whereas greater in-plane diffusive conductance facilitated oxygen redistribution beneath the ribs. Wider ribs consequently place greater demands on lateral oxygen transport, while narrower ribs reduce the available electrical contact area. Increasing GDL thickness provides a larger cross-section for lateral diffusion but also extends the through-plane transport pathway. These competing effects provide a physical basis for selecting GDL thickness, directional transport properties, and rib geometry according to the required balance between current output, spatial uniformity, and interfacial contact resistance.

Surrogate-assisted multi-objective optimization quantified these trade-offs and identified favourable GDL–flow-field combinations, providing a systematic basis for engineering design decisions. The reference-condition Pareto set recovered 97.1–100% of the target-condition hypervolume across seven operating shifts. For the six less severe conditions, sparse certification reduced the number of required continuum-model evaluations by 80.4% relative to complete target campaigns. Severe oxygen depletion remained an exception, demonstrating that favourable retrospective transfer performance does not necessarily establish reliable reuse from limited target-condition information.

The comparison of pristine GDL material with material recovered after prolonged fuel cell operation revealed differences in wettability and pore-throat structure accompanied by changes in capillary water retention. The aged substrate exhibited higher liquid-water saturation at low capillary pressures, whereas the pristine material reached higher saturation at elevated pressures. This crossover is consistent with competing influences of wettability and pore-network accessibility on liquid-water invasion. Despite these differences, the relative diffusivity–saturation relationships remained broadly similar, indicating comparable fractional reductions in gas diffusivity at a given saturation. The

consequences of prolonged operation for oxygen transport therefore depend on both the capillary pressure–saturation relationship and dry effective diffusivity, rather than relative diffusivity alone.

6.2 Future work

Future investigations should prioritize experimental validation of the geometry-dependent GDL selection criteria. Measurements of directional effective gas diffusivity under compression and partial liquid-water saturation, combined with limiting-current experiments, spatially resolved current-density mapping, and operando water imaging, would help establish how material properties and flow-field geometry influence local reactant transport and electrochemical performance.

Higher-resolution X-ray tomography and image-based mechanical modelling could further clarify how MPL morphology, deformation, and liquid-water invasion affect effective transport properties. Investigations across different GDL materials, stack locations, and operating histories would help distinguish degradation-related changes from structural variability. Larger imaging datasets could also support three-dimensional convolutional neural networks and graph neural networks for predicting effective transport properties from pore structure and connectivity.

Finally, extending the surrogate-assisted optimization framework to experimentally characterized GDL material classes would allow relationships between their mechanical and transport properties to be incorporated into the design process. Experimental evaluation of selected Pareto-optimal configurations would further strengthen the connection between the predicted design trade-offs and material-specific GDL–flow-field selection.

References

[1] Energy Agency I. World Energy Outlook 2025. 2025.

[2] Working Group III contribution to the Sixth Assessment Report of the Intergovernmental Panel on Climate Change Mitigation of Climate Change. 2022.

[3] Guo H, Chen L, Ismail SA, Jiang L, Guo S, Gu J, et al. Gas Diffusion Layer for Proton Exchange Membrane Fuel Cells: A Review. Materials 2022;15. https://doi.org/10.3390/ma15248800.

[4] Okonkwo PC, Otor C. A review of gas diffusion layer properties and water management in proton exchange membrane fuel cell system. Int J Energy Res 2021;45:3780–800. https://doi.org/10.1002/er.6227.

[5] Mortazavi M, Tajiri K. Effect of the PTFE content in the gas diffusion layer on water transport in polymer electrolyte fuel cells (PEFCs). J Power Sources 2014;245:236–44. https://doi.org/10.1016/j.jpowsour.2013.06.138.

[6] Eller J, Lamibrac A, Marone F, Buchi F. Influence of Binder Porosity on Gdl Gas Phase Transport, ECS; 2016.

[7] Mo J, Zhang C, Zheng W, Hu Y, Li Z, Suekane T. Influence of binder content on gas-water two-phase flow and displacement phase diagram in the gas diffusion layer of PEMFC: A pore network view. Int J Heat Mass Transf 2024;231. https://doi.org/10.1016/j.ijheatmasstransfer.2024.125838.

[8] Ismail MS, Damjanovic T, Ingham DB, Pourkashanian M, Westwood A. Effect of polytetrafluoroethylene-treatment and microporous layer-coating on the electrical conductivity of gas diffusion layers used in proton exchange membrane fuel cells. J Power Sources 2010;195:2700–8. https://doi.org/10.1016/j.jpowsour.2009.11.069.

[9] Weber AZ, Newman J, Soc JE, Weber AZ, Newman J. Effects of Microporous Layers in Polymer Electrolyte Fuel Cells Effects of Microporous Layers in Polymer Electrolyte Fuel Cells 2005. https://doi.org/10.1149/1.1861194.

[10] Chen W, Jiang F. Impact of PTFE content and distribution on liquid-gas flow in PEMFC carbon paper gas distribution layer: 3D lattice Boltzmann simulations. Int J Hydrogen Energy 2016. https://doi.org/10.1016/j.ijhydene.2016.02.159.

[11] Liu F, Wang Q, Li B, Zhang C, Ming P. Effect of PTFE and liquid water on the thermal characteristics of compressed gas diffusion backing of PEM fuel cell. ETransportation 2022;12. https://doi.org/10.1016/j.etran.2022.100162.

[12] McCarthy N, Chen R, Offer G, Thring R. PTFE mapping in gas diffusion media for PEMFCs using fluorescence microscopy. Int J Hydrogen Energy 2016;41:17631–43. https://doi.org/10.1016/j.ijhydene.2016.07.270.

[13] Barbir F. Main Cell Components, Material Properties, and Processes. PEM Fuel Cells, 2013, p. 73–117. https://doi.org/10.1016/b978-0-12-387710-9.00004-7.

[14] Barbir F. Fuel Cell Electrochemistry. PEM Fuel Cells, 2013, p. 33–72. https://doi.org/10.1016/b978-0-12-387710-9.00003-5.

[15] Thesis D. Transport phenomena on the channel-rib scale of polymer electrolyte fuel cells 2009.

[16] Zhao X, Wang Z, Xiao L, Zha Y, Deng G, Li S, et al. Corrosion-Resistant and Conductive Coatings on 316L Stainless Steel Bipolar Plates Fabricated by Hot Rolling. Materials 2025;18. https://doi.org/10.3390/ma18081831.

[17] Alo OA, Otunniyi IO, Pienaar HcZ. Manufacturing methods for metallic bipolar plates for polymer electrolyte membrane fuel cell. Materials and Manufacturing Processes 2019;34:927–55. https://doi.org/10.1080/10426914.2019.1605170.

[18] Spernjak D, Prasad AK, Advani SG. In situ comparison of water content and dynamics in parallel, single-serpentine, and interdigitated flow fields of polymer electrolyte membrane fuel cells. J Power Sources 2010;195:3553–68. https://doi.org/10.1016/j.jpowsour.2009.12.031.

[19] Cooper NJ, Santamaria AD, Becton MK, Park JW. Investigation of the performance improvement in decreasing aspect ratio interdigitated flow field PEMFCs. Energy Convers Manag 2017;136:307–17. https://doi.org/10.1016/j.enconman.2017.01.005.

[20] Alam Rimon ST, Shajid SR, Mourshed M, Hasan Khan Tushar MS. Flow field configurations in PEMFCs: Design, Modeling, and performance insights. Energy Conversion and Management: X 2025;28. https://doi.org/10.1016/j.ecmx.2025.101263.

[21] Wang Y, Liao X, Liu G, Xu H, Guan C, Wang H, et al. Review of Flow Field Designs for Polymer Electrolyte Membrane Fuel Cells. Energies (Basel) 2023;16. https://doi.org/10.3390/en16104207.

[22] Zhou ZQ, Wang JX, Hu HY, Hou HL. Achievements in protective coatings for metallic bipolar plates in proton exchange membrane fuel cells: a comprehensive review. Engineering Research Express 2025;7. https://doi.org/10.1088/2631-8695/adc34c.

[23] Guo J, Li X, Ouyang Z, Shao Z. A comprehensive review of metallic bipolar plates in PEMFCs of surface engineering and new materials development. Int J Hydrogen Energy 2025;137:553–74. https://doi.org/10.1016/j.ijhydene.2025.05.093.

[24] Bohackova T, Ludvik J, Kouril M. Metallic material selection and prospective surface treatments for proton exchange membrane fuel cell bipolar plates—a review. Materials 2021;14. https://doi.org/10.3390/ma14102682.

[25] Forouzanmehr M, Kashyzadeh KR, Borjali A, Ivanov A, Jafarnode M, Gan TH, et al. Detection and Analysis of Corrosion and Contact Resistance Faults of TiN and CrN Coatings on 410 Stainless Steel as Bipolar Plates in PEM Fuel Cells. Sensors 2022;22. https://doi.org/10.3390/s22030750.

[26] Irshad HM, Shahgaldi S. Comprehensive review of bipolar plates for proton exchange membrane fuel cells with a focus on materials, processing methods and characteristics. Int J Hydrogen Energy 2025;111:462–87. https://doi.org/10.1016/j.ijhydene.2025.02.300.

[27] Hu T, Chen D, Chi C, Hu S, Ma F, Li Y, et al. High-performance Ag-doped multilayer amorphous carbon coatings on metallic bipolar plates for proton exchange membrane fuel cells. Diam Relat Mater 2025;158. https://doi.org/10.1016/j.diamond.2025.112613.

[28] Zhang R, Lan S, Xu Z, Qiu D, Peng L. Investigation and optimization of the ultra-thin metallic bipolar plate multi-stage forming for proton exchange membrane fuel cell. J Power Sources 2021;484. https://doi.org/10.1016/j.jpowsour.2020.229298.

[29] Peker MF, Cora ÖN, Koç M. Micro-stamping of PEMFC bipolar plates-investigations on the effect of friction, coating and surface quality interactions on the corrosion resistance characteristics. n.d.

[30] Lee FC, Ismail MS, Ingham DB, Hughes KJ, Ma L, Lyth SM, et al. Alternative architectures and materials for PEMFC gas diffusion layers: A review and outlook. Renewable and Sustainable Energy Reviews 2022;166. https://doi.org/10.1016/j.rser.2022.112640.

[31] Graphite Solutions Powering up fuel cells SIGRACET ®. n.d.

[32] Berger A, Striednig M, Simon C, Gasteiger HA. Determination of the τ/ε-Ratio for Gas Diffusion Substrates and Microporous Layers in a Proton Exchange Membrane Fuel Cell. J Electrochem Soc 2025;172:014508. https://doi.org/10.1149/1945-7111/ada63e.

[33] Mathias M, Roth J, Fleming J, Lehnert W. Chapter 46 Diffusion media materials and characterisation. n.d.

[34] Kleemann J, Finsterwalder F, Tillmetz W. Characterisation of mechanical behaviour and coupled electrical properties of polymer electrolyte membrane fuel cell gas diffusion layers. J Power Sources 2009;190:92–102. https://doi.org/10.1016/j.jpowsour.2008.09.026.

[35] Ozden A, Shahgaldi S, Li X, Hamdullahpur F. A review of gas diffusion layers for proton exchange membrane fuel cells—With a focus on characteristics, characterization techniques, materials and designs. Prog Energy Combust Sci 2019. https://doi.org/10.1016/j.pecs.2019.05.002.

[36] García-Salaberri PA, Vera M, Zaera R. Nonlinear orthotropic model of the inhomogeneous assembly compression of PEM fuel cell gas diffusion layers. Int J Hydrogen Energy 2011. https://doi.org/10.1016/j.ijhydene.2011.05.152.

[37] Zenyuk I V., Parkinson DY, Connolly LG, Weber AZ. Gas-diffusion-layer structural properties under compression via X-ray tomography. J Power Sources 2016;328:364–76. https://doi.org/10.1016/j.jpowsour.2016.08.020.

[38] Chen J, Gao W, Ning T, Meng L, Yin Y, Ouyang H, et al. Effect of GDL compression on PEMFC performance: A comprehensive cross-scale study. Chemical Engineering Journal 2025;503. https://doi.org/10.1016/j.cej.2024.158542.

[39] Bazylak A, Sinton D, Liu ZS, Djilali N. Effect of compression on liquid water transport and microstructure of PEMFC gas diffusion layers. J Power Sources 2007;163:784–92. https://doi.org/10.1016/j.jpowsour.2006.09.045.

[40] Zhu L, Zhang H, Xiao L, Bazylak A, Gao X, Sui PC. Pore-scale modeling of gas diffusion layers: Effects of compression on transport properties. J Power Sources 2021;496. https://doi.org/10.1016/j.jpowsour.2021.229822.

[41] Kulkarni N, Cho JIS, Jervis R, Roberts EPL, Francesco I, Kok MDR, et al. The effect of non-uniform compression on the performance of polymer electrolyte fuel cells. J Power Sources 2022;521. https://doi.org/10.1016/j.jpowsour.2021.230973.

[42] Simon C, Hasché F, Müller D, Gasteiger HA. Influence of the Gas Diffusion Layer Compression on the Oxygen Mass Transport in PEM Fuel Cells. ECS Trans 2015;69:1293–302. https://doi.org/10.1149/06917.1293ecst.

[43] Chippar P, Kyeongmin O, Kang K, Ju H. A numerical investigation of the effects of GDL compression and intrusion in polymer electrolyte fuel cells (PEFCs). Int J Hydrogen Energy 2012;37:6326–38. https://doi.org/10.1016/j.ijhydene.2011.04.154.

[44] Millichamp J, Mason TJ, Neville TP, Rajalakshmi N, Jervis R, Shearing PR, et al. Mechanisms and effects of mechanical compression and dimensional change in polymer electrolyte fuel cells - A review. J Power Sources 2015;284:305–20. https://doi.org/10.1016/j.jpowsour.2015.02.111.

[45] Qiu D, Janßen H, Peng L, Irmscher P, Lai X, Lehnert W. Electrical resistance and microstructure of typical gas diffusion layers for proton exchange membrane fuel cell under compression. Appl Energy 2018;231:127–37. https://doi.org/10.1016/j.apenergy.2018.09.117.

[46] Molaeimanesh GR, Nazemian M. Investigation of GDL compression effects on the performance of a PEM fuel cell cathode by lattice Boltzmann method. J Power Sources 2017;359:494–506. https://doi.org/10.1016/j.jpowsour.2017.05.078.

[47] Khajeh-Hosseini-Dalasm N, Sasabe T, Tokumasu T, Pasaogullari U. Effects of polytetrafluoroethylene treatment and compression on gas diffusion layer microstructure using high-resolution X-ray computed tomography. J Power Sources 2014;266:213–21. https://doi.org/10.1016/j.jpowsour.2014.05.004.

[48] Hottinen T, Himanen O, Karvonen S, Nitta I. Inhomogeneous compression of PEMFC gas diffusion layer. Part II. Modeling the effect. J Power Sources 2007;171:113–21. https://doi.org/10.1016/j.jpowsour.2006.10.076.

[49] Mortazavi M, Santamaria AD, Chauhan V, Benner JZ, Heidari M, Médici EF. Effect of PEM fuel cell porous media compression on in-plane transport phenomena. Journal of Power Sources Advances 2020;1:100001. https://doi.org/10.1016/j.powera.2020.100001.

[50] Bouziane K, Khetabi EM, Lachat R, Candusso D, Meyer Y. Methods to Measure the Electrical Resistances of a Gas Diffusion Layer Under Mechanical Compression. Fuel Cells 2024;24. https://doi.org/10.1002/fuce.202200102.

[51] Lee WK, Ho CH, Van Zee JW, Murthy M. Effects of compression and gas diffusion layers on the performance of a PEM fuel cell. J Power Sources 1999;84:45–51. https://doi.org/10.1016/S0378-7753(99)00298-0.

[52] García-Salaberri PA, Sánchez-Ramos A. A numerical analysis of the effect of layer-scale and microscopic parameters of membrane electrode assembly in proton exchange fuel cells under two-phase conditions. J Power Sources 2024;593. https://doi.org/10.1016/j.jpowsour.2023.233950.

[53] García-Salaberri PA, Sánchez-Ramos A. Modeling of a polymer electrolyte membrane fuel cell with a hybrid continuum/discrete formulation at the rib/channel scale: Effect of relative humidity and temperature on performance and two-phase transport. Appl Energy 2024;367. https://doi.org/10.1016/j.apenergy.2024.123332.

[54] García-Salaberri PA, Das PK. Effective transport properties for fuel cells: modeling and experimental characterization. Fuel Cells for Transportation: Fundamental Principles and Applications, Elsevier; 2023, p. 199–224. https://doi.org/10.1016/B978-0-323-99485-9.00011-3.

[55] L Dullien FA, York London Toronto Sydney San Francisco N. Porous Media Fluid Transport and Pore Structure. n.d.

[56] Kirkpatrick S. Percolation and Conduction. Rev Mod Phys 1973;45:574–88. https://doi.org/10.1103/RevModPhys.45.574.

[57] Zamel N, Li X. Effective transport properties for polymer electrolyte membrane fuel cells - With a focus on the gas diffusion layer. Prog Energy Combust Sci 2013;39:111–46. https://doi.org/10.1016/j.pecs.2012.07.002.

[58] Flückiger R, Freunberger SA, Kramer D, Wokaun A, Scherer GG, Büchi FN. Anisotropic, effective diffusivity of porous gas diffusion layer materials for PEFC. Electrochim Acta 2008;54:551–9. https://doi.org/10.1016/j.electacta.2008.07.034.

[59] Zamel N, Li X. Effective transport properties for polymer electrolyte membrane fuel cells - With a focus on the gas diffusion layer. Prog Energy Combust Sci 2013;39:111–46. https://doi.org/10.1016/j.pecs.2012.07.002.

[60] 6 Multiphase Flow of Immiscible Fluids in Porous Media. n.d.

[61] Single-Phase Transport 4 Phenomena in Porous Media. n.d.

[62] Klinkenberg LJ. THE PERMEABILITY OF POROUS MEDIA TO LIQUIDS AND GASES "f. n.d.

[63] L Capillarity in Porous Media. n.d.

[64] Eller J, Stampanoni M, Schmidt TJ. X-ray Tomographic Microscopy of Polymer Electrolyte Fuel Cells. n.d.

[65] Lamibrac A, Roth J, Toulec M, Marone F, Stampanoni M, Büchi FN. Characterization of Liquid Water Saturation in Gas Diffusion Layers by X-Ray Tomographic Microscopy. J Electrochem Soc 2016;163:F202–9. https://doi.org/10.1149/2.0401603jes.

[66] Zenyuk I V., Parkinson DY, Hwang G, Weber AZ. Probing water distribution in compressed fuel-cell gas-diffusion layers using X-ray computed tomography. Electrochem Commun 2015;53:24–8. https://doi.org/10.1016/j.elecom.2015.02.005.

[67] Gostick JT, Ioannidis MA, Fowler MW, Pritzker MD. Direct measurement of the capillary pressure characteristics of water-air-gas diffusion layer systems for PEM fuel cells. Electrochem Commun 2008;10:1520–3. https://doi.org/10.1016/j.elecom.2008.08.008.

[68] Fairweather JD, Cheung P, St-Pierre J, Schwartz DT. A microfluidic approach for measuring capillary pressure in PEMFC gas diffusion layers. Electrochem Commun 2007;9:2340–5. https://doi.org/10.1016/j.elecom.2007.06.042.

[69] Dubau L, Castanheira L, Maillard F, Chatenet M, Lottin O, Maranzana G, et al. A review of PEM fuel cell durability: Materials degradation, local heterogeneities of aging and possible

mitigation strategies. Wiley Interdiscip Rev Energy Environ 2014;3:540–60. https://doi.org/10.1002/wene.113.

[70] Edjokola JM, Heidinger M, Niroumand A, Hacker V, Bodner M. Chemical Oxidation-Induced Degradation in Gas Diffusion Layers for PEFC: Mechanisms and Performance Implications. J Electrochem Soc 2024. https://doi.org/10.1149/1945-7111/ad790a.

[71] Moon JW, Kim SK, Jung SY. In-situ visualization of cathode flow channel in polymer electrolyte membrane fuel cell: Effect of GDL degradation. Int J Hydrogen Energy 2024;51:1255–63. https://doi.org/10.1016/j.ijhydene.2023.03.342.

[72] Bosomoiu M, Tsotridis G, Bednarek T. Study of effective transport properties of fresh and aged gas diffusion layers. J Power Sources 2015;285:568–79. https://doi.org/10.1016/j.jpowsour.2015.03.132.

[73] Arlt T, Klages M, Messerschmidt M, Scholta J, Manke I. Influence of artificially aged gas diffusion layers on the water management of polymer electrolyte membrane fuel cells analyzed with in-operando synchrotron imaging. Energy 2017;118:502–11. https://doi.org/10.1016/j.energy.2016.10.061.

[74] Zucconi A, Hack J, Stocker R, Suter TAM, Rettie AJE, Brett DJL. Challenges and opportunities for characterisation of high-temperature polymer electrolyte membrane fuel cells: a review. J Mater Chem A Mater 2024;12:8014–64. https://doi.org/10.1039/d3ta06895a.

[75] Lee J, Carreon Ruiz ER, Kaestner A, Trtik P, Strobl M, Boillat P. Framework for processing operando neutron radiography of energy devices. Sci Rep 2025;15. https://doi.org/10.1038/s41598-025-09425-w.

[76] Wijaya YP, Orfino FP, Kjeang E. X-ray Computed Tomography Visualization of Liquid Water in Proton Exchange Membrane Fuel Cells: A State-of-the-Art Review. ACS Appl Energy Mater 2025;8:12997–3019. https://doi.org/10.1021/acsaem.5c01284.

[77] Lang YL, Guo H, Ye F, Chen H. A review of X-ray water imaging studies applied to the gas diffusion layer of proton exchange membrane fuel cells. Renewable and Sustainable Energy Reviews 2025;221. https://doi.org/10.1016/j.rser.2025.115919.

[78] Matsui H, Ohta T, Nakamura T, Uruga T, Tada M. In situ 3D X-ray imaging of water distribution in each layer of a membrane electrode assembly of a polymer electrolyte fuel cell. Physical Chemistry Chemical Physics 2024;26:15115–9. https://doi.org/10.1039/d4cp00728j.

[79] Wang CY. Fundamental models for fuel cell engineering. Chem Rev 2004;104:4727–65. https://doi.org/10.1021/cr020718s.

[80] Mukherjee PP, Kang Q, Wang CY. Pore-scale modeling of two-phase transport in polymer electrolyte fuel cells - Progress and perspective. Energy Environ Sci 2011;4:346–69. https://doi.org/10.1039/b926077c.

[81] Weber AZ, Borup RL, Darling RM, Das PK, Dursch TJ, Gu W, et al. A Critical Review of Modeling Transport Phenomena in Polymer-Electrolyte Fuel Cells. J Electrochem Soc 2014;161:F1254–99. https://doi.org/10.1149/2.0751412jes.

[82] Chen K, Luo Z, Zou G, He D, Xiong Z, Zhou Y, et al. Multi-objective optimization of gradient gas diffusion layer structures for enhancing proton exchange membrane fuel cell performance

based on response surface methodology and non-dominated sorting genetic algorithm-III. Energy 2024;288. https://doi.org/10.1016/j.energy.2023.129793.

[83] Omongos R Lou, Galvez-Aranda DE, Zanotto FM, Vernes A, Franco AA. Machine learning-driven optimization of gas diffusion layer microstructure for PEM fuel cells. J Power Sources 2025;625. https://doi.org/10.1016/j.jpowsour.2024.235583.

[84] Wang J, Jiang H, Chen G, Wang H, Lu L, Liu J, et al. Integration of multi-physics and machine learning-based surrogate modelling approaches for multi-objective optimization of deformed GDL of PEM fuel cells. Energy and AI 2023;14. https://doi.org/10.1016/j.egyai.2023.100261.

[85] Sun J, Lin P, Zeng L, Guo Z, Jiang Y, Xiao C, et al. Artificial-intelligence-guided design of ordered gas diffusion layers for high-performing fuel cells via Bayesian machine learning. Nature Communications 2025;16. https://doi.org/10.1038/s41467-025-61794-y.

[86] Pan Y, Ruan H, Wu B, Regmi YN, Wang H, Brandon NP. A machine learning driven 3D+1D model for efficient characterization of proton exchange membrane fuel cells. Energy and AI 2024;17. https://doi.org/10.1016/j.egyai.2024.100397.

[87] Garcí-Salaberri PA. General aspects in the modeling of fuel cells: From conventional fuel cells to nano fuel cells. Nanotechnology in Fuel Cells, Elsevier; 2022, p. 77–121. https://doi.org/10.1016/B978-0-323-85727-7.00015-1.

[88] Weber AZ, Newman J. Modeling transport in polymer-electrolyte fuel cells. Chem Rev 2004;104:4679–726. https://doi.org/10.1021/cr020729l.

[89] Tranter TG, Gostick JT, Burns AD, Gale WF. Pore Network Modeling of Compressed Fuel Cell Components with OpenPNM. Fuel Cells 2016;16:504–15. https://doi.org/10.1002/fuce.201500168.

[90] Schulz VP, Wargo EA, Kumbur EC. Pore-Morphology-Based Simulation of Drainage in Porous Media Featuring a Locally Variable Contact Angle. Transp Porous Media 2015;107:13–25. https://doi.org/10.1007/s11242-014-0422-4.

[91] Erfani H, Haghani R, McClure J, Boek E, Berg CF. Spatial Characterization of Wetting in Porous Media Using Local Lattice-Boltzmann Simulations. Transp Porous Media 2024;151:429–48. https://doi.org/10.1007/s11242-023-02044-x.

[92] Hao L, Cheng P. Lattice Boltzmann simulations of anisotropic permeabilities in carbon paper gas diffusion layers. J Power Sources 2009. https://doi.org/10.1016/j.jpowsour.2008.09.086.

[93] Pourrahmani H, Hosseini M, Moussaoui H, Oveisi E, Siavashi M, Van Herle J. Quantitative measurement and comparison of breakthroughs inside the gas diffusion layer using lattice Boltzmann method and computed tomography scan. Sci Rep 2024;14. https://doi.org/10.1038/s41598-024-60148-w.

[94] Schulz VP, Becker J, Wiegmann A, Mukherjee PP, Wang C-Y. Modeling of Two-Phase Behavior in the Gas Diffusion Medium of PEFCs via Full Morphology Approach. J Electrochem Soc 2007;154:B419. https://doi.org/10.1149/1.2472547.

[95] Zubov AS, Khlyupin AN, Karsanina M V., Gerke KM. In search for representative elementary volume (REV) within heterogeneous materials: A survey of scalar and vector metrics using

porous media as an example. Adv Water Resour 2024;192. https://doi.org/10.1016/j.advwatres.2024.104762.

[96] Al-Raoush R, Papadopoulos A. Representative elementary volume analysis of porous media using X-ray computed tomography. Powder Technol 2010;200:69–77. https://doi.org/10.1016/j.powtec.2010.02.011.

[97] Wang J, Jiang H, Chen G, Wang H, Lu L, Liu J, et al. Integration of multi-physics and machine learning-based surrogate modelling approaches for multi-objective optimization of deformed GDL of PEM fuel cells. Energy and AI 2023;14. https://doi.org/10.1016/j.egyai.2023.100261.

[98] Rosmin APP, Hidayat MIP, Pramata AD. Recent progress on machine learning techniques for flow field optimization toward performance and commercial scale proton exchange membrane fuel cell: A systematic review. Results in Engineering 2026;29. https://doi.org/10.1016/j.rineng.2026.109519.

[99] Tamilarasan S, Wang CK, Kuan Y Der, Shih YC, Stachiv I. Machine learning as a catalyst for PEMFC optimization: A comprehensive review from flow fields to system integration with a multiscale perspective on research and applications. Renewable and Sustainable Energy Reviews 2026;226. https://doi.org/10.1016/j.rser.2025.116274.

[100] Rasmussen CEdward, Williams CKI. Gaussian processes for machine learning. MIT Press; 2006.

[101] Marrel A, Iooss B. Probabilistic surrogate modeling by Gaussian process: A review on recent insights in estimation and validation. Reliab Eng Syst Saf 2024;247. https://doi.org/10.1016/j.ress.2024.110094.

[102] Zhang X, Yu G, Jin Y, Qian F. An adaptive Gaussian process based manifold transfer learning to expensive dynamic multi-objective optimization. Neurocomputing 2023;538. https://doi.org/10.1016/j.neucom.2023.03.073.

[103] Kennedy MC, O'hagan A. Bayesian calibration of computer models. n.d.

[104] Daulton S, Balandat M, Bakshy E. Parallel Bayesian Optimization of Multiple Noisy Objectives with Expected Hypervolume Improvement 2021.

[105] Feser JP, Prasad AK, Advani SG. Experimental characterization of in-plane permeability of gas diffusion layers. J Power Sources 2006;162:1226–31. https://doi.org/10.1016/j.jpowsour.2006.07.058.

[106] Ringström M, Ekström H, Kylhammar L, Lindbergh G, Lindström RW. Comprehensive ex-situ characterization of the compression-dependent properties of gas diffusion layers in PEM fuel cells. Energy Convers Manag 2026;356. https://doi.org/10.1016/j.enconman.2026.121319.

[107] Xvii V, Edward Washburn Synopsis BW. Second Series MGrck, Ig2I P H YSICAL REVIEW. THE DYNAMICS OF CAPILLARY FLOK. n.d.

[108] Schulz D, Ringström M, Sankar SR, Martinelli A. The Role of Native Binder in Controlling the Polytetrafluoroethylene Distribution in Gas Diffusion Layers for Proton Exchange Membrane Fuel Cells. Fuel Cells 2026;26. https://doi.org/10.1002/fuce.70139.

[109] Baker DR, Wieser C, Neyerlin KC, Murphy MW. The Use of Limiting Current to Determine Transport Resistance in PEM Fuel Cells. ECS Trans 2006;3:989–99. https://doi.org/10.1149/1.2356218.

[110] Chen YC, Karageorgiou C, Eller J, Schmidt TJ, Büchi FN. Determination of the porosity and its heterogeneity of fuel cell microporous layers by X-ray tomographic microscopy. J Power Sources 2022;539. https://doi.org/10.1016/j.jpowsour.2022.231612.

[111] Wang JX, Springer TE, Adzic RR. Dual-Pathway Kinetic Equation for the Hydrogen Oxidation Reaction on Pt Electrodes. J Electrochem Soc 2006;153:A1732. https://doi.org/10.1149/1.2218756.

[112] Moore M, Wardlaw P, Dobson P, Boisvert JJ, Putz A, Spiteri RJ, et al. Understanding the Effect of Kinetic and Mass Transport Processes in Cathode Agglomerates. J Electrochem Soc 2014;161:E3125–37. https://doi.org/10.1149/2.010408jes.

[113] Tomadakis MM, Sotirchos S V. Ordinary and transition regime diffusion in random fiber structures. AIChE Journal 1993;39:397–412. https://doi.org/10.1002/aic.690390304.

[114] Carman PG. Fluid flow through granular beds. Chemical Engineering Research and Design 1997;75. https://doi.org/10.1016/s0263-8762(97)80003-2.

[115] Gostick JT, Ioannidis MA, Fowler MW, Pritzker MD. Wettability and capillary behavior of fibrous gas diffusion media for polymer electrolyte membrane fuel cells. J Power Sources 2009;194:433–44. https://doi.org/10.1016/j.jpowsour.2009.04.052.

[116] Closed-form Equation for Predicting the Hydraulic Conductivity of Unsaturated Soils, A (1) n.d.

[117] Kosugi K, Inoue M. Estimation of hydraulic properties of vertically heterogeneous forest soil from transient matric pressure data. Water Resour Res 2002;38:58-1-58–18. https://doi.org/10.1029/2002wr001546.

[118] Sheng J, Huang T, Ye Z, Hu B, Liu Y, Fan Q. Evaluation of van Genuchten-Mualem model on the relative permeability for unsaturated flow in aperture-based fractures. J Hydrol (Amst) 2019;576:315–24. https://doi.org/10.1016/j.jhydrol.2019.06.047.

[119] Li K. More general capillary pressure and relative permeability models from fractal geometry. J Contam Hydrol 2010;111:13–24. https://doi.org/10.1016/j.jconhyd.2009.10.005.

[120] Gostick JT, Fowler MW, Ioannidis MA, Pritzker MD, Volfkovich YM, Sakars A. Capillary pressure and hydrophilic porosity in gas diffusion layers for polymer electrolyte fuel cells. J Power Sources 2006;156:375–87. https://doi.org/10.1016/j.jpowsour.2005.05.086.

[121] Ament S, Daulton S, Eriksson D, Balandat M, Bakshy E. Unexpected Improvements to Expected Improvement for Bayesian Optimization 2025.

[122] Ringström M, Ekström H, Lindbergh G, Wreland Lindström R. Interplay between the GDL Mechanical Properties and the Flow Field Structure in PEMFCs. J Electrochem Soc 2026. https://doi.org/10.1149/1945-7111/aeb076.